UNIVERSITY OF CALIFORNIA

Santa Barbara

CELLS ON THE MOVE –

Intra- and Extra-cellular Mechanisms of in vivo Cell Migration

A dissertation submitted in partial satisfaction of the

requirements for the degree Doctor of Philosophy

in Molecular, Cellular and Developmental Biology

by

Xiaoran Guo

Committee in charge:

Professor Denise Montell, Chair

Professor Kathleen Foltz

Professor Dzwokai Zach Ma

Professor Diego Acosta-Alvear

December 2021

The dissertation of Xiaoran Guo is approved.

_____

Kathleen Foltz

_____

Dzwokai Zach Ma

_____

Diego Acosta-Alvear

_____

Denise Montell, Committee Chair

November 2021

CELLS ON THE MOVE –

Intra- and Extra-cellular Mechanisms of in vivo Cell Migration

by

Xiaoran Guo

ACKNOWLEDGEMENTS

I would like to thank my advisor Dr. Denise Montell for her guidance and tremendous support. Denise offers me so much to learn as a scientist. She generates many innovative ideas that greatly inspired me. She helps me identify the most important scientific questions with her experience and vision. She values my effort and helps prioritize my time among numerous leads that I could follow. At the same time, Denise gives me freedom and support to explore all the potential projects that interest me. For that reason, I was able to make discoveries in three different projects on cell migration and to be involved in an anastasis project; I also learned unique techniques. I am grateful for the time and effort that Denise has generously given to me to help me with my projects, presentations and writings, even during her rare and precious vacation times and weekends. Denise influences me in daily life: I learned to work hard and play hard. In family life, I try to treat my family as respectfully as "strangers" and do not take things for granted as Denise advised on my wedding. And she influenced me so that I always remind myself to be positive and brave to every challenge I encounter in life.

I want to express my gratitude to my lab colleagues and friends for being kind and helpful. Special thanks for Dr. Wei Dai who mentored me patiently when I joined the lab and has been continuously supportive throughout my studies. I want to thank my undergraduate research assistants throughout the years: Kristin Mercier, Marc Anthony Pastor, and Yijing Li. They have provided me massive technical support and accelerated my experimental progress.

I am grateful for my committee faculties: Dr. Kathy Foltz, Dr. Zach Ma and Dr. Diego Acosta-Alvear. Dr. Zach Ma raised intriguing questions about my projects. Dr. Diego Acosta-Alvear who gave great ideas for my Catsup project. Kathy, who also supervised me as a teaching assistant, has guided me a lot throughout my Ph.D. research career.

I appreciate the platform provided at UCSB and our MCDB department, especially Anthony Galaviz who gave essential support from my enrollment to graduation.

Last but not the least, I want to thank my parents Guoxin Ren and Jing Guo. They support my science dreams and always encourage me to explore the world. Many credits go to my husband Dr. Rui Wu for his understanding, support and company during my experimenting midnights and weekends. At last, I thank my 3-month baby Ian Yuran Wu for being very, very cute.

Curriculum Vitae: XIAORAN GUO

EDUCATIONS

Ph.D.	**Molecular, Cellular and Developmental Biology** University of California, Santa Barbara	2015 –2021 (Expected)
Visiting Student	University of California, Berkeley	2014-2015
Visiting Student	Texas Tech University	2013 - 2014
B.S.	**Biological Sciences** Cuiying Honors College in Lanzhou University	2011 - 2015

PROFESSIONAL EMPLOYMENT

Lab assistant	Rebecca Heald Lab University of California, Berkeley	2015
Teaching Assistant	Molecular, Cellular and Developmental Biology Department University of California, Santa Barbara	2016-2019
Graduate student researcher	Denise Montell Lab University of California, Santa Barbara	2013-2014

PUBLICATIONS

1. Dai, W.[1], **Guo, X.[1]**, Cao, Y., Mondo, J. A., Campanale, J. P., Montell, B. J., Burrous, H., Sebastian. S., Gov, N., Rappel, W.J., and Montell, D. J. Tissue topography steers migrating Drosophila border cells. (*Science*, 2020) *[1]equal contribution co-authors* https://science.sciencemag.org/content/370/6519/987.full
2. **Guo, X.**, Espinosa, A. T., Dai, W., and Montell, D. J. Collective border cell migration requires the Zn2+ transporter Catsup to promote endoplasmic reticulum-associated protein degradation. Preprint on *BioRxiv*, 2021
3. Sun, G., Ding, X. A., Argaw, Y., **Guo, X.**, and Montell, D. J. Akt1 and dCIZ1 drive cell survival of apoptotic caspase activation during regeneration and oncogenic overgrowth. (*Nature Communication*, 2020) https://www.nature.com/articles/s41467-020-19068-2
4. Popular science book (published in Chinese language) *In the next thirty years, where do humans heading towards?* Chapter 13-Gene Editing Technology (**Guo, X.**, 2020)
5. Fan, J., Du, Y., Turner, N.C., Wang, B., Fang, Y., Xi, Y., Guo, X., Li, F. Changes in root morphology and physiology to limited phosphorus and moisture in a locally-selected cultivar and an introduced cultivar of Medicago sativa L. growing in alkaline soil. (Plant and Soil, 2015) https://link.springer.com/article/10.1007/s11104-015-2454-0

AWARDS

The 2020 Chinese Government Award for Outstanding Self-financed Students	2020
2021 Schmidt Science Fellow nominee *UCSB selected the top 3 researchers on campus to compete in the global competition*	2020
Graduate Division Dissertation Fellowship, UCSB	2020

ABSTRACT

CELLS ON THE MOVE –

Intra- and Extra-cellular Mechanisms of in vivo Cell Migration

by

Xiaoran Guo

Collective cell migration is critical for development, wound healing, and tumor metastasis. Moving cells can sense and respond to physical features of the microenvironment; however, in vivo, the significance of tissue topography is mostly unknown. My research focused on *Drosophila* border cells in the Drosophila ovary, an established model for in vivo cell migration, to study how chemical and physical information influences path selection. Although chemical cues were thought to be sufficient, live imaging, genetics, modeling, and simulations show that microtopography is also important. Chemoattractants promote predominantly posterior movement, whereas tissue architecture presents orthogonal information, a path of least resistance concentrated near the center of the egg chamber. E-cadherin supplies a permissive haptotactic cue. The results provide insight into how cells integrate and prioritize topographical, adhesive, and chemoattractant cues to choose one path among many.

An advantage of the border cell model is that it is amenable to large-scale genetic screens. In a screen for mutations that cause border cell migration defects in mosaic clones, the gene

Catsup was identified. The *Drosophila* ortholog of *ZIP7* (*SLC39A7*), Catsup encodes a multifunctional endoplasmic reticulum (ER) transmembrane protein reported to negatively regulate catecholamine biosynthesis, to be required for Notch and EGFR trafficking, to function as a Zn^{2+} transporter, and to reduce ER stress. However, the relationship between these functions was unclear. Here we report that *Catsup* knockdown caused abnormal accumulation of Notch and EGFR proteins and induced ER stress in border cells. Ectopic expression of a folding-defective rhodopsin mutant protein, $Rh1^{G69D}$, also induced ER stress, inhibited Notch transcriptional responses, and blocked border cell migration, even in the absence of abnormal Notch or EGFR accumulation in the ER. Remarkably, simultaneous overexpression of Catsup and $Rh1^{G69D}$ was sufficient to degrade $Rh1^{G69D}$, resolve ER stress, and rescue border cell migration. Mutant forms of Catsup predicted to disrupt the Zn^{2+} transport were nonfunctional, indicating a requirement for Zn^{2+} transport in resolving ER stress. We propose a model for Catsup/ZIP7 function: local ZIP7-mediated Zn^{2+} transport at the ER/cytosol interface is rate-limiting for Zn^{2+}-binding ubiquitin ligases that promote ER-associated degradation (ERAD). Accumulation of misfolded proteins in the absence of functional ERAD triggers ER stress, which inhibits Notch transcriptional activity independently of trafficking or proteolytic activation. This proposed mechanism may be evolutionarily ancient, accounting for observations in multiple cell types, tissues, and organisms and suggests a novel treatment strategy for retinitis pigmentosa.

Cell movement depends heavily on cytoskeletal dynamics. Intermediate filaments are one of the major cytoskeletal networks involved in cell migration. Until recently, intermediate filaments were unknown in Drosophila. In the last chapter, I identified a new isoform of Tropomyosin1: Tm1-X, which has a domain architecture similar to intermediate filament

proteins and forms filaments in vitro. In vivo, Tm1-X promotes border cell migration. Together this work provides new insights into the intracellular and extracellular mechanisms regulating cell migration in vivo.

Table of Contents

1. Introduction 1

1.1. Cell-rich microenvironments influence cell migration in vivo 3

1.2. Cell-on-cell migration is prevalent in vivo 4

1.2.1. Cell-on-cell migrations in the nervous system 5

1.2.2. Cell-on-cell migrations in the immune system 5

1.2.3. Cell-on-cell migrations in cancer 9

1.2.4. Developmental cell-on-cell migration 11

2. Tissue topography steers migrating Drosophila border cells 17

2.1 Introduction 17

2.2. The function of chemoattractant in directing border cells migration 20

2.3. The role of E-cadherin adhesive molecule in guiding border cell migration 21

2.4. The 3D reconstruction of the egg chamber reveals the tissue topography microenvironment. 24

2.5. Simulation predicts that cells favor to migrate in multiple cell junctures 27

2.6. Migrating cells follow multiple cell junctures in various scenarios 30

2.7. The non-critical features in the chosen migration path 33

2.8. Migrating cells integrate and prioritize the environmental cues 35

2.9. Discussion 36

2.10. Supplementary Text 38

2.10.1. The free space in 2D and 3D 38

2.10.2. Energy costs of protrusions 40

2.10.3. The 3D dynamic model 41

2.11. Supplementary Figures and Legends 45

2.12. Supplementary Tables 64

2.13. Multimedia Files 81

3. Collective border cell migration requires the Zn^{2+} transporter Catsup to promote endoplasmic reticulum-associated protein degradation 83

3.1 Introduction 83

3.2. Catsup localizes with ER in the drosophila ovaries 85

3.3. Catsup is important for border cell migration 87

3.4. Catsup loss of function changes Notch and EGFR protein abundance 90

3.5. Catsup mutant causes ER stress 93

3.6. Zn^{2+} transportation and ER homeostasis 96

3.7. A model for Catsup/ZIP7 function: local Zn^{2+} transport is limiting for ERAD and mitigation of ER stress 99

3.8. Materials and methods *103*

4. A new Tropomyosin1 isoform supports Drosophila border cell migration **107**

4.1. Tm1-I/C is dispensable for border cell migration *108*

4.2. Tm1-X is sufficient to rescue border cell migration *108*

4.3. Tm1-X is a cytoplasmic, non-canonical Tropomyosin *111*

4.4. Methods and materials *115*

5. Perspectives and future directions **116**

5.1. How does nuclear stiffness contribute to migration through a confined, cell-rich environment? *117*

5.2. From border cell migration to a gene therapy for Retinitis Pigmentosa? *119*

5.3. Intermediate filament proteins in Drosophila? *122*

1. Introduction

This chapter is adapted from an unpublished review manuscript: Wei Dai, Xiaoran Guo and Denise J. Montell. “Cell migration through cell-rich microenvironments in development and disease.”

For embryos to develop, the nervous system to form, and the immune system to function, cells must move. Pioneering in vitro studies of fibroblasts, keratinocytes, Dictyostelium amoebae, and leukocytes revealed fundamental mechanisms of random motility and directional chemotaxis [1,2]. These include identification of chemoattractants and their receptors as well as the intracellular signaling pathways that transduce signals to reorganize and polarize the cytoskeleton. Early on, the vast majority of studies focused on single cells migrating on glass, but improvements in microscopy coupled with the ability to express fluorescent proteins in transgenic animals opened the door to studying cell movements in vivo, where cells often move in groups through diverse and complex microenvironments.

Extracellular physical and chemical cues steer migratory cells. A migrating cell, such as an immune cell [3] or a primordial germ cell [4,5], encounters disparate terrains, moving over or wedging between other cells (Introduction Fig. A), crossing epithelial, endothelial, and/or smooth muscle barriers (Introduction Fig. B), crawling on basement membranes (Introduction Fig. C) and/or squeezing through three dimensional (3D) fibrous networks (Introduction Fig. D). During development of the central nervous system, neural progenitors crawl directly upon radial glia to reach the appropriate layer [6]. The external chemical signals that can bias the direction of migration include chemokines, phospholipids, and secreted growth factors, which activate transmembrane receptors on the migratory cells.

Physical properties can also bias directional movement including gradients of charge, stiffness, and available space. Cancer cells hijack some of the same migration strategies to leave the primary tumor, enter the circulation, spread through the body, and establish metastases [7]. Though much research has focused on interactions between migrating cells and extracellular matrices [8], cell-on-cell migrations are prevalent in development, neurobiology, immunology, and cancer biology. There are multifarious roles that cell-cell interactions play in promoting, steering, and sometimes hindering cell migration in vivo.

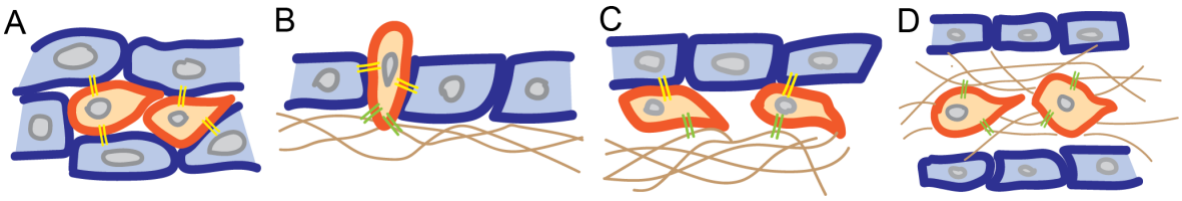

Introduction Figure. In vivo cell migration in varied microenvironments including cells and matrix.

Schematic illustration of the migratory cells in four types of tissue terrains. (A) Cells migrate among other cells. (B) Cells migrate across other cell layers. (C) Cells move between cellular structure and extracellular matrix. (D) Cells migrating in extracellular matrix. Migratory cells are illustrated in orange, stationary cells in blue, nuclei in grey, extracellular matrix in brown filaments, adhesion between cell and cell in yellow and adhesion between migrating cell and matrix in green.

The intracellular molecular interactions that drive cell migration behaviors are well-established. Regardless of the physical environment, migratory cells sense and respond to secreted chemoattractants that broadly activate either a receptor tyrosine kinase or a seven transmembrane-domain-containing, G-protein-coupled receptor to trigger cell polarization.

To move, cells need to polarize, protrude, generate new adhesions, and release the rear. There are distinct “modes” of motility: cells that move in a mesenchymal mode rely on protrusions driven by RacGTP-mediated F-actin polymerization, adhesion to the substrate, and acto-myosin-mediated contractility to pull up the rear. Alternatively cells such as primordial germ cells in zebrafish move via a bleb-based motion initiated by Rho-mediated contractility and hydrostatic pressure. The basic mechanisms of cell migration have been reviewed recently [9].

1.1. Cell-rich microenvironments influence cell migration in vivo

In vivo microenvironments are composed of cells and secreted extracellular matrix (ECM). The ECM is produced by cells, and its volume and architecture depends on the surrounding tissue and cell types. Migrating cells in vivo therefore can encounter different microenvironments that might be composed of mostly ECM, basement membrane on one side and cells on another, layers of cells followed by layers of ECM, or mostly cells.

Cells in the microenvironment can influence a migrating cell or cell group in a variety of ways. They can serve as sources and/or sinks for secreted factors that attract or repel [10]. Neighboring cells can produce, modify, and/or degrade ECM, which in turn can concentrate or sequester attractive and/or repulsive chemical cues that bind to ECM [8]. Additionally, cells frequently migrate directly on or between other cells, and the in vivo mechanical and topographical properties of the substrate cells directly triggers cell movement [11] or provides a path of least resistance [12]. Furthermore, cells in the microenvironment

communicate with migrating cells by exchanging materials and/or providing physical guidance through direct binding. Head to head collisions between migrating cells can lead to contact inhibition of locomotion (CIL), sending cells migrating in opposite directions, while head-to-tail contact can lead cells to join up and migrate in the same direction. Ultimately, migrating cells must integrate the varied incoming signals to choose one path amongst many. The stakes are high, as choosing the optimal path often promotes survival whereas errant cells are eliminated [13].

1.2. Cell-on-cell migration is prevalent in vivo

Many studies have focused on cells migrating on ECM; however, in vivo, cells commonly migrate on other cells. There are a few differences in the mechanisms by which cells migrate between other cells compared to movement on or through ECM. The main difference is in the receptors used for adhesion. The primary cell-matrix adhesion receptors are integrins whereas cell-cell adhesion also depends on classical and proto-cadherins as well as other families of cell-cell adhesion molecules. When cells migrate through dense ECM or between densely packed cells, they must make sufficient space in the surrounding microenvironment to accommodate the nucleus. Cells moving through ECM can use membrane bound or secreted proteases to locally dissolve the matrix and carve open a path whereas cells moving between other cells don't have this option and may thus be more constrained and sensitive to pre-existing spaces between cells. Given the prevalence of cell-on-cell migration, it is worth a deeper understanding.

1.2.1. Cell-on-cell migrations in the nervous system

Radial lamination of the neocortex

During brain development, newborn neurons migrate to organize into specific patterns required for neuronal circuit formation. The migration modes can be divided into radial and tangential, although a combination or switching has also been demonstrated [14]. Radial migration is a process important for cortical lamination in which neurons crawl upon radial glial cells, using them as monorail-like tracks. Molecules that have been implicated in the neuron-glia attachment, include integrin [15], gap junctions [16], and both classical and proto-cadherins. Recently, the neuronal receptor astrotactin (ASTN1) was shown to mediate the cadherin CDH2 interaction between neurons and glia [17], suggesting that cadherins also participate in heterophilic interactions. Cell-contact-dependent guidance via the adhesion molecule nectin has been shown to play a role in Cajal-Retzius cell directed neuronal migration [18].

1.2.2. Cell-on-cell migrations in the immune system

T cell maturation in the thymus

Mature T cells must be replenished throughout one's life. The differentiation and maturation of T cells relies on directional migration of T cell progenitors within the thymus. Once T cell progenitors enter the thymus, they migrate towards the cortex to differentiate from double

negative stage 1 (DN1) into DN2 and DN3. Through analysing the integrins expressed on DN2 cells and the microenvironment of thymus, DN2 cells were found to migrate on stromal cells through the adhesion between integrins and VCAM-1 molecules expressed on stromal cells [19]. The stromal cells become Notch-positive upon contacting T cell progenitors, which promotes T cell differentiation [20]. DN cells differentiate into Double Positive (DP: CD4+CD8+) cells as they migrate from the thymus cortex back to the medulla region. DP cells then go through positive selection, which is a process of differentiating into Single Positive (SP: CD4+ or CD8+) cells. SP cells migrate into the medulla to complete negative selection, which is the process that eliminates self-reactive T cells and thus prevents auto-immune disease. During negative selection, direct contact between Antigen Presenting Cells (APCs) and T cells exposes them to the entire repertoire of Tissue Restricted Antigens, and induces apoptosis in self-reactive T cells. To encounter as many APCs as possible within their 4-5 day stay in the medulla [21], thymocytes increase migration speed and make direct contact with various cell types including medullary thymic epithelial cells and dendritic cells [22]. When autoreactive T cells contact negative selection ligands, the migration slows down and they interact extensively with APCs [23]. The T cells that fail the selection die and are cleared quickly by phagocytes. Live imaging of Medaka shows that migratory thymocytes intermittently contact macrophages and dendritic cells, and that the macrophages can even extend long protrusions to clear dead thymocytes in regions without many phagocytes [24]. The whole maturation process is based on direct cell-cell contact-mediated T cell precursor migration.

Leukocyte transendothelial migration

The vascular wall is composed of endothelial cells, pericytes, smooth muscle cells, and basement membrane, and could vary depending on the location. Leukocyte extravasation is mediated by sequential interactions between leukocytes and the vascular cells. First, leukocytes roll on the endothelial cells through weak adhesion between leukocyte expressing an integrin CD11a and endothelial expressing ICAM, then they crawl by stronger adhesion mediated through integrin CD11b and ICAM to find the ideal spot for diapedesis [25], usually composed of multicellular junctions [26]. When migrating through the endothelial layers, leukocytes use the cell-cell adhesion molecule PECAM to bind to endothelial cells, and additional interactions of CD99 between leukocytes and endothelial cells are required for the transendothelial migration process. Meanwhile, VE-cadherin mediated adhesion between individual endothelial cells must be downregulated to allow leukocytes to pass between them [27]. The leukocytes then crawl between the endothelial layer and pericytes using CD11a to bind to ICAM [28]). Finally, the cells locate spots with thinner basement membrane and locally degrade it by secreting neutrophil elastase [29]. Thus the migrating cells and the cells in the environment cooperate to facilitate leukocyte movement.

Stem cell homing in the immune system

Stem cell homing is a process by which circulating hematopoietic stem cells migrate to the bone marrow niche. Homing also occurs when marrow mesenchymal stem cells migrate to the injured tissue for regeneration [30]. Similar to leukocyte transendothelial migration, the process of stem cell homing involves rolling and crawling on endothelial cells and then extravasation. The chemoattractant signals CXCR and SIP as well as integrin mediated cell-

cell interactions are also important in this process. Recent studies revealed that stem cell arrival in the perivascular niche triggers endothelial cell morphological remodeling such that endothelial cells and and stromal cells enwrap the stem cells [31]. This “cuddling” is important for providing a perivascular niche for stem cell self renewal. The molecules involved in endothelial remodeling and stromal cell anchoring are not known. Stem cells also interact with leukocytes via integrin signaling, which provides guidance [32], in a way similar to cancer cell and leukocyte interaction in the vascular system.

Immune surveillance and responses to wounding and infection

Cell-cell contact is an essential feature at many points in the response to a wound, infection, or tumor. For example, antigen presenting cells make direct cell-cell contacts with T cells to activate them [33]. Direct contact between neutrophils and cell debris within a sterile wound results in signaling that attracts more neutrophils and triggers swarming. On the other hand, macrophages can form a physical barrier to limit neutrophil contact with the wound, thus preventing swarming [34]. Neutrophil killing tumor cells can be promoted by IgA variant antibody treatment, in which neutrophils constantly express the Fc receptor (FcαRI) for IgA, therefore the killing is effective once the cell-cell contact is established between the swarming neutrophils and the IgA targeted tumor cells [35]. Neutrophil contacting necrotic tissue senses the damage signal ATP, triggers a sustained calcium flux, which induces chemoattractant synthesis. The calcium flux propagates through the nascent neutrophil cluster by the connexin-43 (Cx43) hemichannels [36]. Macrophages form tight clusters during an upregulation due to E-Cadherin-mediated adhesion between them. As important as activation of an inflammatory

response is the resolution of inflammation. E-cadherin may suppress contact inhibition of locomotion [37], regaining contact inhibition of locomotion by downregulating E-cadherin may contribute to dispersal of macrophages in the resolution phase [3].

1.2.3. Cell-on-cell migrations in cancer

Immune cell infiltration of tumors

The process of immune cell infiltration into solid tumors is important for the success of immunotherapy. The different subclasses of tumor immune microenvironment is key to understanding the difference in immunotherapeutic responsiveness [38]. Although how to enhance CAR T cell infiltration into solid tumors is still largely unknown, strategies targeting the tumor microenvironment and/or the T cell itself have been implicated. The lymphatic vasculature could serve as highways to help T cells to reach brain tumors [39]. Local tumor macrophages could serve as barriers for T cell infiltration [40]. Promoting T cell trafficking and persistence through STING agonist could modulate its ability to infiltrate breast cancer [41]. Tumor cell and T cell interaction through cell surface molecules also mediated tumor-induced exhaustion that affects T cell function [38]. Therefore, in addition to strategies enhancing T cell function intrinsically, modulating the extrinsic tumor microenvironment may also enhance T cell infiltration.

Transendothelial migration

Tumor cell extravasation requires direct interaction between tumor and endothelial cells, with assistance from leukocytes and platelets [42]. First, tumor cells adhere to the endothelium, which involves a variety of molecules including selectins, cadherins, and integrins [43]. Second, tumor cells modulate the barrier through regulation of endothelial cell-cell junctions [44,45] or induced necrosis [46]. Platelets release TGFbeta to induce an invasive, mesenchymal-like phenotype in tumor cells [47] and release dense granule-derived ATP to stimulate opening of endothelial barrier [42]. They also recruit granulocytes through chemokine secretion to entrap tumor cells at sites of metastasis [48]. Neutrophils are activated by tumor cells to release NETs which promote metastasis by sequestering circulating tumors, facilitating adhesion to the endothelium, and degradating the extracellular matrix.

Metastasis within and to the brain

Cell-on-cell migration mechanisms promote metastasis within and to the brain. During breast cancer metastasis to brain, cancer cells form pseudo-tripartite synapses with neurons to better absorb the glutamate secreted by the excitatory neurons, and activates the NMDA receptors on the metastatic cells to assist metastasis and colonization [49]. Breast and lung carcinoma cells require direct interactions with astrocytes through gap junctions to metastasize to the brain. The second messenger cGAMP travels through gap junctions from cancer cells to astrocytes, inducing inflammatory cytokine production, which enhances cancer cell growth [50]. Connexins, which are gap junction forming proteins, were also shown to be important in coupling breast cancer cells and melanoma with vasculature in the brain to promote metastasis [51].

Glioma has a tendency to disseminate broadly throughout the brain parenchyma, which makes this cancer particularly difficult to treat and leads to high rates of recurrence. Connexin 43 promotes direct interactions between glioma cells and astrocytes in 3D brain slice cultures [52]. Connexins form gap junction channels but also exhibit channel-independent functions, and the role of connexin43 in promoting glioma cell motility may be independent of its channel function. Overexpression of a channel-deficient mutant Connexin 43, which should be dominant-negative for channel formation, does not impair glioma invasion, whereas disrupting the cell-cell coupling mediated by connexin 43 reduces glioma metastasis [53]. Co-culturing glioblastoma with astrocytes and microglia has been reported to promote cell migration in vitro [54,55], consistent with the idea that cell-on-cell migration might be a common mechanism that glioma cells use to spread.

Neuronal and glial cell surface proteins can promote or suppress tumor invasion. For example, the adhesion molecule PTPmu suppresses the spreading and migration of glioblastoma within the brain [56]. On the other hand, platelet-derived growth factor (PDGF) releases contact inhibition of proliferation and migration by decreasing N-cadherin mediated cell-cell adhesion in a mouse model of aggressive glioma. Meanwhile, R-cadherin overexpression activates ERK signaling [57].

1.2.4. Developmental cell-on-cell migration

Developing embryos are a roiling sea of motion. Cell migration is required for everything from formation of germ layers to the development of every organ. While migration of cells on and through ECM has been extensively studied, some recent studies described below focus on cells migrating through cell-rich microenvironments. These examples represent the proverbial tip of the iceberg, and many additional examples are likely to be discovered in the future.

1.2.4.1. Cell intercalation in organogenesis

During animal development, cell-cell intercalation is a widespread and important mechanism through which short-range cell-on-cell migrations and rearrangements produce large scale changes in morphology [58]. Here we describe just two examples.

Xenopus skin

Xenopus epidermis is composed of an outer superficial layer and an inner epidermal layer. The superficial layer forms the outer barrier of the embryo with mucus-secreting cells, while the inner layer supplies ciliated cell precursors (CCPs) that migrate apically and intercalate into the outer layer, then differentiate into multiciliated cells (MCCs). Non-ciliated ionocytes also move from the inner layer into the outer layer through cell intercalation. The sites of cell intercalation are sparse and evenly distributed across the plane. Live imaging shows that MCCs intercalate at the site where multiple cells meet [59]. CCPs need to establish apicobasal polarity to properly intercalate into the outer layer [60] [61]. The molecular environment non-cell-autonomously determines successful intercalation, for instance, dystroglycan is essential in the

sensorial inner cells that are non-CCPs. Without dystroglycan, the inner layer cell adhesion is disrupted with impaired E-cadherin membrane localization, which may be essential for intercalation [62]. CCPs migrating into other outer layer cells is the first step, they have to expand apically to stably intercalate. The apical expansion is accomplished by formin-mediated actin polymerization [63]. The proper rate of actin network assembly is supported by RhoA, thus maintaining force balance in the apical surface during MCCs emergence [64]. The desmosomal protein desmoplakin also localizes to the apical surfaces of MCCs where it is required for apical expansion. By maintaining proper cytoskeleton organization and adherens junctions [65], desmoplakin facilitates establishment of new cell-cell contacts and thus stable MCC intercalation.

Mammary gland development

During mammary gland development, epithelial tubes emerge from an embryonic placode and branch into ductal arrays. At puberty, the ends of the ducts develop into stratified terminal end buds (TEBs). TEB cells adhere to each other via E-cadherin and continue proliferating and migrating on each other in the absence of extracellular matrix [66]. Through confocal imaging of mammary gland organoids, TEB cells can be seen to protrude between surrounding cells and crawl towards the tip of the branch, where they eventually intercalate into the outermost layer, thus elongating the tube [67]. Eventually, the multi-layered terminal bud cells all squeeze into the outermost epithelium, whereas cell proliferation does not play a significant role in the elongation process. Thus mammary gland development relies heavily on cell-contact mediated cell migration.

1.2.4.2. Lung cell slithering

Bronchial epithelium is a monolayer of polarized epithelial cells consisting of secretory cells and ciliated cells, among which pulmonary neuroendocrine (NE) sensory cells are initially randomly interspersed. During mouse lung epithelium development, NE cells delaminate from initial locations and slither across the apical surfaces of pulmonary epithelial cells toward NE clusters to form neuroendocrine bodies (NEBs). NEBs monitor oxygen, chemical and mechanical perturbations and transmit that sensory information to the central nervous system [68]. NEBs also function as stem cells to regenerate injured lung airways [69]. As they migrate, NE cells lose apicobasal polarity, transiently express the epithelial-to-mesenchymal transition (EMT) marker Snail, and downregulate E-cadherin mediated cell-cell adhesion. However, rather than migrating on basement membranes, pulmonary NE cells maintain membrane contact with the epithelial cells and crawl on them towards the NEBs cluster. Interestingly, NEBs clusters tend to form at the angled branching points rather than a straight flat region, which indicates that the tissue topographic information may influence the slithering directions [70].

1.2.4.3. Primordial germ cell migration

In most animal embryos studied to date, primordial germ cells (PGCs) undertake complex journeys through a variety of cell-rich tissues to reach the incipient gonad. In Drosophila [71], PGCs are first swept passively into the embryo with endodermal epithelium, adhering to it via E-cadherin mediated adhesion during gastrulation [72]. Next, PGCs undergo transepithelial migration to exit the gut epithelium in a process that requires gut epithelial

remodeling [73] (Fig.3B). Third, PGCs migrate dorsolaterally following a trail of phosphorylated lipids that binds the receptors Wunen and Wunen2 that are also lipid phosphate phosphatases. Wunen and Wunen2 are expressed by both PGCs and subsets of somatic cells in the embryo. Somatic cells thereby deplete some areas of the phospholipid. It is the remaining trail that the PGCs follow [74]. Because the phospholipid is essential for PGC survival, errant PGCs die (Fig.2A). Finally, surviving PGCs migrate towards the somatic gonad where cells express a still-mysterious attractant that requires a sterol modification [75].

In zebrafish, PGCs are specified in four different locations and actively migrate toward the developing gonad. PGCs and surrounding somatic cells express chemokine receptor Cxcr4 or Cxcr7 respectively to compete for the ligand Sdf1a [5] (Fig.2A). Zebrafish PGCs move via amoeboid bleb-based protrusions to squeeze through a cell-rich microenvironment via cadherin but not integrin [76]. By generating somatic clones depleted of E-cadherin, Grimaldi and colleagues demonstrated that E-cadherin mediates friction between PGCs and the surrounding somatic cells and potentiates the directional persistence in zebrafish PGCs [77]. Automated, high-throughput analysis of the tissue landscape revealed that the notochord acts as a physical barrier at the end of gastrulation [78], while later the somites expressing lipid phosphate phosphatases provide repulsive cues, and the developing gut acts as another physical barrier[79]. Therefore, although the exact route of PGC migration varies between organisms, they are highly influenced by nearby somatic cells, some of which secrete chemical attractants or provide a permissive adhesive substrate while others function as a chemoattractant sink or present a physical barrier.

1.2.4.4. Border cell migration

A well-studied example of cells squeezing between other cells during tissue development is the migration of border cells during Drosophila oogenesis. Ovaries are composed of strings of developing egg chambers, which contain 16 germ line cells enveloped by a somatic follicle cell epithelium. At developmental stage 9, a group of 6-10 follicle cells at the anterior egg chamber tip, round up, detach from the basal lamina, protrude dynamically and migrate by squeezing between the germ cells until they arrive at the anterior oocyte border. Border cells migrate ~150 um in 4-6 hours [80]. This is a clear example of cells migrating directly upon other cells as it depends upon E-cadherin expression on both border cells and nurse cells [81] and no ECM has been detected.

Numerous studies have reported the signals that stimulate border cell motility, the cytoskeletal regulators that govern their dynamically changing shape [82], and even the mechanism by which they connect to new partners at the end of migration [83]. In the following chapter, I report characterization of the non-autonomous effect of a specific physical feature of the microenvironment, the arrangement of nurse cells, on border cell path selection. In the final two chapters, I return to the functions of genes that act autonomously within the migratory cells. In Chapter 3, I report the essential role of mitigating ER stress during border cell migration and the remarkable finding that over-expression of a single zinc transporter is sufficient to rescue migration defects due to accumulation of misfolded proteins. This discovery has implications for treating protein misfolding diseases such as Retinitis

Pigmentosa. In the fourth and final chapter, I describe the discovery of a novel isoform of an unusual filament-forming protein and its role in border cell migration.

One strength of this relatively simple system is the ability to describe and to manipulate each of the key features of the microenvironment individually. In addition to loss of function and ectopic over-expression of chemoattractants and E-cadherin, as described below, we have been able to manipulate the arrangement of nurse cells to distinguish whether the border cells were attracted to some unidentified feature of the egg chamber center or to the multi-nurse-cell junctures that normally concentrate there. Using egg chambers with abnormal numbers and arrangements of nurse cells, we showed that off-center multi-nurse-cell junctures were more attractive than the geometric center.

2. Tissue topography steers migrating Drosophila border cells

This chapter is adapted from a published work: Wei Dai1, Xiaoran Guo1, Yuansheng Cao, James A. Mondo, Joseph P. Campanale, Brandon J. Montell, Haley Burrous, Sebastian Streichan, Nir Gov, Wouter-Jan Rappel, and Denise J. Montell. "Tissue topography steers migrating Drosophila border cells." *Science* (2020).

2.1 Introduction

Cell migrations are essential in development, homeostasis, and disease. While chemoattractants and repellents have been extensively studied [84–86], physical features of the microenvironment may be equally important. Here we use Drosophila border cells as a model and uncover a role for tissue topography in directional cell migration *in vivo*. Border cells are 6-10 follicle cells that delaminate and migrate collectively ~150 μm over 3-6 hours

within ovarian egg chambers, which are composed of 15 nurse cells and one oocyte, encased within ~850 epithelial follicle cells [7,80,87] (Fig.1A).

The oocyte secretes chemoattractants that activate two receptor tyrosine kinases (RTKs) [88–90]. The platelet-derived-growth-factor-and-vascular-endothelial-derived-growth-factor-like protein (PVF1) activates its receptor PVR [90]. The ligands Spitz (Spi), Keren (Krn), and Gurken (Grk) activate the Drosophila epidermal-growth-factor receptor (EGFR) [91]. Border cells lacking expression or activity of both RTKs, fail to reach the oocyte [89,90], and ectopic PVF1, Spi or Krn is sufficient to reroute them [91]. Similarly, lymphocyte homing, axon pathfinding, and migration of the zebrafish lateral line [92], neural crest [93], and primordial germ cells [13] have been attributed primarily to chemoattraction/repulsion. While the effects of substrate stiffness on migrating cells have been studied *in vitro* and *in vivo* [11,94,95], other physical features, like tissue topography, remain relatively unexplored.

By reconstructing egg chambers in three dimensions (3D), we noticed two orthogonal components to border cell pathway selection. Border cells migrate from anterior to posterior, the obvious path in a typical lateral view (Fig. 1A, fig. S1A). In addition, they follow a central path (Fig. 1B, fig. S1B and C, movie 1), despite encountering ~40 lateral alternatives (Fig. 1B and movie 2).

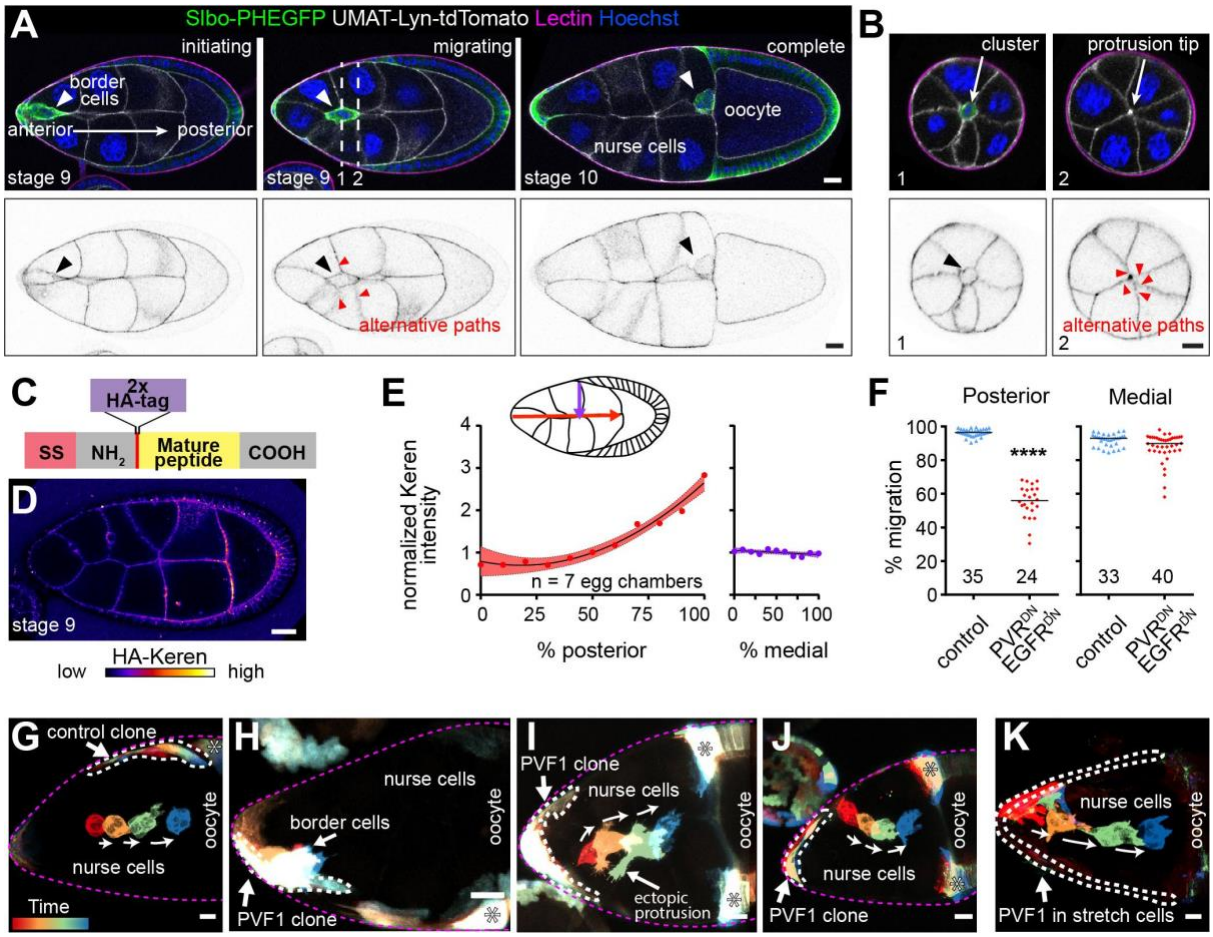

Fig. 1. Medial migration is not primarily controlled by chemoattractant guidance cues

(A) Lateral views of egg chambers showing border cell migration between nurse cells to the oocyte. Dashed lines represent cross sections shown in (B). (C) Schematic of endogenously CRISPR-tagged HA-Keren. (D) A living, unpermeabilized egg chamber stained for anti-HA-Keren (see also fig. S2). (E) Quantification of HA-Keren along anterio/posterior (left) and mediolateral (right) axes. Each dot represents a location along the path. (F) Quantification of border cell position. Each dot, one cluster. ****, $P < 0.0001$ (Mann-Whitney test). (G to K) Rainbow views of border cell migration in control or with ectopic UAS-PVF1 expression in clones (H-J) or in all anterior, "stretch" follicle cells (K). Scale bars, 20 μm.

2.2. The function of chemoattractant in directing border cells migration

To address whether the extracellular RTK ligands are present in gradients that might explain both posterior and medial guidance, we used CRISPR to epitope-tag endogenous PVF1, Spi, and Krn (see methods). [Grk directs dorsal movement only as the cells near the oocyte [80]]. Extracellular HA-tagged Krn (Fig. 1C) accumulated in an anterior (low) to posterior (high) gradient; however its concentration was not higher medially than laterally (Fig. 1D and E, fig. S2A and B). Intracellular, but not extracellular, HA-tagged PVF1 was detectable (fig. S2C and D). Tagged Spi was undetectable.

Since we could not detect all of the ligands, we addressed their contributions by expressing dominant-negative receptors (PVR^{DN} and $EGFR^{DN}$), which impedes posterior migration [89] (Fig. 1F, fig. S3A and B). Importantly, mediolateral defects were rare, occurring in <10% of egg chambers (Fig. 1F). RNAi caused similar effects (fig. S3C). Therefore, some other factor(s) must guide the cells medially.

Live imaging of egg chambers with ectopic PVF1 provided further evidence for independent attraction to the egg-chamber center (Fig. 1G to K). When anterior follicle cells ectopically expressed PVF1, border cells sensed the ligand because they were frequently detained at the anterior (Fig. 1H) compared to controls (Fig. 1G). Border cells also frequently protruded toward the ligand-expressing cells but remained on the central path (Fig. 1I). In other cases (Fig. 1J), border cells migrated along a patch of PVF1-expressing follicle cells, lingered, then nevertheless left the clone and returned to the egg-chamber center, ignoring more direct routes to the oocyte. PVF1 expression in all anterior follicle cells produced similar results

(Fig. 1K). Thus even in the presence of ectopic chemoattractant, border cells preferred the egg-chamber center, again suggesting that another signal steers them medially.

2.3. The role of E-cadherin adhesive molecule in guiding border cell migration

Of all the migration-defective mutants analyzed, only nurse-cell knockdown of E-cadherin exhibits dramatic mediolateral defects [96] (Fig. 2A and B), causing border cells to move between E-cadherin-positive follicle cells and nurse cells (fig. S4, movie 3).

How does nurse-cell E-cadherin contribute to central path selection? Neither uniform (17), nor asymmetric E-cadherin overexpression on nurse cells caused any medial guidance defect (Fig. 2A and B). Using near isotropic light sheet imaging (fig. S5), we detected no significant difference in E-cadherin concentration (Fig. 2C) on central versus side paths. Fluorescence recovery after photobleaching (fig. S6) also revealed no difference in E-cadherin dynamics between central and side paths (Fig. 2D and E) . E-cadherin knockdown did not alter the HA-Krn distribution in a way that could account for lateral path selection (fig. S7): a mediolateral gradient was absent, and an anterior/posterior gradient was still present (Fig. 2F and G).

Follicle cells normally express more E-cadherin than nurse cells (fig. S8A), so if differences in E-cadherin concentration steered border cells, we would expect that reduction of follicle cell E-cadherin might cause mediolateral guidance defects; yet follicle cell RNAi caused no defect (fig. S8B). Nor did E-cadherin over-expression in follicle cells impact pathfinding (fig. S8C to E). Therefore, though the presence of a low level of E-cadherin normally found

on nurse cells is essential for border cells to migrate between them, we found no evidence that E-cadherin concentration differences were sufficient to steer border cells.

We noticed that border cells pulled on wild-type nurse-cell membranes as they migrated, creating a measurable deflection of the nurse cells (Fig. 2H, movie 4, fig. S9). In contrast, border cells protruding between E-cadherin-negative nurse cells did not deflect their membranes (Fig. 2I to K, movie 4), suggesting border cells could not get traction. The lack of traction could in principle fully account for their inability to take the central path between nurse cells. Interestingly, border cells still protruded extensively between nurse cells; however the protrusions appeared as broad flat lamellipodia (movie 3) rather than the normal spear-shaped protrusions (movie 1). We conclude that E-cadherin supplies a permissive traction cue. As previously described (17), this mechanical function amplifies RTK signaling and shapes forward protrusions (17 and this study); however something other than differential adhesion must normally steer border cells to the central path.

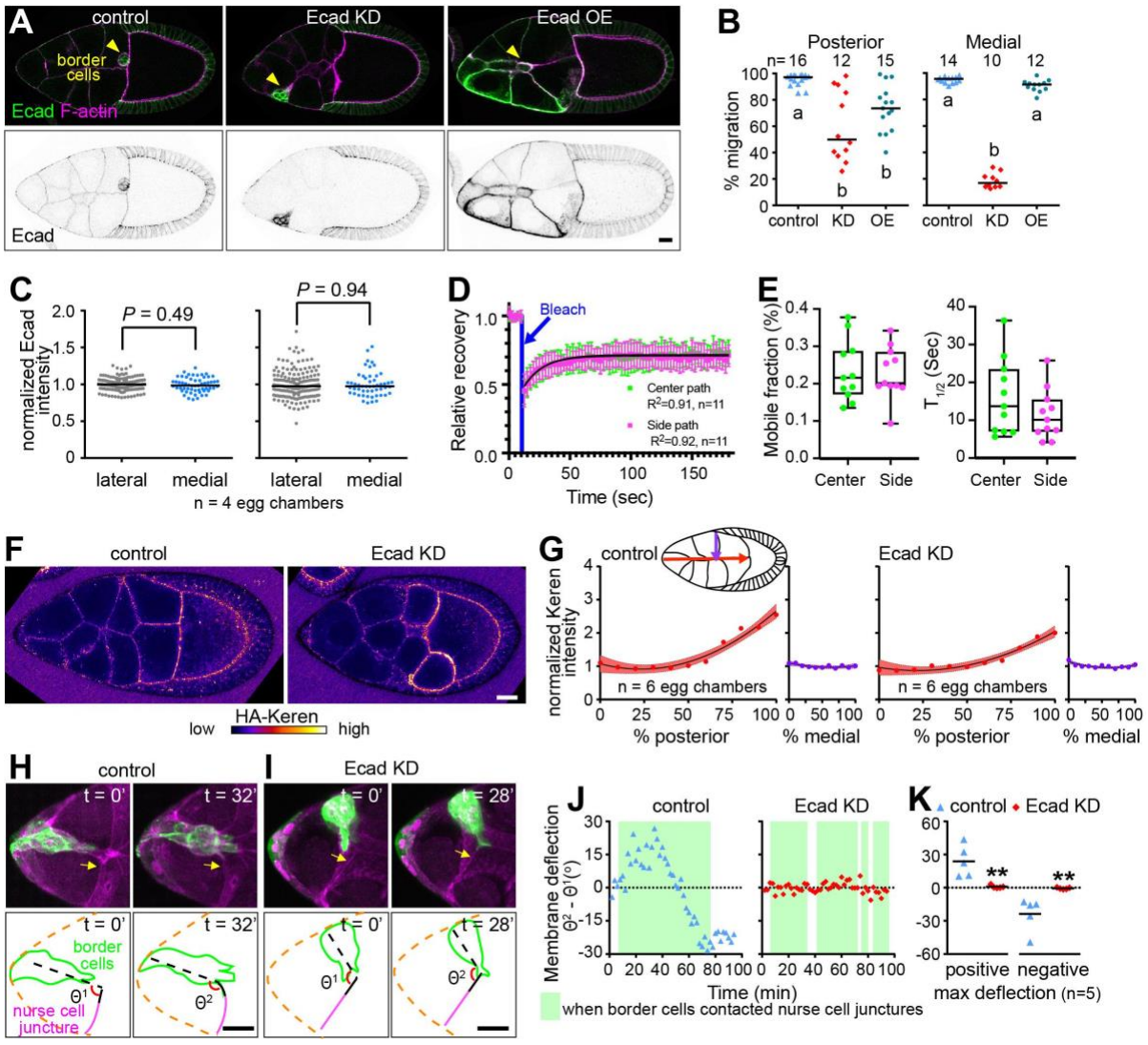

Fig. 2. E-cadherin provides a permissive medial traction cue

(A) Images of egg chambers from control, nurse-cell E-cadherin (Ecad) knockdown (KD), or mosaic nurse-cell overexpression (OE). Top panels show anti-E-cadherin (green) and phalloidin staining of F-actin (magenta). Bottom panels show anti-E-cadherin alone. (B) Quantification of migration. Letters a and b designate significantly different groups ($P <$ 0.01, Kruskal-Wallist test). (C) Quantification of E-cadherin and F-actin intensities on medial and lateral surfaces that lack ring canals. Anova with post-hoc Tukey test and blocking by

egg chamber. (D) Quantification of the FRAP experiment shown in (fig. S6). (E) Quantification of the mobile fraction and $T_{1/2}$ of E-cadherin on center and side membranes. (F) Anti-HA-stained, living egg chambers from control and E-cadherin knockdown (KD). (G) Quantification of Keren intensity along the anterior-posterior (coral) and lateral-medial (purple) axes. The line represents the best fit trendline of normalized Keren distribution along the A/P or L/M axis. Shading represents the standard deviation of the best fit trendline. There is no statistically significant difference between control and nurse-cell Ecad RNAi along the mediolateral axis (P = 0.6) or the relevant portion of the A/P axis (P = 0.6) that border cells encounter in the nurse-cell Ecad RNAi condition (see Fig. 2B). (H and I) Still images from movies showing (H) border cells pull on and deflect nurse-cell junctures in the control but not in the E-cadherin knockdown (I). (J) Traces of nurse-cell membrane deflections. (K) Quantification of maximum deflections. (**, $P < 0.01$ Mann-Whitney test). Scale bars, 20 μm.

2.4. The 3D reconstruction of the egg chamber reveals the tissue topography microenvironment.

Since neither chemoattractant nor adhesive cues fully accounted for medial pathfinding, we reconstructed egg chambers in 3D and characterized central versus side migration paths. The nurse-cell-oocyte complex is a syncytium packed within the follicular epithelium (fig. S10, movie 8) [97]. A striking feature of the central path is that it is where ≥3 nurse cells come together (lines and magenta dots in Fig. 3A, fig. S11). Side paths are largely composed of 2-nurse-cell interfaces (lines in Fig. 3B; planes in Fig. 3C, movie 5). Strikingly, ≥3-nurse-cell

junctures are enriched near the center (Fig. 3D). We use the word juncture, rather than junction to reflect the fact that they are places where cells come together but are not adherens, tight, or gap junctions.

We considered the influences that this geometry would likely have on border cells squeezing between nurse cells (supplementary texts ST1 and ST2). Due to the energy cost of unzipping nurse-cell-nurse-cell adhesions, protrusion into regions where multiple nurse cells meet should in principle be more favorable (Fig. 3E). This geometry argument predicts that there should be larger spaces where more nurse cells come together (fig. S12A to D), which we confirmed by measuring extracellular spaces using fluorescent dextran (Fig. 3F and G). As predicted, germline E-cadherin knockdown opened larger spaces (Fig. 3H, fig. S12E), confirming that E-cadherin normally seals nurse cells together. The free space should be most relevant at the scale of protrusions similar in size to the open space; the protrusions then steer the cluster. *In vitro*, migrating cells have been shown to choose channels that accommodate the size of the nucleus [98,99]; here we show that in vivo, even smaller spaces can guide cells.

To test the prediction that crevices where more cells come together present a lower energy barrier for protrusion, we examined 3D movies. Junctures of ≥3 nurse cells line the center path, and forward-directed protrusions always extended between multiple nurse cells. Moreover, when cells encountered two ≥3-nurse-cell paths, the cluster extended two protrusions (Fig. 3I). Eventually, the protrusion between the greater number of nurse cells always won.

When cells probed side paths, they extended into both 2-cell and 3-cell junctures (Fig. 3J). However, protrusion into three-nurse-cell junctures were more frequent (Fig. 3K), even though 2-nurse-cell interfaces offer vastly greater surface area (Fig. 3A and C). We conclude that crevices where multiple nurse cells come together create an energetically favorable path, and tissue topography, specifically ≥3-cell junctures, normally promotes central pathway selection.

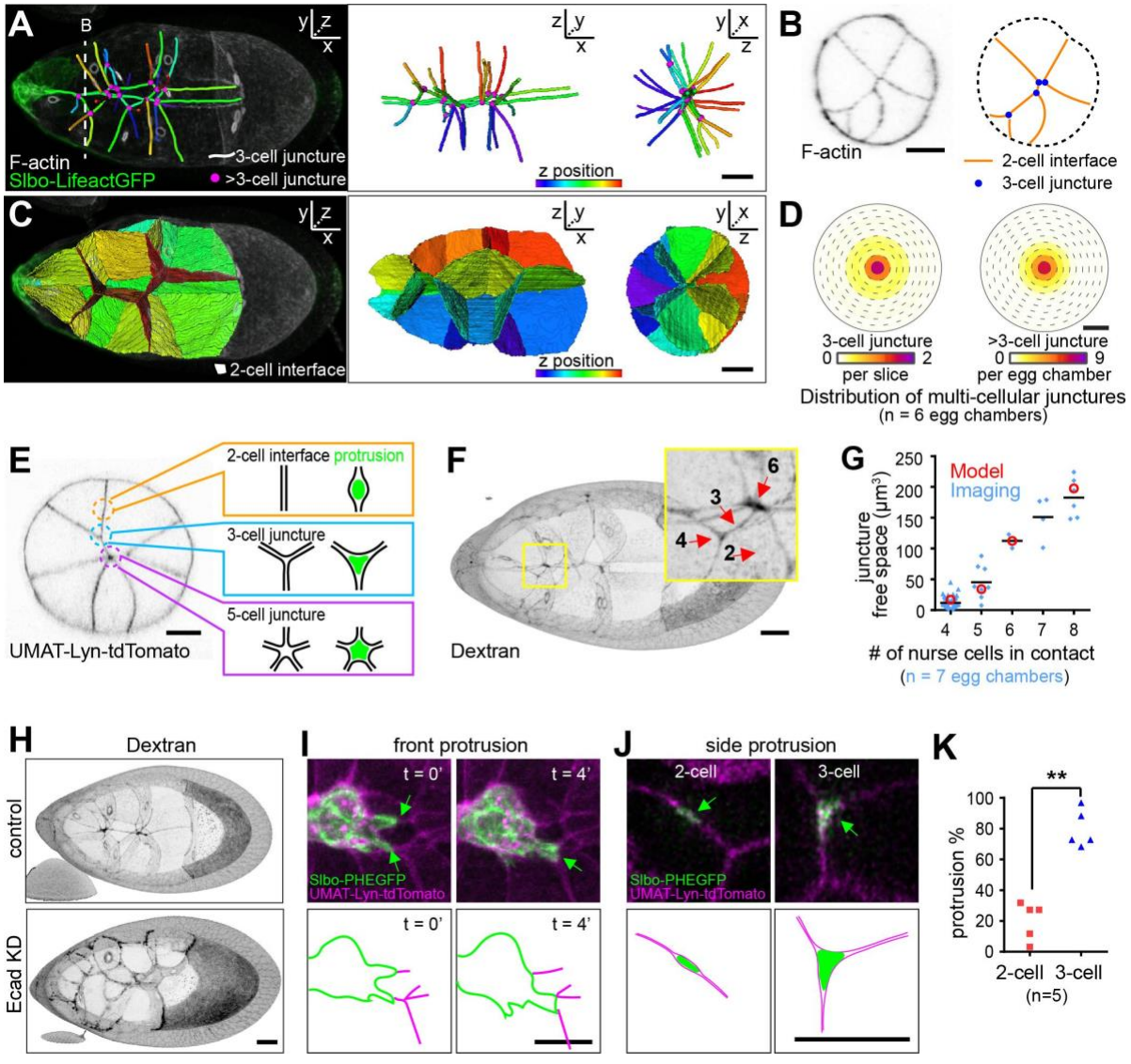

Fig. 3. The central path is enriched in junctures where multiple nurse cells meet

(A to C) 3D reconstructions of nurse-cell contacts. Dashed line in (A) indicates cross section in (B). (D) Heat map showing distributions of 3 (left) or >3 (right) cell junctures as a function of mediolateral position. (E) Schematic representation of border cell protrusion into nurse-cell junctures illustrating the concept that more space is expected in regions where more nurse cells meet. (F) Extracellular spaces filled with fluorescent dextran in a wild type egg chamber. (G) Quantification of extracellular volume as a function of the number of cells in a juncture. Values from the 3D model (red) (supplementary text ST1) and the experimental data (blue). (H) Dextran filled spaces (black) in a control stage 9 egg chamber compared to germline E-cadherin knockdown (KD). (I) Still images from two time points from a 3D movie. Two forward-directed protrusions (green arrows in I) encounter different multiple-nurse-cell junctures (magenta). The protrusion that reaches a >3 cell juncture wins (green arrow in B, n = 11 from 7 movies). (J) Cross-sections showing side protrusions (green) at 2-cell interface or 3-cell junctures (magenta). (K) Percentage of total side protrusions extending into 2-cell or 3-cell junctures. **, $P < 0.01$ (paired t test).

2.5. Simulation predicts that cells favor to migrate in multiple cell junctures

To test whether the combination of an anteroposterior chemoattractant gradient and a bias toward multiple cell junctures is in principle sufficient to explain border cell behavior, we developed a dynamic model that describes the trajectory of border cells moving within a realistic egg chamber geometry (Fig. 4A). We modeled the border cell cluster as a particle that moves stochastically in an effective potential $U(\vec{r})$(ST3) that incorporates two independent guidance terms: $\alpha D(\vec{r})$, the energy cost for the cluster to move between N nurse

cells, and $\beta \quad S \quad (\vec{r})$,the anteroposterior chemoattractant gradient. Simulating normal border cell migration conditions replicated normal trajectories (Fig. 4A to C, and movie 6). Eliminating the chemoattractant caused significant posterior migration defects but little deviation from the central path (Fig. 4A to D), consistent with experiments (Fig. 1F). In contrast, eliminating the preference for ≥3-nurse-cell junctures randomized mediolateral path selection without posterior migration defects (Fig. 4A, B, and E). Eliminating both terms produced dramatic mediolateral and anterioposterior defects (Fig. 4A, B, and F).

Multiple cell junctures are concentrated near the egg chamber center, so it could be that border cells are attracted to multiple cell junctures or to some other property of the geometric center of the egg chamber. For example, it could be that border cells are attracted to the center due to an unknown, centrally-concentrated chemoattractant or possibly due to an unknown laterally-concentrated chemorepellent, or some other unknown factor. To distinguish whether border cells prefer multiple cell junctures or the geometric center, we analyzed egg chambers with atypical geometries. In mutants that alter early germ cell divisions [100], we found some 31-nurse-cell egg chambers (fig. S13) with a central 2-nurse-cell interface (Fig. 4G). In each instance, the border cells selected the ≥3 nurse-cell-junctures even when off-center (Fig. 4G). Simulating migration using the 31-nurse-cell geometry and the same parameters as for wild-type reproduced the result (Fig. 4H and I). These results support the interpretation that border cells are attracted to multiple-cell junctures over any other property of the geometric center.

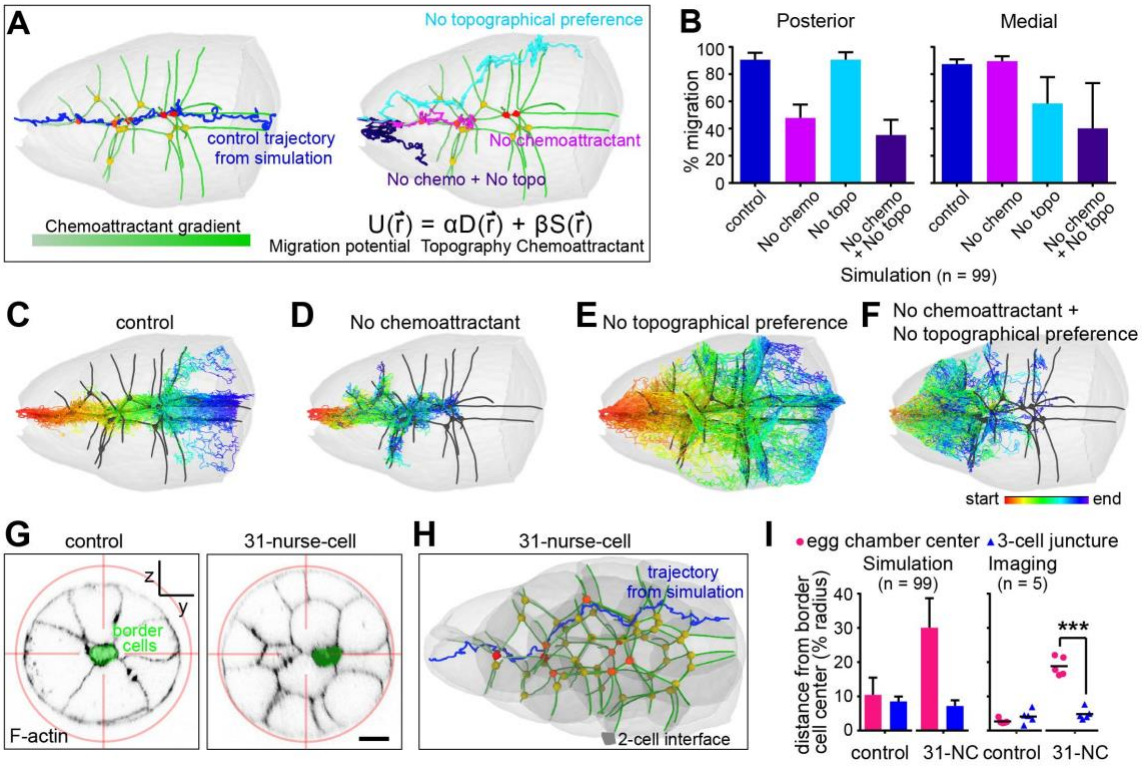

Fig. 4. Simulations and experiments showing preference for multiple cell junctures over the geometric center

(A) Representative simulated trajectories through the wild-type geometry shown in Fig. 3A. (B) Quantification based on 99 simulations. (C to F) Rainbow display of 99 simulated migration paths (red=start and blue=end) for each of the indicated conditions. (C) Normal condition in which path selection is a function of both a posterior chemoattractant gradient and increasing preference for junctures with increasing numbers of nurse cells. At the end of migration the influence of geometry weakens, correlating with loss of >3 nurse cell junctures. (D) Removal of the posterior chemoattractant gradient causes 100% posterior migration defect and 10% medial migration defect. Those clusters that deviate from the central path migrate into side paths with >3-cell junctures. (E) In the presence of chemoattractant but absence of preference for multiple nurse cell junctures, clusters migrate posteriorly but are distributed essentially randomly with respect to the mediolateral axis. (F) In the absence of

both chemoattractant and junctional preference, clusters exhibit both posterior and medial migration defects. (G) Cross-sections showing border cell and nurse-cell positions relative to the egg-chamber center in a control compared to a 31-nurse-cell egg chamber. (H) Representative simulated trajectory. (I) Comparison of the distance from the border cell centroid to the egg-chamber center vs the nearest 3-cell juncture. In both simulations and experiments, border cell position correlates more strongly with 3-cell junctures than the geometric center. ***, $P < 0.001$ (Paired t-test). Scale bars, 20 μm.

2.6. Migrating cells follow multiple cell junctures in various scenarios

We also simulated migration in egg chambers lacking nurse-cell E-cadherin, in which there is more free space where two nurse cells meet follicle cells than between one nurse cell and follicle cells (Fig. 5A). The model predicted and experiments confirmed that the border cells zig zag along grooves at nurse cell-nurse cell-follicle cell junctures (Fig. 5B, fig. S14, and movie 7).

We then re-examined the 10% of PVR^{DN}, $EGFR^{DN}$ egg chambers in which border cells are found off-center (Fig. 1F). Remarkably, border cells again moved to sites where multiple nurse cells meet (Fig. 5C and D), supporting the idea that multiple-cell junctures are energetically favorable even when not at the geometric center. Simulations also recapitulated this result (Fig. 5E).

At the initiation of migration when border cells first detach from the anterior follicle cells, the border cells are not always located at the geometric center (Fig. 5F to I), and 3-nurse-cell junctures are not as concentrated at the center at the anterior, compared to the rest of the migration path (Fig. 5G). Again, border cells preferred multiple-nurse-cell-junctures over the geometric center (Fig. 5H and I).

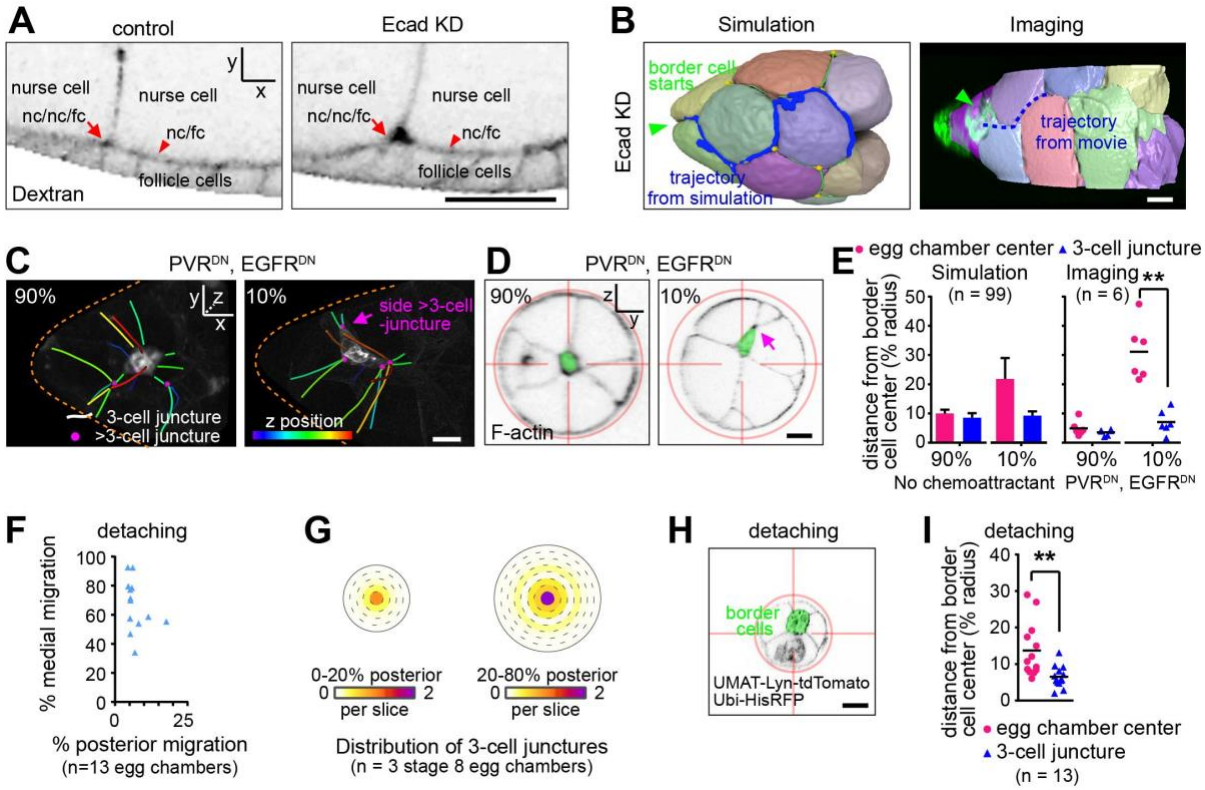

Fig. 5. Border cells follow off-center multiple-cell junctures

(A) Lateral view of dextran showing E-cadherin knockdown enlarged space. (B) 3D reconstructions of nurse cells with E-cadherin knockdown showing border cells in nurse cell-nurse cell-follicle cell grooves. (C and D) Border cell cluster location relative to nearby ≥3-cell junctures in representative egg chambers in which border cells express PVR^{DN} and $EGFR^{DN}$. In 90% of egg-chambers, border cell clusters remain in the center, while 10% migrate off-center (Fig. 1F, right panel). (E) Quantification of distance from border cell

centroid to the egg chamber center and the nearest 3-cell juncture. Simulation of no chemoattractant is done by removing the chemoattractant term. **, $P < 0.01$ (Paired t-test). (F) Migration in control stage 9 egg chambers when border cells are detaching from anterior follicle cells. (G) Heat map showing distributions of 3-cell junctures as a function of mediolateral position in stage 8 egg chambers at 0-20% posterior location or 20-80% posterior location. (H) Cross-sections showing border cells (green pseudocolor) and nurse cell junctions (black lines) relative to the egg chamber center. (I) Comparison of the distance from the border cell centroid to the egg chamber center (pink dots) vs the nearest 3-cell junction (blue triangles) in early stage 9 egg chambers when border cells are detaching from anterior follicle cells. **, $P < 0.01$ (Paired t-test). Scale bar, 20 μm.

2.7. The non-critical features in the chosen migration path

Many other features of the central path proved inconsequential (Fig. 6). For example, residual, stabilized cleavage furrows called ring canals connect germline cells to one another in a regular pattern (fig. S10). While the central path typically lacks ring canals (Fig. 6A, top), 63% lateral paths also lack ring canals (Fig. 6A, bottom), so absence of ring canals is insufficient to direct border cells centrally. Occasionally, we observed a ring canal along the migration path (Fig. 6B, fig. S15), and the border cells migrated around it (Fig. 6B). So absence of ring canals is neither necessary nor sufficient to provide medial guidance.

The central path is also normally devoid of cells. However, in 31 nurse cell egg chambers, border cells successfully navigate around centrally located cells (Fig. 6C and D). The central path is also normally composed of much smaller surface areas compared to side paths (Fig. 6A, fig. S16A and B). However, in egg chambers with 31 nurse cells (fig. S16A and B), the differences between medial and lateral surface areas are much reduced (fig. S16B), and in egg chambers with 7 nurse cells (fig. S16C and D) [101], the medial surfaces are nearly absent (Fig. 6E). Nevertheless, border cells still migrate in multicellular junctures and reach the oocyte border (Fig. 6F).

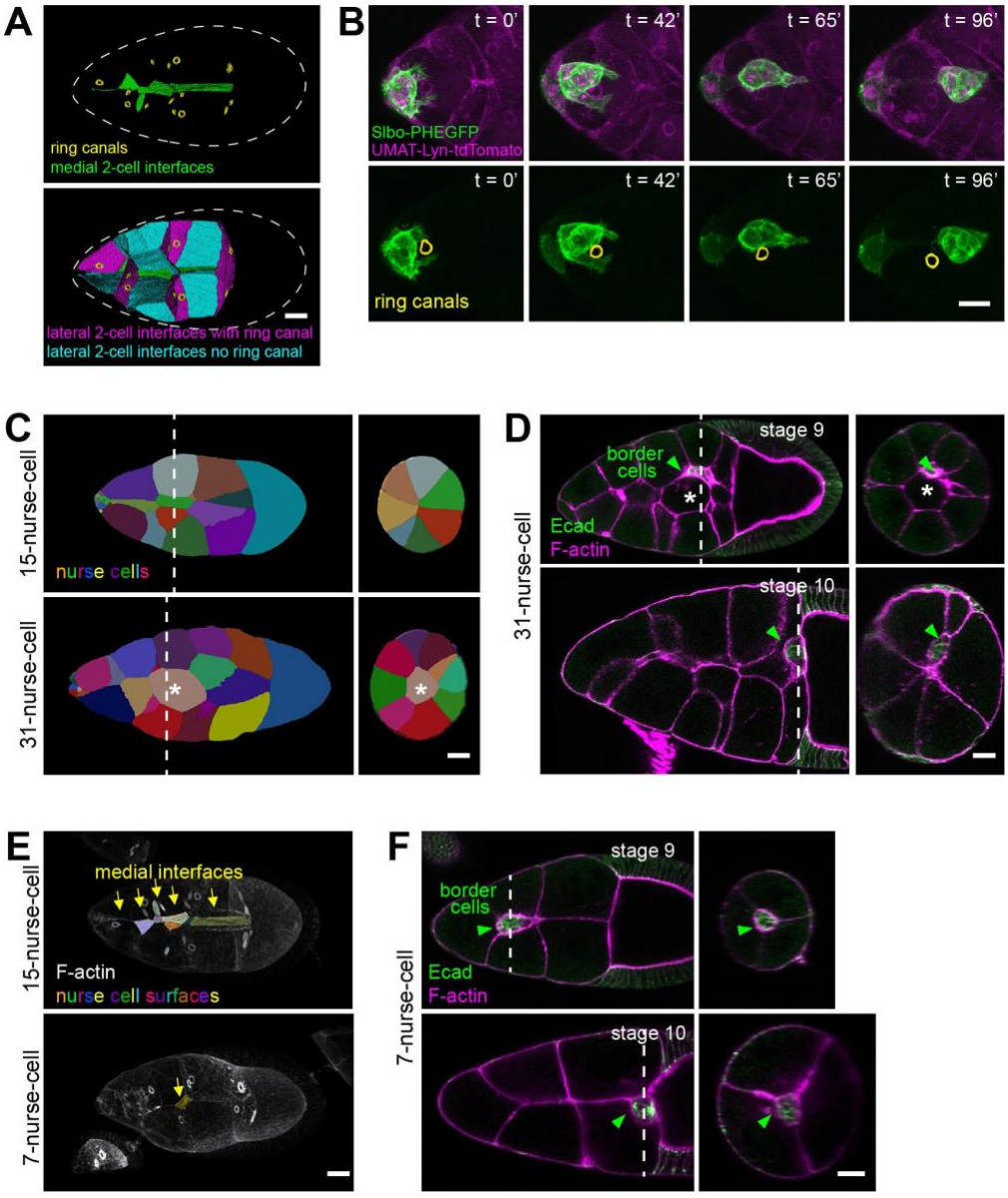

Fig. 6. Some physical features are not critical

(A) Ring canal locations on 2-germ cell interfaces. Medial interfaces (green) are free of ring canals (left panel). 15 lateral cell interfaces contain ring canals (magenta, right panel) and 26 do not (cyan). (B) Still images from a time lapse movie showing border cells migrating past a ring canal. Dashed line outlines the egg chamber. (C) Reconstructed nurse cell arrangements showing all nurse cells contact follicle cells in control, but there are 1-2 nurse cells in the center in 31-nurse-cell egg chambers. (D) Border cells migrate around a central nurse cell in

stage 9 (n=9) and reach the oocyte border by stage 10 in an egg chamber with 31 nurse cells (n=19). White lines indicate cross-sectional planes shown in the right panels. White asterisks indicate the central nurse cell. (E) Lateral view of segmented 3D nurse cell medial surface-surface contacts in early stage 9 egg chambers. (F) Border cells migrated along the multiple cell juncture and reached the oocyte border in stage 10 egg chambers with 7 nurse cells (n=41). White dashed lines indicate the cross sectional plane shown in the right panel. Scale bars, 20 μm.

2.8. Migrating cells integrate and prioritize the environmental cues

We gained further insight into how the cells integrate and prioritize the chemical and geometric cues. Results reported here show that, for most of their trajectory, the chemoattractants primarily guide the border cells posteriorly and multicellular junctures steer them centrally. These findings are consistent with an earlier study that used photo-activatable Rac (PA-Rac) to steer border cells [102]. PA-Rac could steer cells forward or backward down the center path throughout migration but was only able to steer them off center near the beginning or near the end [102]. Since Rac functions downstream of the RTKs, this already suggested that some other cue must steer the cells centrally and that this cue should be strongest between 25% and 75% of the distance to the oocyte.

Interestingly, ≥3 cell junctures near the end of migration, as border cells approach the oocyte, we found that >3-cell junctures are absent (Fig. 3A), which the model predicts would weaken the central bias of topographical information. Chemoattractant levels are highest near the

oocyte, and the EGFR ligand Gurken is enriched dorsally [91]. By aligning egg chambers according to the position of the oocyte nucleus, we noticed that the border cells typically squeeze between two nurse cells to move dorsally (Fig. 7A and B, movie 9). Adding Grk into the model and simulation accurately predicts this dorsal turn (Fig. 7C and D, movie 10).

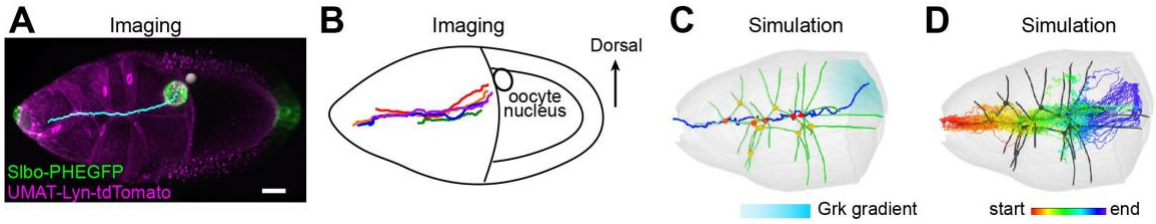

Fig. 7. Integrating and prioritizing topographic and chemoattractant cues

(A) Live imaging of a wild-type egg chamber, showing dorsal migration near the oocyte. The cyan line indicates the track taken by border cells (movie 9). White sphere indicates dorsal location of the oocyte nucleus. Scale bar, 20 μm. (B) Dorsoventral alignment of egg chambers according to the oocyte nucleus position, by rotation around the x-y plane, reveals consistent dorsal migration near the oocyte. Trajectories from each of 5 egg chambers are shown in different colors. (C) Representative simulation of a border cell migration path when the Grk gradient (cyan shading) is included (movie 10). Note that between the most posterior four nurse cells, >3-cell junctures (colored dots) are absent, weakening the geometry cue and allowing the chemical cue to guide cells through a suboptimal physical space. (D) 99 simulations with Grk gradient.

2.9. Discussion

Here we measure and manipulate chemical, adhesive, and topographical cues and elucidate their relative contributions to selection of one migration path amongst many. RTK signaling normally attracts border cells posteriorly toward the highest ligand concentration. We previously showed that E-cadherin amplifies small differences in chemoattractant concentration between the front and back of the cluster to ensure robust posterior migration [96]. Here we show that the key function of nurse-cell E-cadherin is to provide traction. However, differential adhesion does not provide directional information to steer the cells.

For medial path selection, the organization of the nurse cells is an instructive cue. At the junctures where multiple nurse cells meet, they do not quite touch due to geometry, leaving tiny openings where protrusions need not break as many adhesion bonds between nurse cells. Thus, the concentration of multiple-cell junctures near the egg-chamber center provides an energetically favorable medial path. When the chemoattractant concentration is high enough, for example when the cells near the oocyte or in the presence of ectopic PVF1, the chemical cue can dominate, allowing cells to move through suboptimal physical space. Similarly, when E-cadherin-mediated traction is unavailable on nurse cells, border cells migrate on follicle cells, choosing grooves where multiple cells meet. This work thus elucidates how border cells integrate and prioritize chemical, adhesive, and physical features of the in vivo microenvironment to choose a path.

The new work also offers an explanation for an earlier, unexplained phenomenon. The small GTPase Rac functions downstream of chemoattractant signaling [89,103] and Wang et al showed that a photoactivation of an optogenetic form of Rac within a single border cell caused

local protrusion and was sufficient to shift the direction of migration for the entire cluster [102]. Intriguingly, PA-Rac readily steered the cluster forward and backward along the medial migration path but it was not possible to steer the cells into side paths. At the time it was unclear what feature of the microenvironment was causing cells to favor the central path. The recent work shows that the central path is where multiple-nurse-cell junctures are concentrated, creating a path of least resistance.

2.10. Supplementary Text

2.10.1. The free space in 2D and 3D

To determine the possible free space in a N-cell juncture, we assume that the equilibrium configuration is determined by a balance between the adhesion energy between nurse cells (parameterized by A, per unit length in 2D, and per unit area in 3D) and the membrane/cortex bending energy (parameterized by bending modulus B, per unit length in 2D and per unit area in 3D). First, we consider the 2D case shown in fig. S12 A and B for $N = 3$and $N = 4$. The geometry of the junctures is characterized by circular arcs of membrane with radius R_f that join smoothly, i.e. without creating a cusp. The system's energy reaches a minimum when $\delta(W_{adh} + W_{bend})/\delta R = 0$. The bending energy for each arc is computed by integrating over the angle of polygon $(N-2)\pi/N$ (for the examples shown in fig. S12A and B this angle is $\pi/3$ and $\pi/2$, respectively). Computing the energy change for each arc, we arrive at $\delta W_{bend} = -BN\theta(N)\delta R/R^2$ with $\theta(N) = (N-2)\pi/N$. Due to the change in R the total length of cell-cell contact changes and the resulting total change in adhesion energy is $\delta W_{adh} = NA\delta L = N(A\ cot\ [\theta(N)/2]\delta R)$. Setting $\delta(W_{adh} + W_{bend}) = 0$ we find for the equilibrium radius

$$R_f{}^2 = B(N-2)\pi \tan(\pi/N)/(NA).$$

The area of the free space is then the area of the N-polygon connecting the circle center minus the area of the circular sectors. The area of the polygon is $NR_f{}^2 \cot(\pi/N)$while the area of sectors is $N\theta(N)R_f{}^2/2$. Thus, the total free space is given by

$$S_{free} = S_{polygon} - N\theta(N)R_f{}^2/2 = [N \cot(\pi/N) - (N-2)\pi/2]B(N-2)\pi$$
$$\tan(\pi/N)/(NA) \equiv f(N)B/A.$$

In fig. S12C we show that $f(N) = S_{free}/(B/A)$is a monotonically increasing function of N. This indicates that the available space becomes larger as the number of cells in the juncture increases. Note that $S_{free} \sim B/A$ which predicts that, as adhesion decreases, the free space in cell junctures increases, which is consistent with the results of the E-cadherin knock-down experiments (Fig. 3H, Fig. 5A, and fig. S12E).

Following the same argument, the above calculation can be directly extended to 3D, where the nurse cell membranes, now considered to be spherical caps, join smoothly at the juncture. Unlike 2D, where any number of arcs can join to form a polygon, in 3D the stacking of spherical caps is more complicated. Specifically, it is only possible for N=4,6,8,12, and 20, such that the center of the spheres form a polyhedron known as a Platonic solid. The N=4 example, resulting in a tetrahedron, is shown in fig. S12D. We again have the adhesion-bending $\delta(W_{adh} + W_{bend})/\delta R = 0$, where close at$\delta W_{adh} = ANR\delta R \cot[\theta(N)/2]$ and $\delta W_{bend} = -BN\phi(N)\delta R/R^3$. Here, $\theta(N)$ and $\phi(N)$is the dihedral angle and the solid angle of the face of the polyhedron, respectively. The equilibrium radius is thus

$$R_f^4 = B\phi(N)/(A\ cot\ [\theta(N)/2])$$

The free space volume is the volume of the Platonic solid minus the volume of the spherical caps,

$$V_{free}(N) = V_{solid}(N) - NR_f^3(N)\phi(N)/3.$$

For N=5, a simple configuration is mirror imaging a tetrahedron (N=4), which gives $V_{free}(5) = 2V_{free}(4)$. For N=7, there is no simple stacking. The ratio of the free space volume between N=4,5,6, and 8 in 3D is 1 : 2 : 6.6 : 11.6, which increases as N increases. This is close to the experimental ratio, which was found to be 1 : 3.8 : 9.5 : 15.5 (Fig. 3G, the middle point is arbitrary and is scaled to match the experimental data). As a comparison, the ratio in 2D is N=4,5,6,8 is 1 : 2.3 : 3.8 : 7.4.

2.10.2. Energy costs of protrusions

When border cell protrusions extend into a two-nurse-cell juncture, they have to "unzip" the adhesion bonds between nurse cells. Additionally, there is an energy cost due to the need to bend nurse cell membranes (Fig. 3E, orange box). The adhesion penalty is approximately $W_{adh,2} = 2\pi rA \approx AP$, where $r$is the average radius of the border cell protrusion and P is its perimeter. The bending penalty is $W_{bend,2} \approx 2\pi B/r$. When border cells protrude into $N \geq 3$ cell junctures, the protrusions break fewer adhesion bonds due to the pre-existing space, so the adhesion penalty is smaller than in two cell junctures. Furthermore, in contrast to the two-cell juncture, squeezing into $N \geq 3$should *release* bending energy, by reducing the nurse cell curvature from $1/R_f$ to $1/R_p$, where R_f and R_p represent the local radius of the nurse

cell membrane before and after the protrusion moves in (Fig. 3E, cyan and magenta boxes). In general, $R_p > R_f$. The adhesion penalty is proportional to the nurse cell membrane that must be unzipped, given by $W_{adh,N} = A(N-2)\pi(R_p - R_f)$. The difference of total bending energy is $W_{bend,N} = B(N-2)\pi(1/R_p - 1/R_f)$. In the simple case, we can model border cell protrusions in full contact with the nurse cells with a fixed perimeter of $(N-2)\pi R_p = P$. Note that, in this case, the adhesion difference due to nurse-border cell contacts is independent of N. Then, $W_{adh,2} > W_{adh,N}$ and $W_{bend,2} > 0 > W_{bend,N}$ for $N \geq 3$. Thus, both bending and adhesion energies favor protrusion into $N \geq 3$-nurse-cell junctures rather than into two-cell junctures. Furthermore, $W_{adh,N} = A(N-2)\pi(R_p - R_f) = AP - A(N-2)R_f$ decreases as N increases. Values of $W_{adh,N}$ are listed in Table S9.

Furthermore, we estimate the value of $B/A \approx 1\ \mu m^2$ by fitting the experimental data in Fig. 3G with the free space volume ratio in 3D. The relative contribution from adhesion and bending energy can be found from $|W_{bend,N}/W_{adh,N}| = \frac{B}{A|R_p R_f|} \approx \frac{\sqrt{B/A}}{R_p\sqrt{(N-2)\pi tan(\pi/N)}}$. R_p can be estimated from the size of the border cell protrusions $r = R_p\ tan\ (\frac{\pi}{N})$. From experimental data, we can estimate $r \approx 2\mu m$ (Fig. 3J). Plugging the estimates we get $|W_{bend,N}/W_{adh,N}| \ll 1$ for $N \geq 3$, which indicates that the bending energy is negligible compared to the adhesion energy.

2.10.3. The 3D dynamic model

To understand the dynamics of border cell cluster migration in response to physical and chemical cues, we developed a dynamic model that describes the trajectory of border cells

within an experimentally determined three-dimensional topography of egg chambers. A complete physical model would describe border cells as deformable 3D objects that exert forces on each other and on deformable nurse cells, and that migrate through a complex 3D geometry guided by chemotactic and geometric cues. Such a model is currently not feasible. We, therefore, model the border cell cluster as a point particle, representing the center of mass, that moves in a 3D geometry based on experimental data, and that follows experimentally derived rules. This model allows us to probe the relative importance of topographic and chemotactic cues.

The mass center of the border cell cluster is modeled as a particle located at position $\vec{r}$ moving in an effective potential $U(\vec{r})$ and subject to noise $\zeta(\vec{r},t)$. The motion can be described by an overdamped stochastic Langevin equation

$$d\vec{r}/dt = -\nabla U(\vec{r}) + \zeta(\vec{r},t),$$

where $< \zeta(\vec{r},t)\zeta(\vec{r}',t') >= 2 \;\; \delta(\vec{r}-\vec{r}')\delta(t-t')$. The effective potential incorporates the different guidance terms:

$$U(\vec{r}) = \alpha D(\vec{r}) + \beta_1 S_1(\vec{r}) + \beta_2 S_2(\vec{r}).$$

The topographic cue is described by the first term. It takes into account that the border cells have multiple protrusions which probe their surroundings. The border cell cluster is more likely to move into places where more free space is available. We model this by including the average energy cost in a sphere of cluster size

$$D(\vec{r}) = \int \quad W(\vec{r})\Theta(r_0 - r \;\;)d\vec{r} / \int \quad \Theta(r_0 - r \;\;)d\vec{r}.$$

Here $\Theta(r_0 - r \;\;) = 1$when $r_0 > r$, otherwise $\Theta(r_0 - r \;\;) = 0$, $r_0$is the average radius of the border cell cluster, and $W(\vec{r}) = W_{adh}[N(\vec{r})] + W_{bend}[N(\vec{r})]$, where W_{adh} and W_{bend} are the

energy costs of protruding into a N-cell juncture at position $\vec{r}$ (computed in ST2). Note that $D(\vec{r})$ has a dominant weight to the outer surface of the cluster where protrusions are formed.

The chemotactic cues are described by the second and third term and take into account chemoattractant gradients along the anterior-posterior and dorsal-ventral axis. Along the anterior-posterior axis, we use, following (*27*), an exponential concentration profile: $S_1(\vec{r}) = c_0 + (c_m - c_0)\ exp\ [-(x - L)/\xi]$, where ξ is the length scale of the exponential profile decay, and L is the total length of the egg chamber. Dorsal-ventral guidance is incorporated by a concentration gradient of the protein Gurken, which we represent as $S_2(\vec{r}) = c_2[d_0 - d(x, y, z)]$, where $d(x, y, z) = \sqrt{(x - x_0)^2 + (y - y_0)^2 + (z - z_0)^2}$ is the distance to the Gurken source. Earlier studies revealed that this guidance is only relevant near the posterior of the egg chamber and thus only exists in our model when $x > 2L/3$ (*5*). Furthermore, we assume that nurse cells represent static obstacles such that $U(\vec{r}) = \infty$ when $\vec{r}$ falls within a nurse cell. Finally, the strength of the geometric cue and chemotactic cue is determined by the parameters α, β_1 and β_2.

In our simulations, we first discretized space in an experimentally segmented egg chamber, resulting in a cubic grid of 1μm. Each grid point is assigned with an identity which indicates the juncture type it belongs to (e.g., 2 or 3-cell juncture). Our simulations started by placing the particle (i.e., border cell cluster) at the anterior end of the egg chamber. We then incorporated a discrete version of the Langevin equation in which, for each time step, the particle can move to a neighboring cubic grid points with probability

$$p(\vec{r} \to \vec{r} + \Delta r) = Z^{-1}\ exp\ \{[U(\vec{r}) - U(\vec{r} + \Delta r)]\},$$

where $Z = \sum_{\Delta r} \quad exp\{[U(\vec{r}) - U(\vec{r} + \Delta r)]\}$ is the partition function, and the sum is over all nearest neighbors of position $\vec{r}$. The potential can be parameterized by rescaling units such that $A = 1$ (notice that the bending energy is negligible, as shown in ST2). The simulation was terminated when the particle reached the oocyte or the total number of simulation steps exceeded 10^4(a typical simulation in wild type egg chamber takes $\sim 10^3$ steps.). Parameters used in the model are given in Table S10. For different combinations of α and β, the mediolateral and anteroposterior indices are shown in Table S11.

Our model can also be applied to the case when E-cadherin is knocked down. In the E-cadherin knockdown egg chamber, the nurse-follicle cell junctures are 2.5 fold larger than the wild type nurse-follicle cell juncture (Fig. 5A, fig. S12E). This difference in juncture size indicates that the adhesion between nurse cell and follicle cells is smaller (see section above). In our simulation, we set $A = 0.4$ while keeping the other parameters the same.

2.11. Supplementary Figures and Legends

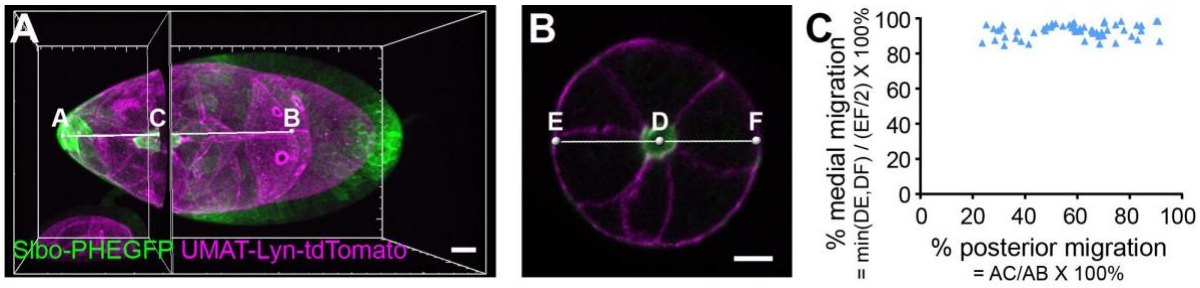

Fig. S1. 3D analysis reveals orthogonal anteroposterior and mediolateral pathway choices

(A) Lateral view showing the method for quantification of posterior migration. (B) Cross sectional view showing the method for quantification of medial migration. (C) Migration in control stage 9 egg chambers. (n = 59 egg chambers). Scale bars, 20 μm.

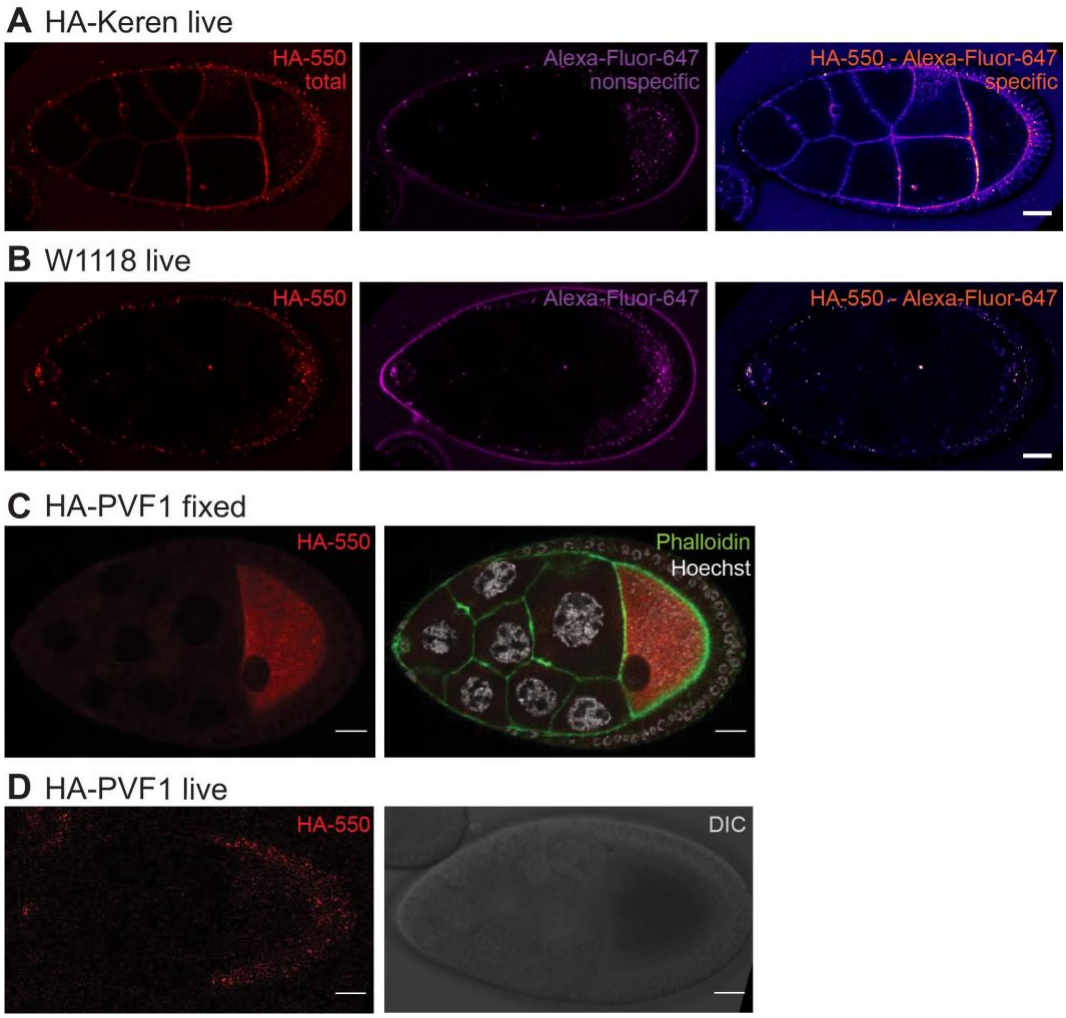

Fig. S2. HA tagging chemoattractant staining

(A) Staining of a living stage 9 egg chamber from a homozygous CRISPR HA-Keren fly with anti-HA-550 and a non-specific Alexa-647 antibody. The 550 - 647 signal provides the specific HA-Krn signal. (B) Staining of a stage 9 egg chamber from w1118 (negative control) with the same antibodies as in A. (C) Staining of a fixed and permeabilized stage 9 egg chamber from a homozygous CRISPR HA-PVF1 fly with anti-HA-550 antibody alone and with Hoechst for DNA (white) and Phalloidin for F-actin (green). (D) Staining of a living stage 9 egg chamber from a homozygous CRISPR HA-PVF1 fly with anti-HA-550 showing that extracellular PVF1 is not detected, though the tagged protein is functional because

homozygous flies are viable and fertile (Table. S8). DIC imaging of the same egg chamber is shown. Scale bars, 20 μm.

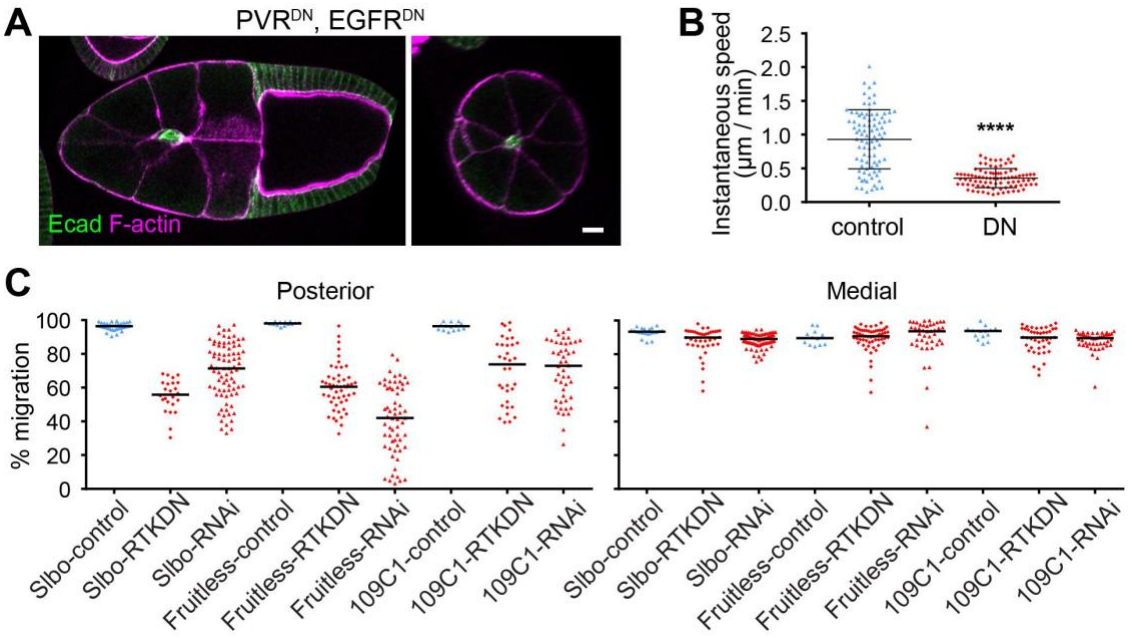

Fig. S3. Migration defects caused by PVR and EGFR RNAi or dominant-negatives (DN)

(A) Lateral and cross sectional view showing an example of posterior migration defect but normal mediolateral path selection in slbo-Gal4>UAS-PVR^{DN}, EGFR^{DN}. Scale bars, 20 μm. (B) Quantification of instantaneous migration speed during early stage 9, in 2 minute time intervals over the course of one hour in slbo-Gal4 control or slbo-Gal4>UAS-PVR^{DN}, EGFR^{DN} . Data from $n = 90$ time points (30 time points each from 3 egg chambers per group). ****, $P < 0.0001$ (Mann-Whitney test). Reduced migration speed shows the dominant-negative receptors were effective. (C) Quantification of migration index following expression of EGFRDN and PVRDN (RTKDN) with the following Gal4 lines: Fruitless-Gal4 expresses in border cells from stage 4, 109C1-Gal4 from stage 7, slbo-Gal4 from stage 8.

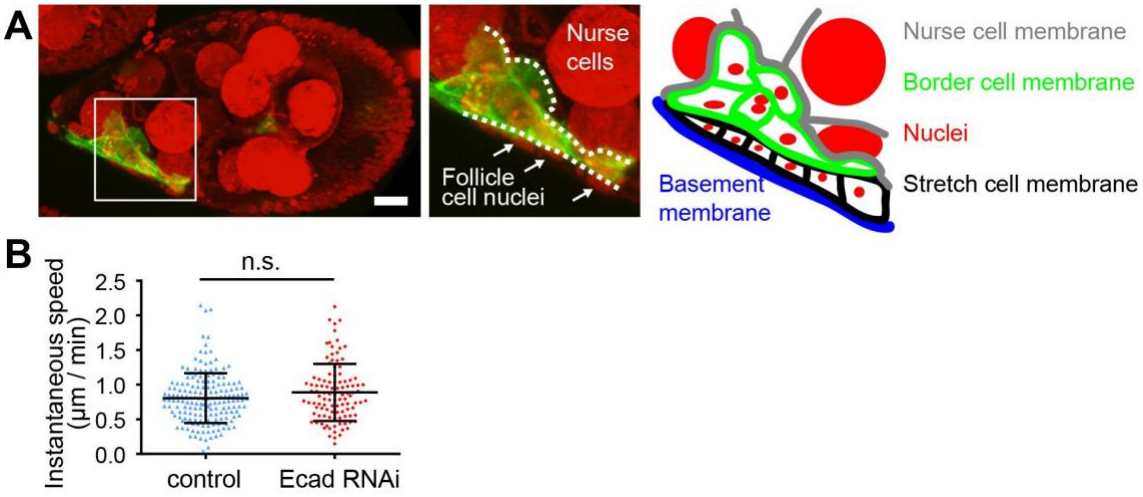

Fig. S4. Effect of nurse cell Ecad knockdown on border cell migration

(A) In nurse cell Ecad knockdown, border cells (marked by Slbo-PHEGFP) migrate in between follicle cells (white arrows) and nurse cells. Scale bars, 20 μm. (B) Quantification of instantaneous migration speed every 4 minutes in control Matalpha-Gal4>UAS-wRNAi or Matalpha4-Gal4>UAS-Ecad RNAi. In contrast to RTK inhibition, migration speed was not initially reduced. Data from eight WT controls n = 178 time points; eight nurse cell Ecad RNAi egg chambers n = 107 time points.

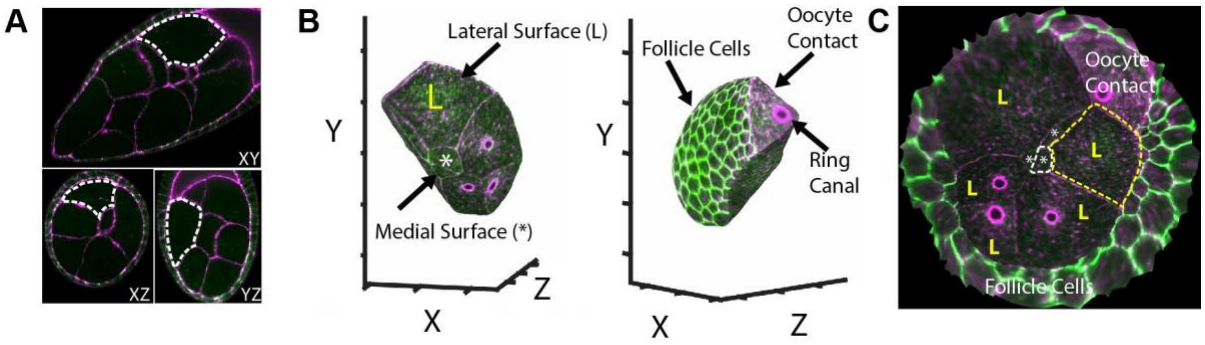

Fig. S5. Isotropic light sheet imaging shows no differences between Ecad concentrations on medial vs. lateral membranes

(A) Isotropic light sheet imaging of a stage 9 egg chamber stained for F-actin with phalloidin (magenta), and anti-Ecad antibody (green). Dashed lines indicate the boundaries of a single nurse cell in the XY/XZ/YZ orthogonal views. (B) 3D reconstruction of the surface of the nurse cell outlined in (A). (C) "Pullback" of the surface of the 3D reconstruction in (B) created with the Images Surfaces Analysis Toolkit (*26*). The pullback represents the summed intensity projection of 1.5um thickness around the surface of the 3D object in (B). Medial surfaces are represented by (*) and lateral surfaces by (L).

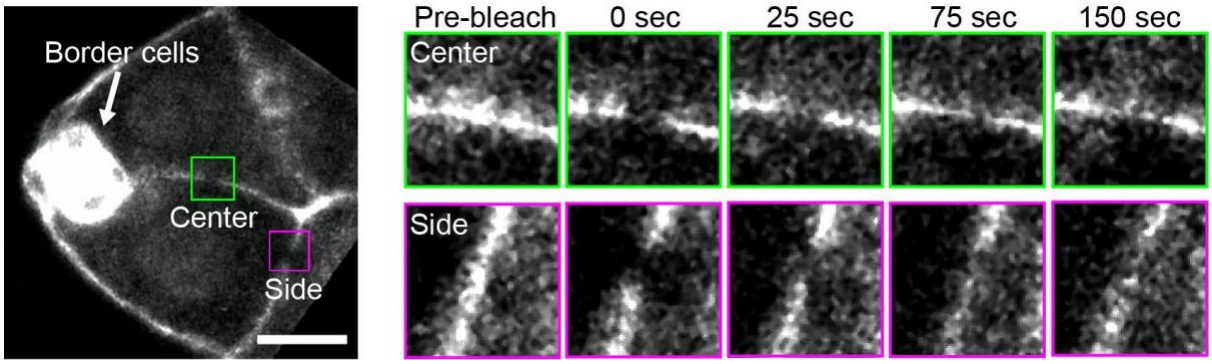

Fig. S6. Fluorescence recovery after photobleaching (FRAP) shows no difference in Ecad stability on center and side paths

Stage 9 egg chamber with Ecad endogenously tagged with GFP. Insets show center vs. side membrane Ecad signal. Scale bar, 20 μm.

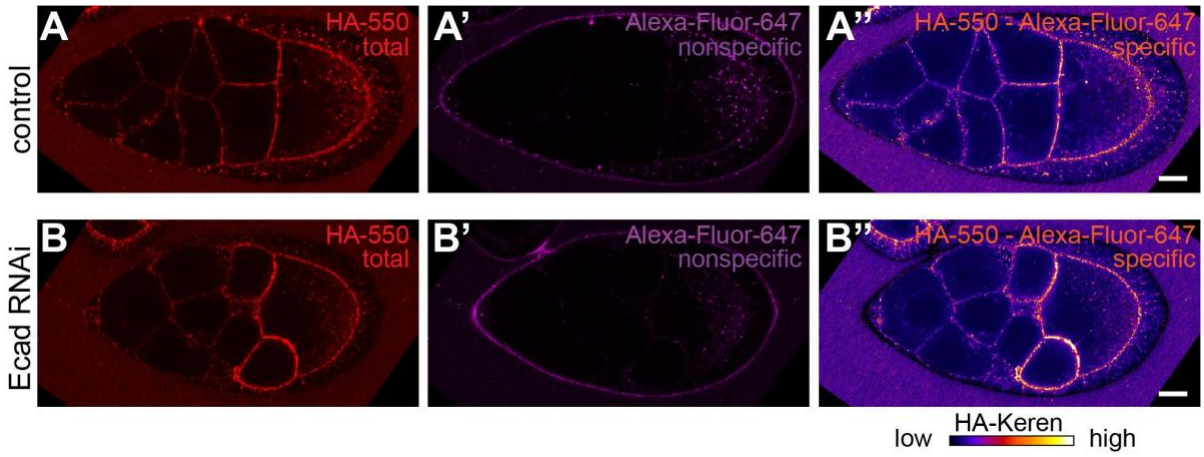

Fig. S7. HA-Krn concentration in control and nurse cell Ecad RNAi expressing egg chambers

Ecad RNAi does not cause a redistribution of HA-Krn that would account for the mediolateral border cell guidance defect. (A) Confocal imaging of anti-HA-550 staining of a living stage 9 egg chamber from a heterozygous CRISPR HA-Keren fly (negative control) [genotype: MatalphaGal4/+;HA-Keren/+;UAS-wRNAi/+]. (A') Labeling of the same egg chamber using a non-specific Alexa-647 antibody. (A'') The specific pattern of HA-Krn was calculated by subtracting the non-specific 647 signal from the total 550 fluorescence. (B-B'') Staining of a stage 9 egg chamber from MatalphaGal4/+;HA-Keren/+;UAS-EcadRNAi/+ using the same method as in A-A''. Scale bars, 20 μm.

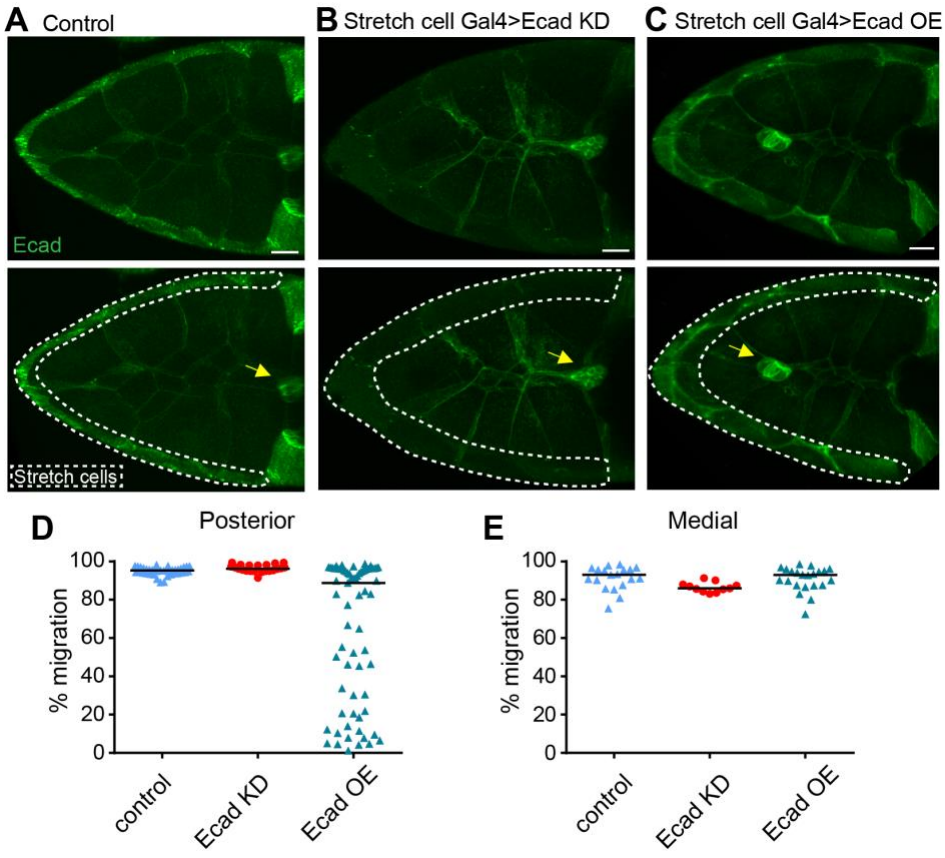

Fig. S8. Stretch cell Ecad knockdown shows no medial guidance defect

Projections of 18 confocal sections (2um each) of anti-E-cadherin staining of early stage 10 egg chambers in the indicated genotypes. (A) Control, stretch cell Gal4>wRNAi, (B) Decreased Ecad level in stretch cell Gal4>Ecad RNAi. (C) Increased Ecad in stretch cell Gal4>Ecad. Scale bar, 20 μm. Dotted lines show stretch cell regions; Arrows indicate border cell clusters. Quantification of posterior (D) and medial (E) migration in egg chambers for each genotype. Scale bars, 20 μm.

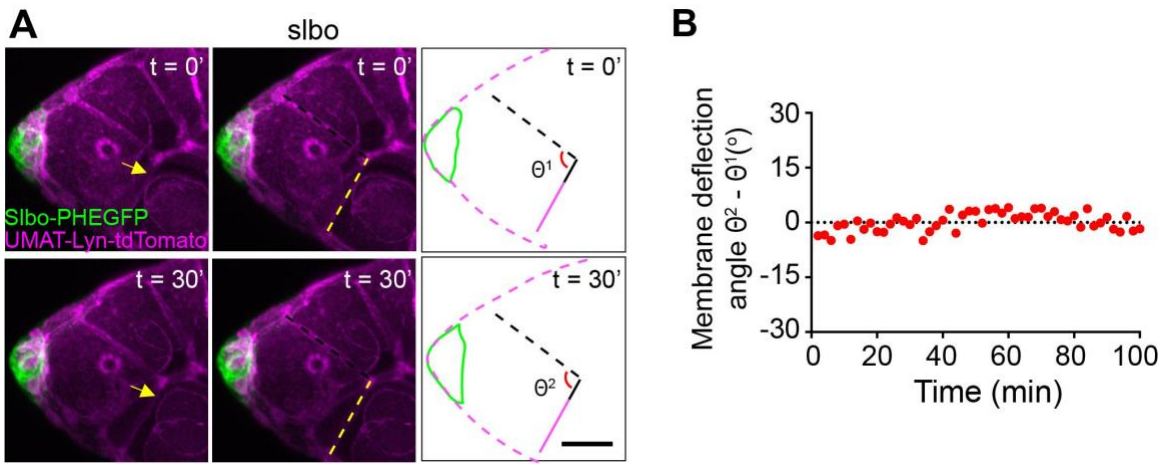

Fig. S9. Nurse cell membrane deflections require border cell migration

(A) Still images from a movie of a *slbo* mutant egg chamber in which border cells do not migrate (*28*). No nurse cell juncture deflection occurs, showing that they are not random fluctuations; rather they are caused by border cells actively pulling. Scale bar, 20 μm. (B) Representative trace of normalized nurse cell membrane deflections in the *slbo* mutant.

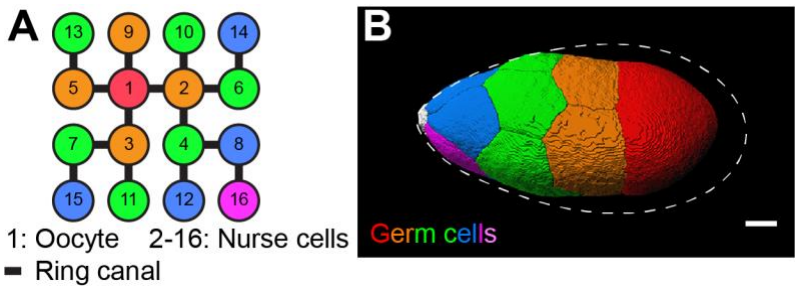

Fig. S10. Nurse cell arrangements in control egg chambers

The 16 germ cells derive from a single germline precursor, which undergoes four rounds of cell division with incomplete cytokinesis. Residual, stabilized cleavage furrows called ring canals thus connect germline cells to one another in a regular pattern. (A) Schematic drawing of the germ cell identity (numbers in circles) based on their birth order and thus ring canal connections (lines) in control egg chambers. Colors indicate distance to the oocyte (#1). (B) 3D reconstruction of germ cell packing in stage 9 egg chambers. White, border cells at the anterior tip. Dashed line indicates the somatic follicle cell layer. Scale bar, 20 μm.

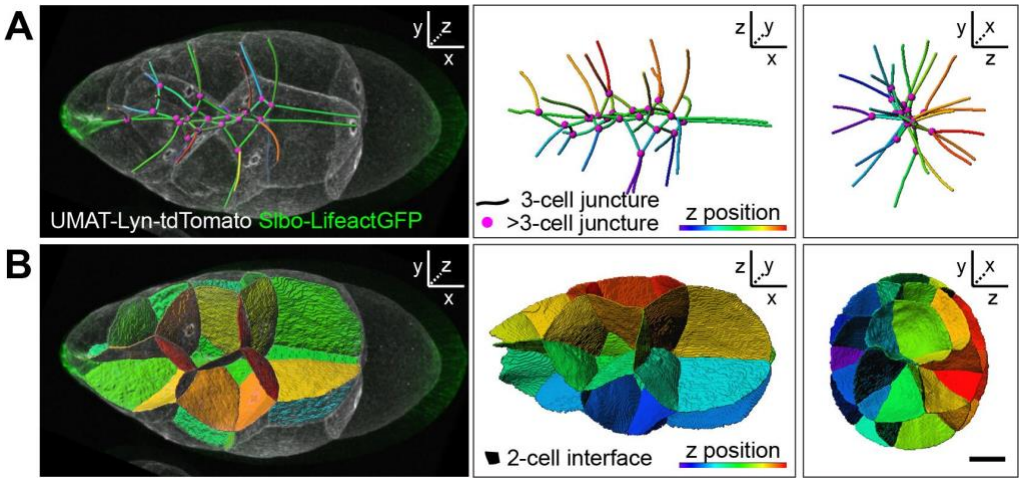

Fig. S11. Three dimensional reconstructions of nurse cell contacts

A second example for Fig.3A and C. (A) 3-nurse cell junctures are represented as lines and color provides position in z. Magenta dots represent junctures of >3 nurse cells. x,y planes (left panels), x,z planes (middle), and y,z planes (right panels) are shown. (B) Two-cell-contacts are shown as surfaces. Scale bar, 20 μm.

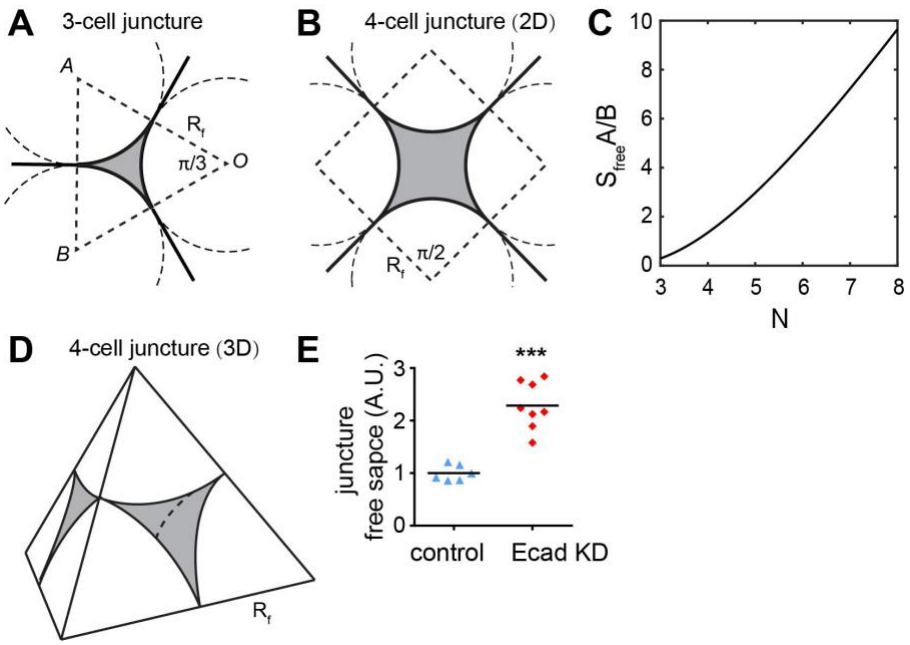

Fig. S12. Geometry of nurse cell junctures and associated free space

(A) The local configuration of 3-cell junctures in a 2D cross section. Nurse cell membranes are represented by solid black lines and R_f is the local radius of the nurse cell. The free space between the nurse cells, shaded gray, is the area of the polygon (OAB), a triangle in this case, minus the area of the circular sector with centers at A, B and O, multiplied by the number of nurse cells in the juncture. (B) The configuration of a 4-cell juncture in 2D. In this case, the polygon is a square. (C) S_{free} is a function of the balance between adhesion (A) energy gained and the cost of bending (B) nurse cell membranes and increases with increasing N at the junctures. Bending energy proved negligible (see ST2) (D) The configuration of a 4-cell juncture in 3D. The nurse cell membrane is represented by spherical surfaces that join together. The centers of the spheres are the vertices of a tetrahedron, which has edges with length $2R_f$. The volume of the free space, again shaded gray, is the volume of the tetrahedron minus the volume of the spherical caps. (E) Quantification of 3-cell junctures in 2D. n = 6, 8

pairs of junctions from 3 control and 4 ECad KD egg chambers. Bars show mean. ***, $P < 0.001$ (Mann-Whitney test), A.U. arbitrary unit. Scale bar, 20 μm.

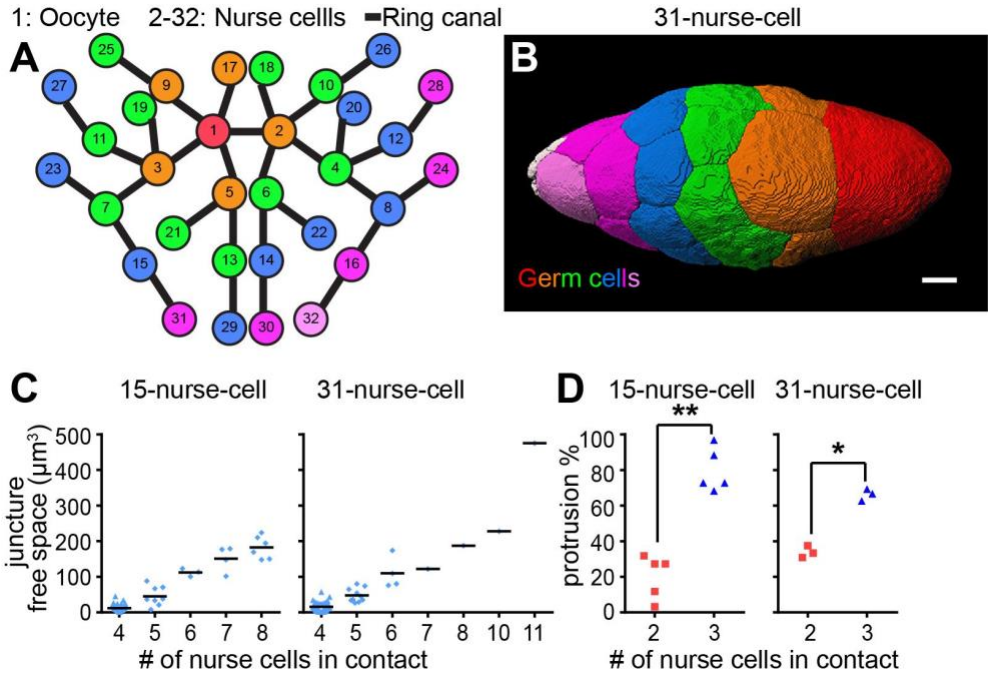

Fig. S13. Nurse cell arrangements in mutants with increased number of nurse cells

(A) Schematic of the pattern of ring canal (lines) connections between individual germ cells (numbers in circles) in a 31-nurse-cell egg chamber. (B) 3D reconstruction of germ cell packing in a 31-nurse-cell stage 9 egg chamber. Germ cells are color coded according to ring canal number, which also correlates with proximity to the oocyte (red cell, #1). Border cells are at the anterior tip in B and are pseudocolored in white. Scale bar, 20 μm. (C) Quantification of extracellular spaces filled with fluorescent dextran in control and 31-nurse-cell egg chambers (n = 7, 3 egg chamber). (D) Quantification of side protrusion preferences as a fraction of total protrusions in control (n=5) and 31-nurse-cell (n=3) movies. **, *P* <

0.01, *, $P < 0.05$ (paired t test). Neither intercellular spaces nor protrusion preference for 3-nurse-cell junctures was altered in 31-nurse-cell egg chambers.

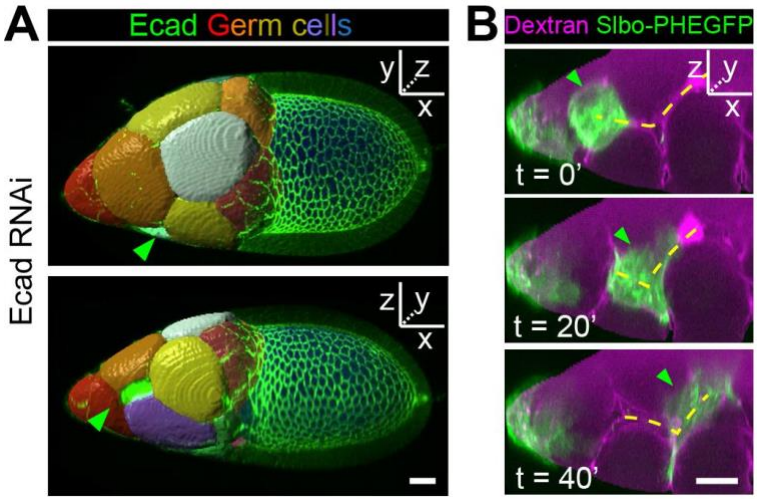

Fig. S14. Border cells prefer multiple cell junctures in egg chambers with reduced germline Ecad

(A) Three dimensional reconstructions of nurse cells in a fixed egg chamber with germline Ecad RNAi showing border cells in nurse cell/nurse cell/follicle cell grooves. (B) Still images from a movie showing border cells (green arrowhead) zig zagging(dashed yellow lines) along grooves. Yellow dashed line indicates the nurse cell junctions that the border cells migrate along. Green arrowhead points to the border cells. Scale bars, 20 μm.

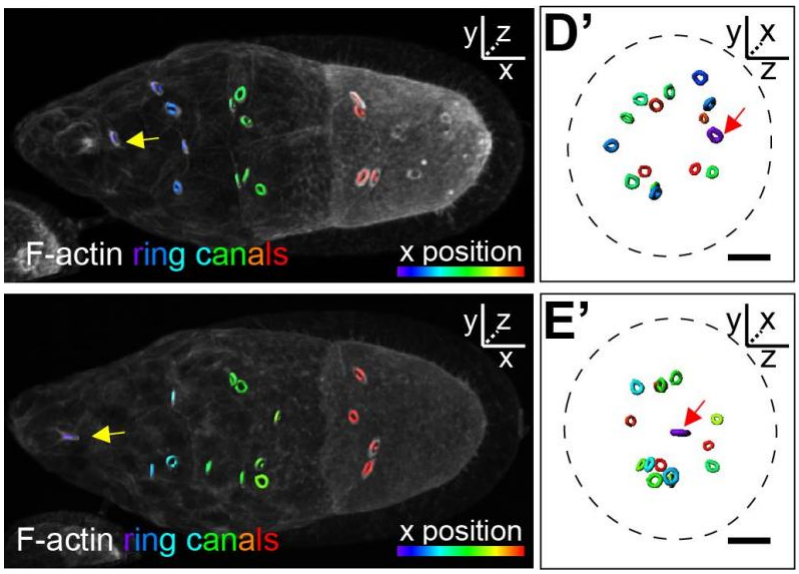

Fig. S15. Ring canals are neither necessary nor sufficient to steer border cells

Lateral and anterior 3D projection views of reconstructed 3D ring canals (colored circles) in early stage 9 egg chambers in which ring canals are absent (upper right panel) or present (lower right panel) in the central path. Scale bars, 20 μm.

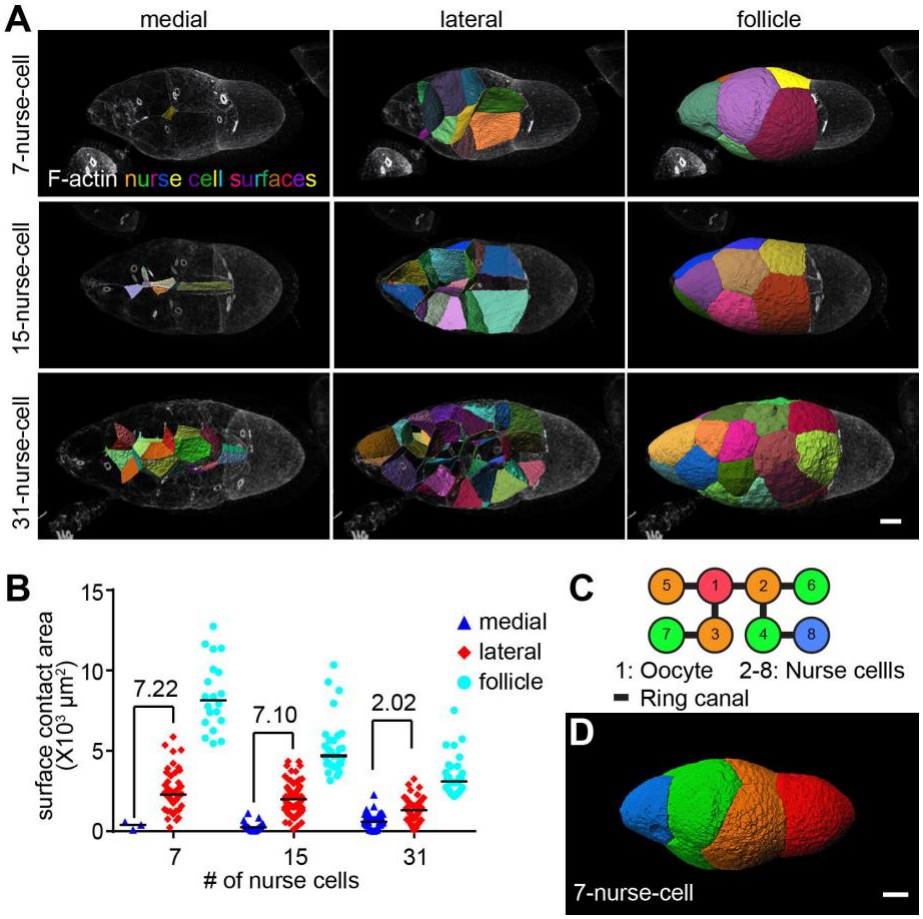

Fig. S16. The ratio of medial to lateral surface areas is not critical for border cell migration

(A) Lateral view of segmented 3D nurse cell surface-surface contacts in early stage 9 egg chambers. (B) Quantification of the areas of different types of nurse cell surface contacts. Each dot represents the area of the contact between a single nurse cell and a neighboring nurse cell or follicle cells. Numbers indicate the mean value normalized to that of the medial path in each genotype to compare relative differences between medial and lateral surface areas. Data from $n = 3, 2, 1$ early stage 9 egg chambers. Absolute size of medial surfaces: 15NC (mean ± SD = 286 ± 256) and 31NC (mean ± SD = 658 ± 462) are significantly different ($P < 0.0001$, unpaired t test). 15NC and 7NC (mean ± SD = 347 ± 247) are not

significantly different. Note there is only 1 medial surface in each 7NC egg chamber. (C) Schematic drawing of the pattern of ring canal (lines) connections between individual germ cells (numbers in circles) in a 7-nurse-cell egg chamber. (D) 3D reconstruction of germ cell packing in a 7-nurse-cell early stage 9 egg chambers. Germ cells are color coded according to ring canal number, which also correlates with proximity to the oocyte (red cell, #1). Scale bars, 20 μm.

2.12. Supplementary Tables

Table S1. List of fly stains used in this study

	Purpose	Genotype	Source	Reference
Fluorescent markers	border cell membrane marker	slbo-4XPHEGFP (III)	Hsin-Ho Sung	
		slbo-LifeactGFP	lab stock	
	nurse cell membrane marker	UMAT-Lyn-tdTomato (II) and (III)	Hsin-Ho Sung	(*29*)
	all cell nuclei marker	ubi-HisRFP	Hsin-Ho Sung	
	Ecad marker	y,w; shgGFP	BDSC 60584	
CRISPR KI	inject PVF1N1	w;vas-Cas9 (III)	BestGene 51324	
	inject PVF1N2, PVF1C, and KerenC	yw; nos-Cas9 (II-attp40)	BestGene	
	inject KerenN	y, vas-Cas9, w	BestGene 55821	
	inject SpitzN and SpitzC	yw; nos-Cas9 (III-attp2)	BestGene	
	remove scarless in KerenN, KerenC	w; 3XP3-ECFP, tub-PBac; MKRS/TM6B	BDSC 32070	

	remove scarless in PVF1N1, PVF1N2, PVF1C, SpitzN, and SpitzC	w; CyO, w+, tub-PBac/wg	BDSC 8283	
Gal4 drivers	border cell Gal4 driver	w; slbo-Gal4 (II)	lab stock	
		Gal80ts; Fruitless-Gal4/TM6B	lab stock	
		109C1-Gal4	BDSC 7020	
	somatic cell mosaic driver	hsFlp; Ay-Gal4, UAS-GFP	lab stock	
	stretch cell Gal4	w; c329b-Gal4/TM3	BDSC 3746	
	nurse cell Gal4	w; matalpha4-Gal4 (II)	BDSC 7062	
		nos-Gal4/CyO; bam-Gal80/TM6	Huynh Jean Rene	(*22*)
		Gal4::VP16	BDSC 64277	
UAS transgenes	PVR, EGFR inhibition	UAS-PVR[DN]; UAS-EGFR[DN]	lab stock	
		UAS-EGFR-RNAi/CyO; UAS-PVR-RNAi/TM6	lab stock	
	PVF1 overexpression	UAS-pvf1; UAS-pvf1/TM6B,Hu	lab stock	

	Ecad overexpression	UASp-EcadFL	lab stock	
		UAS-EcadGFP	lab stock	
RNAi	Ecad RNAi	shgRNAi (HMS00693)	BDSC 32904	(*17*)
		shgRNAi2 (V103962)	VDRC 103962	(*17*)
	shrub RNAi	shrubRNAi (HMS01767)	BDSC 38305	(*22*)
	cycE RNAi	cycERNAi (HMS00060)	BDSC 33654	(*28*)
	wRNAi	wRNAi	lab stock	
mutant	slbo	slbo[e7b]	lab stock	
		slbo[PZ01310]	lab stock	

Table S2. List of fly genotypes in each experiment

Figure	Panel	Group	Genotype
1	A-B	WT	w; slbo-4XPHEGFP, UMAT-Lyn-tdTomato/+
	D-E	HA-Keren	y,w/w; HA-Keren[N1]
	F	control	w; slbo-Gal4/+
		PVR[DN], EGFR[DN]	w; UAS-PVR[DN]/slbo-Gal4; UAS-EGFR[DN]/+
	G-J	control clone	hsFlp/w; Ay-Gal4, UAS-GFP/+; ubi-HisRFP, slbo-4XPHEGFP, UMAT-Lyn-tdTomato/+
		PVF overexpression in clone	hsFlp/UAS-pvf1; Ay-Gal4, UAS-GFP/+; ubi-HisRFP, slbo-4XPHEGFP, UMAT-Lyn-tdTomato/UAS-pvf1
	K	PVF overexpression in stretch cells	UAS-Pvf1/+; slbo-LifeactGFP/+; c329b-Gal4/UAS-LifeactRFP
2	A-B	control	w; matalpha4-Gal4/+
		Ecad RNAi	w/y,sc,v, sev; matalpha4-Gal4/+; shgRNAi (HMS00693)/+
		Ecad overexpression	w; matalpha4-Gal4/UASp-EcadFL
	C	WT	W1118

	D-E	WT	y,w; shgGFP
	F-G	control	matalpha4-Gal4/+;HA-Keren[N1]/+
		Ecad RNAi	matalpha4-Gal4/+;HA-Keren[N1]/shgRNAi (HMS00693)
	H-K	control	w; ubi-HisRFP, slbo-4XPHEGFP, UMAT-Lyn-tdTomato/+
		Ecad RNAi	matalpha4-Gal4/+; shgRNAi (HMS00693)/ubi-HisRFP, slbo-4XPHEGFP, UMAT-Lyn-tdTomato
3	A-D	WT	w; slbo-GaL4/UAS-LifeactGFP
	E	WT	w; UMAT-Lyn-tdTomato/+; UAS-HisRFP/slbo-LifeactGFP
	F-G	WT	w; matalpha4-Gal4/+
	H	WT	w; matalpha4-Gal4/+
		Ecad RNAi	w/y,sc,v, sev; matalpha4-Gal4/+; shgRNAi (HMS00693)/+
	I-K	WT	w; ubi-HisRFP, slbo-4XPHEGFP, UMAT-Lyn-tdTomato/+
4	G, I	control	w; slbo-Gal4/+
		31-NC	w/y,v; nos-Gal4/shrubRNAi; bam-Gal80/+
5	A	control	w; matalpha4-Gal4/+
		Ecad RNAi	w/y,sc,v, sev; matalpha4-Gal4/+; shgRNAi (HMS00693)/+
	B	Ecad RNAi	matalpha4-Gal4/+; shgRNAi (HMS00693)/ubi-HisRFP, slbo-4XPHEGFP, UMAT-Lyn-tdTomato
	C-D	PVR[DN], EGFR[DN]	w; UAS-PVR[DN]/slbo-Gal4, UAS-LifeactGFP; UAS-EGFR[DN]/+

	E	PVR[DN], EGFR[DN]	w; UAS-PVR[DN]/slbo-Gal4; UAS-EGFR[DN]/+
	F-G	WT	w; slbo-Gal4/+
	H-I	WT	w; ubi-HisRFP, slbo-4XPHEGFP, UMAT-Lyn-tdTomato/+
6	A	WT	w; slbo-GaL4/UAS-LifeactGFP
	B	WT	w; ubi-HisRFP, slbo-4XPHEGFP, UMAT-Lyn-tdTomato/+
	C-D	15-NC	w; UMAT-Lyn-tdTomato/+; UAS-HisRFP/slbo-LifeactGFP
		31-NC	w/y,v; nos-Gal4/shrubRNAi; bam-Gal80/+
	E-F	7-NC	cycERNAi/Gal4::VP16
		15-NC	w; slbo-GaL4/UAS-LifeactGFP
7	A-B	WT	w; UMAT-Lyn-tdTomato/+; UAS-HisRFP//slbo-4XPHEGFP

Table S3. List of fly genotypes in each supplementary experiment

Figure	Panel	Group	Genotype
S1	A-B	WT	w; slbo-4XPHEGFP, UMAT-Lyn-tdTomato/+
	C	WT	w; slbo-Gal4/+
S2	A	HA-Keren	y,w/w; HA-Keren[N1]
	B	WT	w1118
	C-D	HA-PVF1	HA-PVF1[N2]
S3	A	PVR[DN], EGFR[DN]	w; UAS-PVR[DN]/slbo-Gal4; UAS-EGFR[DN]/+
	B	control	w; slbo-Gal4/+; ubi-HisRFP, slbo-4XPHEGFP, UMA-TLyn-tdTomato/+
		PVR[DN], EGFR[DN]	w; UAS-PVR[DN]/slbo-Gal4; UAS-EGFR[DN]/ubi-HisRFP, slbo-4XPHEGFP, UMAT-Lyn-tdTomato
	C	Slbo-control	w; slbo-Gal4/+
		Slbo-DN	w; UAS-PVR[DN]/slbo-Gal4; UAS-EGFR[DN]/+
		Slbo-RNAi	w; UAS-EGFR-RNAi/slbo-Gal4; UAS-PVR-RNAi/+
		Fruitless-control	w; Gal80ts; Fruitless-Gal4/TM6B
		Fruitless-DN	w; Gal80ts/UAS-PVR[DN]; Fruitless-Gal4/UAS-EGFR[DN]

		Fruitless-RNAi	w; Gal80ts/UAS-EGFR-RNAi; Fruitless-Gal4/UAS-PVR-RNAi
		109C1-control	w;109C1-Gal4/+
		109C1-DN	109C1-Gal4; UAS-PVR[DN]/+; UAS-EGFR[DN]/+
		109C1-RNAi	109C1-Gal4; UAS-EGFR-RNAi/+; UAS-PVR-RNAi/+
	A	Ecad RNAi	matalpha4-Gal4/wRNAi; shgRNAi (HMS00693)/ubi-HisRFP, slbo-4XPHEGFP, UMA-TLyn-tdTomato
		control	matalpha4-Gal4/+; ubi-HisRFP, slbo-4XPHEGFP, UMA-TLyn-tdTomato/+
S4	B	Ecad RNAi	matalpha4-Gal4; shgRNAi (HMS00693)/ubi-HisRFP, slbo-4XPHEGFP, UMA-TLyn-tdTomato
S5	A-C	WT	W1118
S6		WT	y,w; shgGFP
		control	matalpha4-Gal4/+;HA-Keren[N1]/+
S7	A-B	Ecad RNAi	matalpha4-Gal4/+;HA-Keren[N1]/shgRNAi (HMS00693)
		control	shgRNAi2 (V103962)/+
		Ecad RNAi	shgRNAi2 (V103962)/+; c329b-Gal4/+
S8	A-E	Ecad OE	c329b-Gal4/UAS-EcadGFP
S9	A-B	slbo mutant	slbo[e7b]/slbo[PZ01310]; ubi-HisRFP, slbo-4XPHEGFP, UMAT-Lyn-tdTomato/+
S10	B	WT	w; slbo-GaL4/UAS-LifeactGFP

S11	A-B	WT	w; UMAT-Lyn-tdTomato/+; UAS-HisRFP/slbo-LifeactGFP
S12	E	WT	w; matalpha4-Gal4/+
		Ecad RNAi	w/y,sc,v, sev; matalpha4-Gal4/+; shgRNAi (HMS00693)/+
S13	B-C	control	w; matalpha4-Gal4/+
		31-NC	nos-Gal4/shrubRNAi; bam-Gal80/ubi-HisRFP, slbo-4XPHEGFP, UMAT-Lyn-tdTomato
	D	control	w; ubi-HisRFP, slbo-4XPHEGFP, UMAT-Lyn-tdTomato/+
		31-NC	nos-Gal4/shrubRNAi; bam-Gal80/ubi-HisRFP, slbo-4XPHEGFP, UMAT-Lyn-tdTomato
S14	A	Ecad RNAi	w/y,sc,v, sev; matalpha4-Gal4/+; shgRNAi (HMS00693)/+
	B	Ecad RNAi	matalpha4-Gal4/+; shgRNAi (HMS00693)/ubi-HisRFP, slbo-4XPHEGFP, UMAT-Lyn-tdTomato
S15		WT	w; slbo-GaL4/UAS-LifeactGFP
S16	A-B	7-NC	cycERNAi/Gal4::VP16
		15-NC	w; slbo-GaL4/UAS-LifeactGFP
		31-NC	w/y,v; nos-Gal4/shrubRNAi; bam-Gal80/+
	D-E	7-NC	cycERNAi/Gal4::VP16

Table S4. Predicted mature peptide and cleavage sites

Gene	Protein ID	N-terminal aa after cleavage before mature peptide	Mature peptide	C-terminal aa after cleavage after mature peptide
Keren	NP_524129.1	IFA	CPPTYVAWYCLNDGTCFTVKIHNEILYNCECALGFMGPRC	EYKEI
Spitz	NP_599118.2	TYK	CPETFDAWYCLNDAHCFAVKIADLPVYSCECAIGFMGQRC	EYKE
Pvf1	NP_523407	VRNATP for N1 and ATP for N2	ASCSPQPTIVELKPPAEDEANYYYMPACTRISRCNGCCGSTLISCQPTEVEQVQLRVRKVDRAATSGRRPFTIITVEQHTQCRC	

Inserted 2xHA sequence flanked by linkers:

QFALGGSGGSGGSGGSMYPYDVPDYAGYPYDVPDYAIKAGGSGGSGGSGGSKGEL

Table S5. CRISPR target sites

Keren N	TGGACAGGCGAAGATCGGGA
Keren C	AGCATCACACGGTTCCTGGT
Spitz N	GGGAATGTAATATTGGGCCT

Spitz C	AACATCGGACGCGGCCTCTT
Pvf1 N	GTTGCATTCCTCACGGTTGC
Pvf1 C	CCGCTGCGATTGCCGCACGA

Table S6. Primers for cloning CRISPR target into the pU6-BbsI-chiRNA vector

Keren N gF	CTTCGTGGACAGGCGAAGATCGGGA
Keren N gR	AAACTCCCGATCTTCGCCTGTCCAC
Keren C gF	CTTCGAGCATCACACGGTTCCTGGT
Keren C gR	AAACACCAGGAACCGTGTGATGCTC
Spitz N gF	CTTCGGGAATGTAATATTGGGCCT
Spitz N gR	AAACAGGCCCAATATTACATTCCC
Spitz C gF	CTTCGAACATCGGACGCGGCCTCTT
Spitz C gR	AAACAAGAGGCCGCGTCCGATGTTC
Pvf1 N gF	CTTCGTTGCATTCCTCACCGTTGC
Pvf1 N gR	AAACGCAACGGTGAGGAATGCAAC
Pvf1 C gF	CTTCGCCGCTGCGATTGCCGCACGA
Pvf1 C gR	AAACTCGTGCGGCAATCGCAGCGGC

Table S7. Primers for cloning left and right recombination arm into the pHD-2xHA-ScarlessDsRed vector.

Keren N1 LF	TAGCGGCCGCGAATTAAGTTGGCATGACTAGCGTTTATTG
Keren N1 LR	CACCAAGGGCGAATTGCGGGAAGGTGACATTCGG
Keren N1 RF	TTCCAAGGGCGAATTAATCTTCGCCTGTCCACCGAC
Keren N1 RR	AGGTTTAAACGAATTCAGCCTAAGGTGACGTCTCAG
Keren C1 LF	TAGCGGCCGCGAATTGATCACAACTAAGGCGAGC
Keren C1 LR	CACCAAGGGCGAATTGAATCTCCTTGTACTCGCACC
Keren C1 RF	TTCCAAGGGCGAATTAGATGGCTCGTACCTGCCAACTCGCAACCGTGTGATG
Keren C1 RR	AGGTTTAAACGAATTAGCACTGAAGTCCGCCTT
Spitz N1 LF	TAGCGGCCGCGAATTCGGAAAATAAACGCGGCTAACAG
Spitz N1 LR	CACCAAGGGCGAATTGGGGGAATGTAATATTCGGGCGGGGCGTGGTC
Spitz N1 RF	TTCCAAGGGCGAATTAACATACAAATGTCCGGAAACCT
Spitz N1 RR	AGGTTTAAACGAATTTTGGGTAGCATGCATCATTTT
Spitz C1 LF	TAGCGGCCGCGAATTAAATGGCTCAACTGGTGGACTG
Spitz C1 LR	CACCAAGGGCGAATTGGATCTCCTTGTATTCGCATCGC
Spitz C1 RF	TTCCAAGGGCGAATTAGACAATACTTACCTGCCCAAACGTCCGCGTCCGA
Spitz C1 RR	AGGTTTAAACGAATTCCACCCTTTTGATTGATTTGATTTG

Pvf1 N1 LF	TAGCGGCCGCGAATTTCGTGGTAAACATACGTTTTGAG
Pvf1 N1 LR	CACCAAGGGCGAATTGGGTTGCTGGAGATTGGG
Pvf1 N1 RF	TTCCAAGGGCGAATTAGTGAGGAATGCAACGCCG
Pvf1 N1 RR	AGGTTTAAACGAATTTACAGAGTGTGTGCCAGC
Pvf1 N2 LF	TAGCGGCCGCGAATTTAAAAATGCGATTCGCTTCCTGGAA
Pvf1 N2 LR	CACCAAGGGCGAATTGATTACGGACGGTTGCTGGAGATTGG
Pvf1 N2 RF	TTCCAAGGGCGAATTAGCAACGCCGGCGAGCTG
Pvf1 N2 RR	AGGTTTAAACGAATTCAGAGTGTGTGCCAGCAGTTG
Pvf1 C1 LF	TAGCGGCCGCGAATTCACTTCCTCTGCGATCGTTTGC
Pvf1 C1 LR	CACCAAGGGCGAATTGGCAGCGGCACTGCGTATGC
Pvf1 C1 RF	TTCCAAGGGCGAATTAGATTGTAGGACCAAGGCGGAGGACTGCA
Pvf1 C1 RR	AGGTTTAAACGAATTTCCCATTTTTGCCTCAACTCAGC

Table S8. List of CRISPR knockin of HA tag in mature chemoattractant ligand peptide

	pU6-BbsI-chiRNA vector	pHD-2xHA-ScarlessDsRed vector	signal in live staining	signal in fixed staining	homozygous viable
Keren N1	pU6 KerenN	pHD KerenN1	yes	no	yes
Keren C1	pU6 KerenC	pHD KerenC1	no	no	no
Spitz N1	pU6 SpitzN	pHD SpitzN1	no	no	no
Spitz C1	pU6 SpitzC	pHD SpitzC1	no	no	no
PVF1 N1	pU6 PVF1N	pHD PVF1N1	no	N.A.	N.A.
PVF1 N2	pU6 PVF1N	pHD PVF1N2	no	yes	yes
PVF1 C1	pU6 PVF1C	pHD PVF1C1	no	no	no

Table S9. Adhesion energy cost for N-cell junctures (in unit of the adhesion strength *A*)

	$W_{adh,2}$	$W_{adh,3}$	$W_{adh,4}$	$W_{adh,5}$	$W_{adh,6}$	$W_{adh,7}$	$W_{adh,8}$
value	*6.3 A*	*4.9 A*	*3.8 A*	*2.8 A*	*1.9 A*	*1.1 A*	*0.3 A*

Table S10. Model parameters.

	c_m	L	ξ	r_0	c_2	α	β_1	β_2
value	10	140 μm	42 μm	10 μm	1	80	0.4	0.2

Table S11. Parameter scanning of α and β_1. Values in the table correspond to posterior and medial migration index and are color coded with red/green corresponding to low/high values. The parameter values used in wild-type simulations are underlined.

% posterior		β_1										
		0	0.1	0.2	0.3	0.4	0.5	0.6	0.7	0.8	0.9	1
α	0	35	57	72	87	91	92	92	91	92	92	92
	10	37	57	76	87	91	92	92	92	92	92	92
	20	41	57	82	89	91	92	92	92	92	92	92
	30	42	59	78	91	92	92	92	93	92	92	92
	40	43	57	78	91	91	92	92	92	93	93	92
	50	46	61	76	89	91	92	92	92	92	92	92
	60	45	61	72	87	91	92	92	92	92	93	93
	70	46	58	74	84	90	92	92	92	93	92	93
	80	48	60	67	81	<u>91</u>	92	92	92	92	92	93
	90	49	59	70	79	86	92	92	92	93	93	92
	100	50	59	67	74	86	90	92	92	92	93	93
%		β_1										

	medial	0	0.1	0.2	0.3	0.4	0.5	0.6	0.7	0.8	0.9	1
	0	40	53	59	61	58	59	61	65	70	71	71
	10	58	60	63	66	67	74	73	73	74	72	76
	20	64	69	74	70	73	79	76	76	80	78	78
	30	71	74	78	77	77	81	78	81	82	84	79
	40	69	78	80	83	83	82	82	85	82	87	82
α	50	83	82	82	83	84	84	87	84	87	87	85
	60	85	87	86	86	86	86	87	85	86	86	88
	70	88	87	88	86	87	88	88	88	88	88	89
	80	89	89	89	87	87	87	87	89	88	88	89
	90	88	88	89	88	87	89	89	89	90	89	89
	100	90	90	90	88	89	88	89	88	90	89	90

2.13. Multimedia Files

Movie 1. Confocal time-lapse imaging of normal border cell migration. SlboGal4 drives UAS-mCD8-EGFP (green) and UAS-RFPnls (magenta).

Movie 2. "Fly-through" from the anterior tip of the egg chamber where the border cells are located to oocyte border, using near isotropic light sheet imaging showing the nurse cell membranes encountered by the border cells as they migrate. Multiple nurse cells meet in the center of the egg chamber where there is high membrane curvature. Border cells encounter ~40 side paths along the way. Green, E-cadherin. Magenta, F-actin. Scale bar, 20 μm.

Movie 3. Confocal time-lapse imaging of border cell migration with germline knockdown of E-cadherin. Matalpha4-Gal4;UAS-EcadRNAi. Green, Slbo-PHEGFP; magenta, UMAT-Lyn-tdTomato.

Movie 4. (Fig. 2H and I) (A) Confocal time-lapse imaging of a nurse cell juncture pulled by incoming border cell cluster in a control egg chamber. Green, Slbo-PHEGFP; magenta, UMAT-Lyn-tdTomato, Ubi-HisRFP. Note that the juncture shown by the yellow filament is just an example. Other junctures that the border cells contact are also deflected. In the first and last time points, tracking is removed to show the original membrane signal. (B) Confocal time-lapse imaging of an egg chamber with germline knockdown of E-cadherin (Matalpha4-Gal4;UAS-EcadRNAi) showing absence of nurse cell membrane deflection when border cell protrusions touch nurse cell membranes. Despite touching the nurse cell juncture multiple times, the border cell protrusion did not deflect it (one juncture is highlighted by the yellow filament). In the first and last time points, tracking is removed to show the original membrane signal.

Movie 5. (Fig. 3A and C) Animation of 3-dimensional reconstruction of different types of nurse cell contacts in a stage 9 egg chamber. Green, Slbo-LifeactGFP; white, F-actin or F-actin with outer follicle cell signal masked. Two-cell-contacts are shown as surfaces and color represents position along the z axis. Three-nurse cell junctures are represented as lines and color provides position in z. Magenta dots represent junctures of >3 nurse cells. First F-actin (white) and border cells (green) are shown. Then outer-follicle cell F-actin signals are masked to show nurse cell contacts. Then 2-cell surfaces are shown in 360 degree rotation, followed by >=3 cell juncture views in another 360 degree rotation.

Movie 6. (Fig. 4A) Simulation of border cell migration with nurse cell geometry and anterior-posterior chemoattractant gradient.

Movie 7. (Fig. 5B, fig. S14B). A confocal time-lapse movie of border cell migration in germline knockdown of E-cadherin. Border cells migrate along nurse-cell/nurse-cell/follicle-cell paths instead of nurse-cell/follicle-cell. Green, Slbo-PHEGFP; magenta, dextran.

Movie 8. (Fig. 6A, fig. S10B) Animation of 3-dimensional reconstruction of nurse cells and ring canals in a stage 9 egg chamber. White, F-actin; green, Slbo-LifeactGFP; blue, Hoechst. Nurse cell color indicates connection distance to the oocyte (red). White, border cells at the anterior tip. Yellow circles, ring canals.

The egg chamber was stained to show F-actin (white), border cells (green), and nuclei (blue). First the reconstructed nurse cells rotate 360 degree to show that nurse cells that connect closer to the oocyte (red) are located more posteriorly. Then the ring canals (yellow) are shown to display their location in between connected nurse cells.

Movie 9. (Fig. 7A) A confocal time-lapse movie of wild-type border cell migration. Note the dorsal migration prior to reaching the oocyte boundary. Green, Slbo-PHEGFP; white, UMAT-Lyn-tdTomato.

Movie 10. (Fig. 7C) Simulation of border cell migration with nurse cell geometry and anterior-posterior chemoattractant gradient and dorsal Grk gradient.

3. Collective border cell migration requires the Zn^{2+} transporter Catsup to promote endoplasmic reticulum-associated protein degradation

This chapter is adapted from an unpublished work: Xiaoran Guo, Alba Torres Espinosa, Wei Dai and Denise J. Montell. "Collective border cell migration requires the Zn2+ transporter Catsup to promote endoplasmic reticulum-associated protein degradation".

3.1 Introduction

Collective cell migration has emerged as a key driver of normal organ development, wound repair, and tumor metastasis[7,10,104,105]. Border cell migration in the *Drosophila* ovary provides a powerful *in vivo* model that is amenable to unbiased genetic screening. *Drosophila* ovaries are composed of ovarioles, which are strings of egg chambers progressing through 14 stages of development to mature eggs (Fig.8A). Each egg chamber is composed of 16 germ cells, including 15 nurse cells and one oocyte, which are surrounded by epithelial follicle cells. During stage 9 (Fig.8B), 4-8 border cells are specified at the anterior end of the egg chamber, delaminate from the follicular epithelium, and migrate posteriorly during developmental stage 9, reaching the anterior border of the oocyte by stage 10.

Genetic screens have yielded insights into the molecular mechanisms that specify which of the ~850 follicle cells acquire the ability to migrate[106,107], the developmental timing of their migration[108,109], direction sensing [90] [91] [110], and cytoskeletal dynamics[88,90,96,102,103,111–116]. Border cell studies continue to provide new biological insights[83,110,117–129]. The gene *Catsup* was identified both in a large-scale ethyl methanesulfonate mutagenesis screen for border cell migration defects in mosaic clones[130] and in a whole-genome expression profile of border cells[131].

The name *Catsup* is an abbreviation of "*Catecholamines up*", loss of which increases synthesis of aromatic amines including neurotransmitters such as epinephrine and dopamine[132]. Catsup is required for *Drosophila* tracheal morphogenesis, and in this context, it directly binds and inhibits the *Drosophila* homolog of tyrosine hydroxylase Ple to limit dopamine synthesis[133]. In contrast, in wing imaginal disc cells, Catsup regulates Notch and EGFR abundance and localization[134].

Catsup shares 62% similarity and 53% identity with its mammalian homolog ZIP7 (also known as SLC39A7 or HKE4)[134], a member of one of the two major families of Zn^{2+} transporters[135]. ZIP7 is located within the endomembrane system including the ER where it transports Zn^{2+} to the cytosol[136]. Zn^{2+} is a necessary trace element vital for many proteins to function, and Zn^{2+} homeostasis is carefully maintained by 24 Zn^{2+} transporters in humans, 14 of which are ZIPs[137]. ZIP7 is conserved throughout eukaryotes, and its loss causes ER stress in organisms as diverse as yeast, plants, and animals[138–143]. However, the relationships between ER stress, Zn^{2+} transport, Notch and EGFR localization and activity, and cell motility remain to be clarified. Here we study Catsup function in border cells. Together with published results, our data suggest a unified model for Catsup/ZIP7 in

providing rate-limiting Zn^{2+} for degradation of ER-localized misfolded proteins, thereby alleviating ER stress to promote cell survival, migration, and Notch transcriptional responses.

3.2. Catsup localizes with ER in the drosophila ovaries

To study the roles of Catsup in the ovary, we first examined its expression using a Catsup::GFP fusion protein expressed under endogenous genomic regulatory sequences[144]. Catsup::GFP was expressed throughout oogenesis, including in all follicle cells (Fig. 8A-B). Mammalian ZIP7 localizes predominantly to the ER[136], and both over-expressed CatsupV5 (Fig. 8C-K) and Catsup::GFP (Fig. 8L-T) significantly co-localized with the ER resident protein-folding enzyme, Protein Disulfide Isomerase **(**PDI), but not with DNA or F-actin, consistent with earlier findings in wing imaginal discs[134].

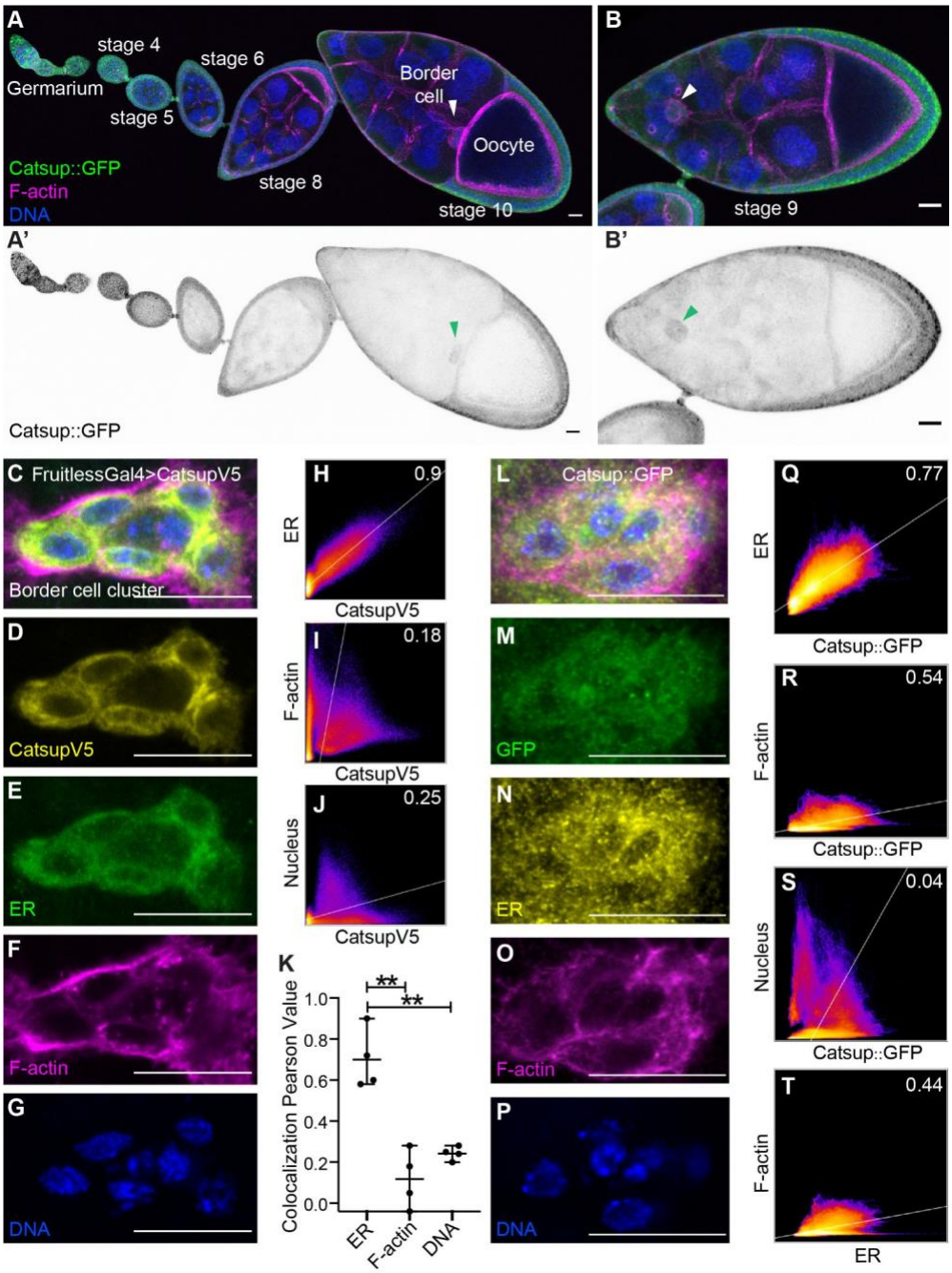

Fig. 8. Catsup expression and subcellular localization in the Drosophila ovary

(A, B) Developing egg chambers from the germarium to developmental stage 10, expressing Catsup::GFP and stained for DNA with Hoechst (blue) and F-actin with phalloidin (magenta). Border cells (white arrowheads) migrate during stage 9 (B) and complete their

migration by stage 10 (A). (A', B') The single Catsup::GFP channel (grayscale). (C-G) High magnification of a border cell cluster showing the localization of overexpressed CatsupV5 (yellow), anti-PDI staining for ER (green), phalloidin (magenta), and Hoechst (blue). (H-J) 2-dimensional intensity histograms for two selected channels showing colocalization of CatsupV5 relative to ER, F-actin, and DNA. The colocalization regression Pearson's coefficient is displayed in the upper right corner. (K) Comparison of Pearson's coefficients (average of 4 border cell clusters). ** P value < 0.01. (L-P) High magnification of a border cell cluster showing the localization of tagged Catsup::GFP expressed under endogenous regulatory sequences (green), ER (PDI, yello), F-actin (phalloidin, magenta) and nuclear DNA (Hoechst, blue). (Q-T) 2-dimensional intensity histograms for two selected channels showing the colocalization and the Pearson's coefficient for Catsup::GFP relative to ER, F-actin, nuclei, as well as ER relative to F-actin. Scale bars, 20 μm.

3.3. Catsup is important for border cell migration

Border cell clusters are composed of 4-6 migratory cells that surround and carry two non-migratory polar cells. Expression of a Catsup RNAi line in outer, migratory border cells using fruitlessGal4[145] inhibited migration (Fig. 9A). The defect was rescued by co-expression of UAS-CatsupV5 (Fig. 9B). Reduction of Catsup::GFP confirmed the effectiveness of the RNAi (Fig. 9C, C' and D, D'). Border cell migration was also impaired when Catsup RNAi was driven by c306Gal4 (Fig. 9E), which is expressed in both polar and migratory cells. FruitlessGal4-driven RNAi impaired border cell migration at least as much as c306Gal4, indicating that Catsup was primarily required in the outer, migratory cells (Fig. 9E).

As a further test of cell autonomy, we used the FLP-FRT system to generate mosaic egg chambers with clones of homozygous *Catsup* mutant cells. No migration was detected in homozygous mutant polar cells (Fig. 9F). However, when border cell clusters contained homozygous mutant outer border cells, migration was impaired. Furthermore, the magnitude of the defect correlated with the proportion of mutant cells (Fig. 9G-H). In clusters containing both heterozygous and homozygous mutant cells, homozygous mutant cells tended to occupy rear positions (Fig. 9I-J), which is typical of mutations in genes required autonomously for motility[146]. We conclude that Catsup is required in outer, migratory border cells for motility.

Catsup mutant wing disc epithelial cells are prone to apoptosis[134], and we observed that 33% (112/337) of *Catsup* mutant follicular epithelial cells were positive for cleaved and activated caspase, which is indicative of cells undergoing apoptosis. However, we never detected cleaved caspase in *Catsup* mutant border cells (0/32), indicating that border cells are more resistant to death, consistent with our earlier report that border cells mutant for *thread*, which encodes the *Drosophila* inhibitor of apoptosis protein (DIAP1), are viable[147].

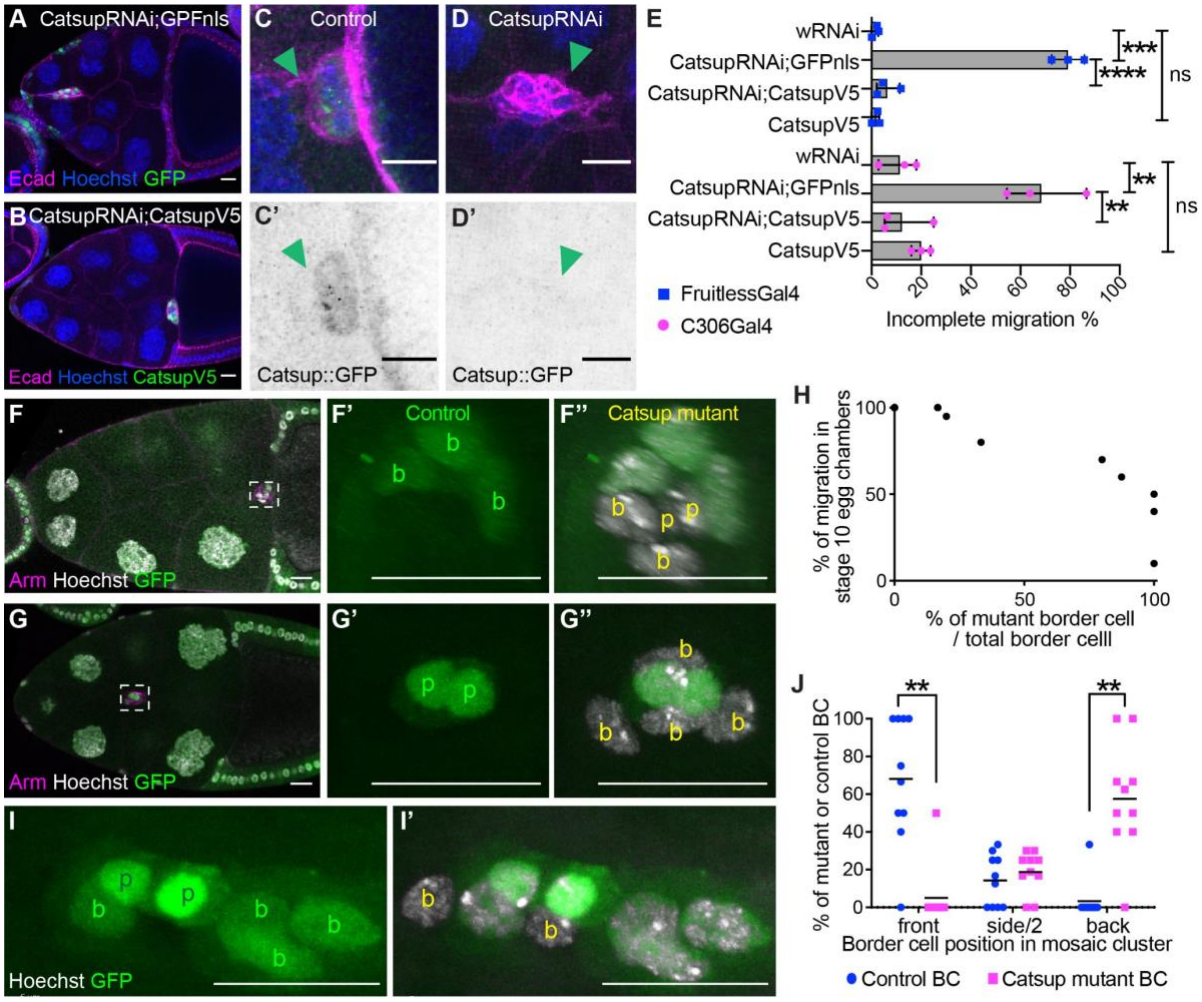

Fig. 9. Border cells require Catsup for normal migration

(A, B) Confocal micrographs of stage 10 egg chambers in which fruitlessGal4 drives expression UAS-Catsup RNAi and (A) UAS-GFPnls or (B) UAS-CatsupV5 in outer, migratory border cells. (C-D') Catsup::GFP expression in control border cells (C, C') or knocked down by c306Gal4>CatsupRNAi (D, D'). (E) Quantification of incomplete migration at stage 10 in fruitlessGal4 (blue) and c306Gal4 (magenta) driving the indicated transgenes. Experiments were independently replicated 3 times. (F-F") An egg chamber with GFP-negative (homozygous *Catsup* mutant) cells. Both polar cells (p) and two border cells (b) are mutant. (G-G") An egg chamber in which all outer border cells are GFP-negative

(homozygous *Catsup* mutant). (H) Migration distance expressed as a percentage of the migration path for mosaic border cell clusters as a function of the proportion of homozygous mutant cells in each cluster. (I) High magnification view showing the spatial distribution of Castup+ (GFP+) and Catsup-/- (GFP-/-) cells in a migrating cluster. (J) Quantification of the percentage of Catsup+ vs Catsup-/- border cells in the front, side, or back of the border cell cluster showing that Catsup-/- cells are more likely to occupy a rear position. “p” indicated polar cells, “b” indicated border cells, green labels control cells, yellow labels mutant cells. ** $P \leq 0.01$, *** $P \leq 0.001$, **** $P \leq 0.0001$. Scale bars, 20 μm.

3.4. Catsup loss of function changes Notch and EGFR protein abundance

One known function of Catsup is direct binding and inhibition of the tyrosine hydroxylase Ple, which is the rate-limiting enzyme in catecholamine synthesis[148]. Ple and Catsup are expressed in embryonic tracheal cells, where they contribute to achieving proper dopamine levels, which regulate Breathless (fibroblast growth factor receptor) endocytosis and signaling[133]. To test whether Catsup functions similarly in border cell migration, we used an antibody to assess Ple expression in wild-type egg chambers. In contrast to tracheal cells, we detected no Ple protein in wild-type egg chambers (Fig. 10A). The antibody was effective because we could detect Ple ectopically expressed using c306Gal4 (Fig. 10B), as well as endogenous expression of Ple in neurons in the adult brain[149] (Fig. 10C). Therefore, it is unlikely that negative regulation of Ple activity is the key function of Catsup in border cells, suggesting that its role in border cell migration is distinct from its role in tracheal development.

In wing imaginal disc epithelia, multiple transmembrane receptor proteins, including Notch and EGFR, accumulate abnormally in *Catsup* mutant cells[134]. We similarly found abnormal intracellular accumulation of Notch in follicle cells generally (Fig. 10D, D') and border cells specifically (Fig. 10E, E') upon Catsup knockdown. Cells lacking Catsup also exhibited defective Notch transcriptional activity, detected by the Notch responsive element reporter[150] (Fig. 10F, F'). Since Notch signalling is essential for border cell migration, and expression of constitutively active Notch (the Notch intracellular domain, NICD), which does not require intracellular trafficking, ligand binding, or processing, rescues impaired Notch signaling in border cells[151], we asked whether NICD could rescue Catsup knockdown. However, neither NICD expression nor overexpression of the Notch specific chaperone O-fucosyltransferase-1[152] was sufficient to rescue Catsup RNAi (Fig. S3.1). As in imaginal discs, EGFR also accumulated abnormally in Catsup RNAi-expressing border cells (Fig. 10G, G') and epithelial follicle cells (Fig. 10H, H'), whereas E-Cadherin was unaffected (Fig. 10I, I'). From these observations, we conclude that Catsup prevents intracellular accumulation of particular transmembrane proteins and promotes Notch signaling, migration and survival in multiple cell types and organisms.

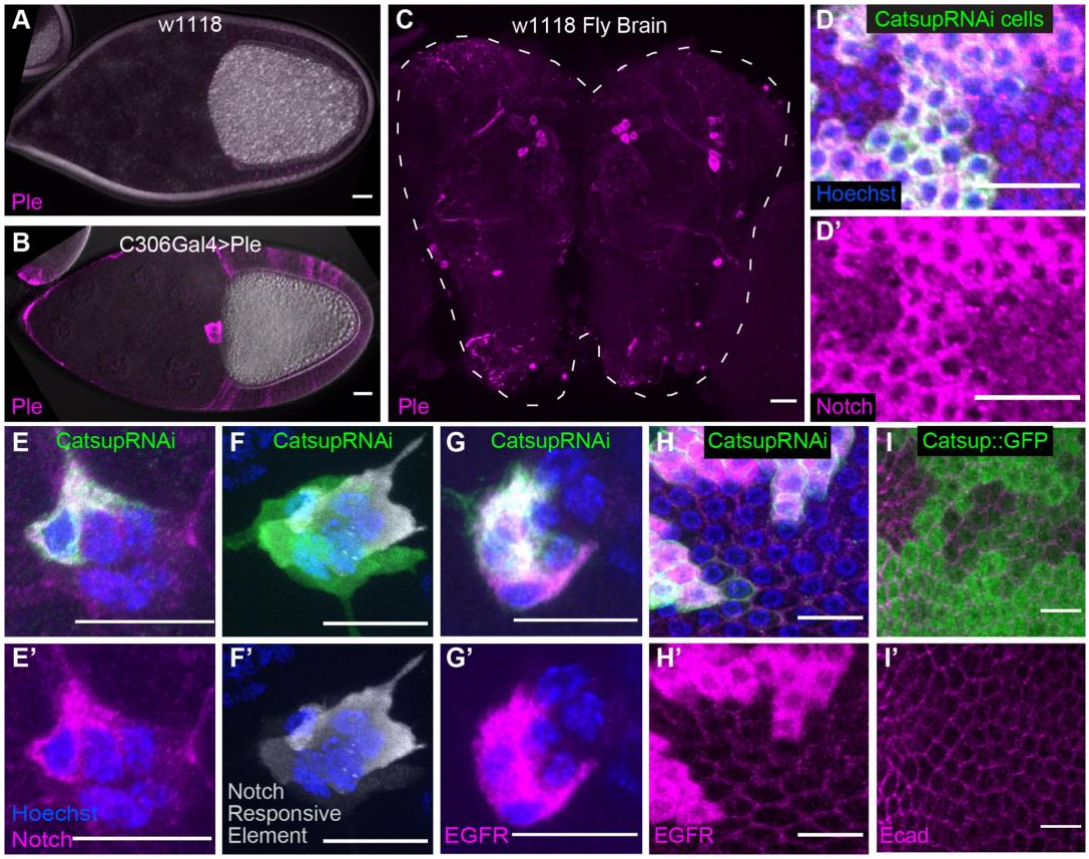

Fig. 10. Altered Notch and EGFR abundance and localization in cells expressing CatsupRNAi

(A, B) Differential interference contrast images of stage 10 egg chambers stained for Ple (magenta) in the w^{1118} control (A) or an egg chamber expressing UAS-Ple with c306Gal4 (B). (C) A dissected fly brain stained for endogenous Ple: dopaminergic neurons are Ple-positive. (D-E') CatsupRNAi-expressing clones (GFP-positive, green) accumulate intracellular Notch protein in epithelial follicle cells (D, D') and border cells (E, E') relative to neighboring wild type cells. (F, F') CatsupRNAi-expressing border cells (GFP-positive, green) show decreased Notch signaling shown by the Notch-responsive-element driving RFP (white) relative to neighboring wild type cells. (G-H') Accumulation of EGFR (magenta) in CatsupRNAi-expressing border cells (G, G') and epithelial follicle cells (H, H'). (I, I')

c306Gal4>CatsupRNAi reduces Catsup::GFP expression but does not cause E-cadherin (magenta) intracellular accumulation. Scale bars, 20 μm.

3.5. Catsup mutant causes ER stress

The abnormal intracellular accumulation of Notch and EGFR suggested possible disruption of ER protein-folding homeostasis (a condition commonly referred to as "ER stress") and activation of the unfolded protein response (UPR). To test if Catsup knockdown induces the UPR in follicle cells, we compared expression of the ER stress marker Xbp1::EGFP[153] in mosaic border cell clusters composed of heterozygous *Catsup*$^{+/-}$ and homozygous *Catsup*$^{-/-}$ mutant cells. We found high levels of Xbp1 in *Catsup*$^{-/-}$ but not *Catsup*$^{+/-}$ border cells (Fig. 11A-A"). Consistent with this result, we observed increased expression of PDI (Fig. 11B-B"). Accumulation of XBP1 and PDI are indicative of induction of an adaptive UPR[154]. This effect was rescued by co-expression of CatsupV5 (Fig. 11C-C"). These results show that cells lacking Catsup experience ER stress and impaired migration, suggesting that the ER stress itself might inhibit motility.

To test whether ER stress impairs border cell migration, we expressed a misfolded rhodopsin protein Rh1^{G69D}, known to induce ER stress[155] As expected, Rh1^{G69D} induced Xbp1 expression in border cells (Fig. 11D insert). Notably, Rh1^{G69D} expression also blocked migration (Fig. 11D), showing that high levels of a misfolded protein in the ER and the ensuing ER stress are sufficient to inhibit motility. Since loss of Catsup caused ER stress, we wondered if Catsup over-expression might suppress ER stress. Interestingly, overexpressing CatsupV5 rescued Rh1^{G69D}-induced Xbp1 expression (Fig. 11E, F) and border cell migration

(Fig. 11E and G). These results suggest that Catsup is a limiting factor for preventing ER stress, which hinders cell motility.

The UPR reinstates ER homeostasis by upregulating the protein-folding capacity of the ER and increasing its protein-degradation capacity[156]. During ERAD, misfolded proteins are extruded from the ER, ubiquitinated, and degraded by the proteasome[154].To test whether Catsup overexpression might enhance ERAD, we examined $Rh1^{G69D}$ protein abundance in cells over-expressing Catsup. Catsup overexpression reduced $Rh1^{G69D}$ protein to an undetectable level (Fig. 11D, E) suggesting that Catsup function is limiting for ERAD.

To distinguish whether ER stress disrupts trafficking of Notch and EGFR, we examined Notch and EGFR abundance and localization in $Rh1^{G69D}$-expressing cells. Notch abundance and localization were normal in $Rh1^{G69D}$-expressing epithelial follicle cells (Fig. 11H, H') and border cells (Fig. 11I, I') as were EGFR expression and localization (Fig. 11J-K'). This result suggests that ER stress per se does not disrupt Notch or EGFR trafficking, which has previously been suggested as an interpretation of the Catsup mutant phenotype.

Interestingly, despite normal localization and abundance of Notch in these cells, Notch signaling was nevertheless impaired (Fig. 11L, L'). Thus ER stress induced by accumulation of a misfolded ER client protein does not affect Notch or EGFR proteostasis but does impair Notch transcriptional activity. This finding is consistent with an earlier study that identified a pharmacological inhibitor of ZIP7 in a screen for compounds that block transcriptional responses to over-expressed NICD [157], which does not require Notch trafficking through the ER, cell surface expression, ligand binding, or proteolytic activation, although the authors concluded that ZIP7 promotes Notch trafficking[157]. Our results imply that ER stress

reduces NICD transcriptional activity, whether caused by Catsup mutation, $Rh1^{G69D}$ expression, or ZIP7 pharmacological inhibition.

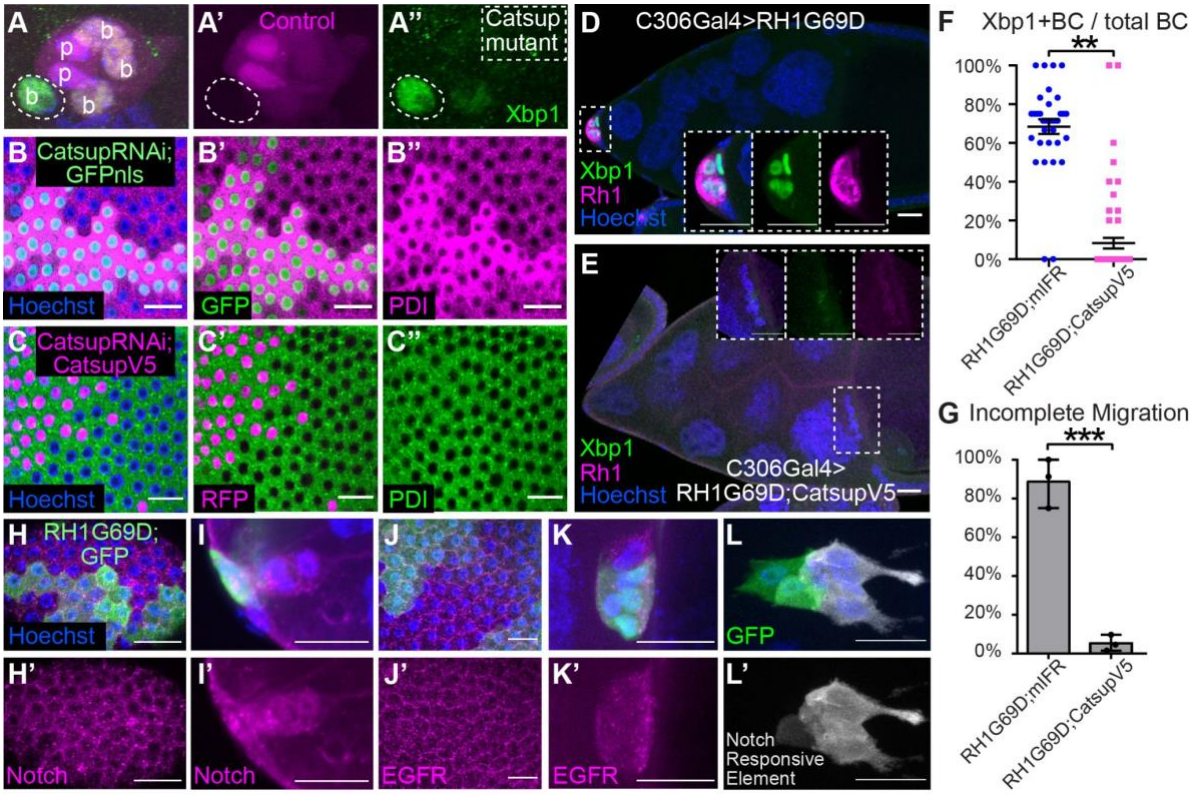

Fig. 11. ER stress in *Catsup* mutant border cells

(A) A mosaic border cell cluster composed of a mixture of control cells (RFP-positive, magenta which can be $Catsup^{+/+}$ or $Catsup^{-/+}$) and homozygous *Catsup* mutant cells (RFP-negative, outlined). Polar cells (p) express a higher level of RFP compared to outer border cells. Xbp1::EGFP (green), a marker for ER stress. (B-B'') Mosaic follicle cell clones expressing CatsupRNAi and GFPnls caused ER expansion shown by PDI (magenta). (C-C'') Mosaic clone expressing CatsupRNAi and CatsupV5 and RFP (magenta). (D) Expression of a misfolded rhodopsin protein $Rh1^{G69D}$ (magenta) in border cells induced ER stress (Xbp1::EGFP in green) and blocked border cell migration. (E) Co-expressing CatsupV5

reduced the Rh1^{G69D} protein level (magenta) and Xbp1::EGFP and rescued migration. (F) The percentage of border cells expressing RH1^{G69D} that are Xbp1 positive, in the absence (blue dots) or presence (pink dots) of CatsupV5 rescue. mIFR is a control, irrelevant fluorescent protein. (G) CatsupV5 rescue of RH1^{G69D} migration defect. (H-L) Mosaic clones expressing RH1^{G69D}; GFP shows comparable Notch intensity in epithelial clones (H, H') and a border cell clone (I, I'); EGFR intensity in epithelial clones (J, J') and a border cell clone (K, K'); The Notch responsive element reporter shows Notch transcriptional activity (white) in wild type but not RH1^{G69D} expressing border cells (L, L'). ** P≤0.01, **** P≤0.0001. Scale bars, 20 µm.

3.6. Zn^{2+} transportation and ER homeostasis

ZIP7 resides in the ER membrane and transports Zn^{2+} from the ER to the cytosol[158]. To test whether the Zn^{2+} transporter activity of Catsup was important for border cell migration, we introduced point mutations, H315A and H344A, which replace histidine residues that are required for Zn^{2+} transport and are conserved between Catsup, ZIP7 and a more distant family member from *Arabidopsis* IRT1 (Fig. 12A and Fig. S3.2). As controls, we engineered Catsup^{H187A} and Catsup^{H183A} mutants that do not affect Zn^{2+} transport in IRT1 [159]. We generated transgenic flies expressing the mutants under Gal4/UAS control and included a V5 tag so that we could monitor protein abundance and localization. We then co-expressed each of these RNAi-resistant transgenes with CatsupRNAi and evaluated protein expression and border cell migration (Fig. 12B-E). The point mutations that do not disrupt Zn^{2+} transport, Catsup^{H187A} and Catsup^{H183A}, were able to rescue border cell migration to nearly wild type levels (Fig. 12F) whereas neither Castup^{H344A} nor Catsup^{H315A} provided significant rescue (Fig. 12F). All the proteins were stably expressed and correctly localized to the ER (Fig.

12B-E), therefore the lack of rescue was likely a consequence of impaired transporter activity rather than impaired expression, localization, or another function. Similarly, the Zn^{2+}-transport-deficient proteins failed to rescue accumulation of Notch and EGFR (Fig. 12G-J') whereas $Catsup^{H187A}$ and $Catsup^{H183A}$ (Fig. 12K-N') did. From these experiments, we conclude that Zn^{2+} transport is an essential function of Catsup in promoting ERAD.

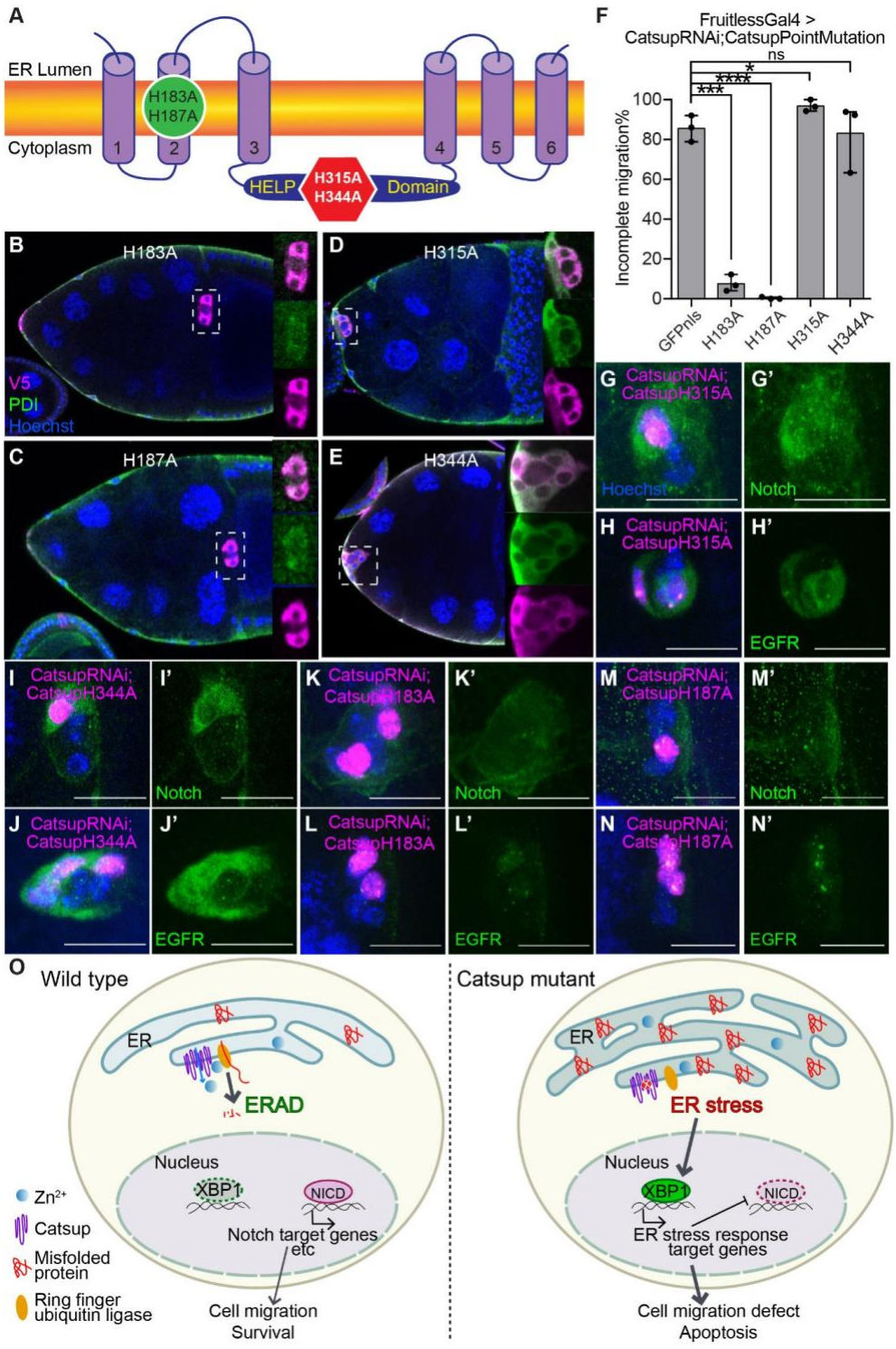

Fig. 12. Point mutations suggest requirement for Zn^{2+} transport in ER homeostasis and cell motility

(A) Schematic representation of transmembrane domains and topology for Catsup. Point mutations H183A and H187A reside within the second transmembrane domain while H315A and H344A are within the HELP domain required for Zn^{2+} transport. (B-E) Expression and co-localization of V5-tagged, RNAo-resistant Catsup mutants with the ER marker PDI (green) in border cells. (F) Quantification of incomplete migration at stage 10 in egg chambers expressing CatsupRNAi together with the indicated mutant forms. Experiments were independently repeated three times. (G-N') Mosaic expression of CatsupRNAi together with the indicated mutant forms of Catsup marked by RFPnls (magenta) and stained for Notch or EGFR in green, as indicated. Scale bars, 20 μm. (O) Model for the function of Catsup/ZIP7.

3.7. A model for Catsup/ZIP7 function: local Zn^{2+} transport is limiting for ERAD and mitigation of ER stress

In this study we explored the roles of the multifunctional protein Catsup in the *Drosophila* ovary. Catsup is named for its role in the negative regulation of catecholamine biosynthesis. Prior to the current work, diverse functions have been attributed to ZIP7 orthologs at the biochemical, cellular, tissue, and organ levels. This study, together with the published literature, suggests that a more general function of Catsup and its orthologs is in ER homeostasis (Fig. 12O). Catsup is a conserved protein that goes by names including ZRT1 in yeast, IRT1 in plants, and SLC39a7/Zip7/Ke4 in mammals. While many studies come to a common conclusion that loss or inhibition of Catsup/ZIP7 disrupts ER homeostasis, we add several new insights. We show that the cause of ER stress upon Catsup/ZIP7 knockdown is accumulation of misfolded/unfolded proteins due to disruption of ERAD and that Catsup overexpression is sufficient to resolve ER stress by degrading ectopically expressed $Rh1^{G69D}$.

ERAD requires a complex machinery involving dozens of proteins responsible for recognizing misfolded proteins in the ER, extruding them to the cytoplasm by retrotranslocation, ubiquitinating them, and degrading them via the proteasome[160]. ERAD E3 RING finger ubiquitin ligases, which reside in the ER membrane and require cytoplasmic Zn^{2+} for their catalytic activity, are crucial components of this system[160]. There is little free Zn^{2+} in cells because most Zn^{2+} is bound to proteins[161]. Cytosolic concentration estimates range from 5-1,000 pM, which are orders of magnitude lower than free Ca^{2+}. Thus, an appealing possibility is that Catsup provides an essential, local source of Zn^{2+} at the ER/cytosol interface for ERAD E3 ubiquitin ligases. Consistent with this idea, overexpression of either of two ERAD E3 ubiquitin ligases, SORDD1/2, suppresses the proteotoxic effects of $Rh1^{G69D}$ expression in the *Drosophila* eye[162], just as Catsup overexpression reduced the levels of misfolded $Rh1^{G69D}$ protein expressed ectopically in border cells and alleviated all of the associated phenotypes including ER stress and border cell migration defects. This similarity between Catsup/ZIP7 and ERAD E3 ubiquitin ligase overexpression in rescuing $Rh1^{G69D}$ phenotypes supports the idea that they function in a common pathway.

The abnormal accumulation of Notch and EGFR in *Catsup* mutant border cells resembles the *Catsup* phenotype in *Drosophila* wing imaginal discs. Although Notch and EGFR regulate cell fate in imaginal disc cells and migration in border cells, our results support a common role for Catsup in both tissues. Using live cell labeling with an antibody against the extracellular domain, Groth et al[134] showed that normal levels of Notch receptor protein are present on the plasma membrane of *Catsup* mutant cells and are endocytosed normally, despite abnormal accumulation in the ER. This result is more consistent with the role we

propose for Catsup in ERAD than it is with the conclusion drawn by others that Catsup/ZIP7 affects Notch trafficking through the secretory pathway. An intriguing implication of the idea that Catsup/ZIP7 might provide a local source of $Zn^{2+}$for ERAD E3 ubiquitin ligases is that other Zn^{2+} transporters might also specialize in providing local Zn^{2+} for specific protein partners rather than, or in addition to, regulating global free Zn^{2+} within the cytosol or specific organelles, which is primarily how Zn^{2+} transport has been understood. Such a scenario could explain the need for 24 Zn^{2+} transporters in humans.

Our observations also raise the interesting question of why some proteins, like Notch and EGFR, are more prone to accumulation in the ER in *Catsup* mutant cells than others that also traverse the secretory pathway, such as E-cadherin. All of these are single-pass transmembrane proteins. Notch is a particularly large protein with 36 EGF-like repeats in and three cysteine-rich LIN12/Notch repeats in its extracellular domain, all of which require multiple disulfide bonds. Thus, Notch may be particularly prone to misfolding. By contrast, the EGFR extracellular domain is not as large or complex but, like Notch, it does contain two cysteine-rich domains and multiple disulfide bonds[163]. In addition to effects on ERAD, it is possible that Catsup/ZIP loss-of-function causes excess Zn^{2+} to accumulate in the ER, which could in principle interfere with protein folding in the ER lumen. For example, excess Zn^{2+} might interact with cysteine residues, disrupting proper disulfide bond formation [164]. In this case, *Catsup* mutant cells might be particularly prone to misfolding of newly synthesized proteins in the ER. Nolin et al. measured a rapid 2.5 fold increase in free Zn^{2+} in the ER lumen upon inhibition of ZIP7[157]. Whether such a modest increase of free Zn^{2+} in the ER lumen would be sufficient to interfere with protein folding is not known.

Our results show that ER stress impairs Notch signaling independent of aberrant protein accumulation because $Rh1^{G69D}$ inhibits Notch signaling without abnormal Notch or EGFR protein accumulation in the ER lumen. How ER stress or the UPR inhibit Notch signaling is not clear, but the observation that a pharmacological inhibitor of ZIP7 was identified as an inhibitor of Notch signaling by NICD in cultured U2OS cells[157] suggests that there is a deeply conserved requirement for Catsup/ZIP7 for Notch transcriptional activity. Nolin et al[157] showed that ZIP7 inhibition causes accumulation of full length Notch and a decrease in the NICD, and concluded that Notch activation by proteolysis was likely perturbed upon inhibition of ZIP7. An alternative interpretation is that full-length Notch accumulates in the ER lumen due to inhibition of ERAD, and that NICD is degraded more rapidly as part of the global ER stress response.

The ability of Catsup overexpression to alleviate the ER stress and cellular defects due to $Rh1^{G69D}$ expression has some general biomedical implications. Dominant mutations in rhodopsin that impair folding and cause accumulation in the ER cause retinal degeneration in human patients [165], for which there is no effective prevention or therapy. Over-expression of proteins that enhance ERAD may be a new therapeutic strategy to consider. Additionally, toxic protein aggregates have been proposed to kill neurons by inhibiting ERAD in numerous neurodegenerative diseases including Huntington's, Altzheimer's, Parkinson's, frontotemporal dementia, and others, even when the toxic protein is not localized in the ER[166]. Thus, strategies to enhance ERAD may be useful in treating these diseases as well.

The suppression of ER stress and border cell migration by Catsup overexpression is consistent with the observation that ZIP7 is over-expressed in numerous cancers where it promotes survival, proliferation and migration and correlates with disease progression,

invasion, and metastasis. The similarities in Catsup/ZIP7 functions and phenotypes across disparate cells, tissues, and organisms suggests that the border cell system offers an excellent model for deciphering the fundamental and conserved effects of this protein *in vivo.*

3.8. Materials and methods

Drosophila genetics

Catsup mutant fly was generated by ethyl methanesulfonate (EMS) mutagen[131]. The mutation results in glycine(G) to aspartic acid(D) replacement at amino acid 178. The FLP/FRT system was used to generate the Catsup^{G178D} homozygous mutant clones by combining FRT40A-Catsup^{G178D} with *hsFLP12,yw;ubi:GFPnls, FRT40A* or *hsFLP12,yw;ubi:RFPnls, FRT40A/(CyO)*. Catsup::GFP expression pattern visualized by the line from VDRC 318542 in the fTRG stocks library. The UAS-CatsupRNAi transgenic line is from VDRC 100095 *P{KK103630}VIE-260B.* Wild type rescue *w[*]; sna[Sco]/CyO; P{w[+mC]=UAS-Catsup.V5}6* Bloomington 63229. Additional transgenic Drosophila stocks used: UAS-wRNAi/Cyo is a lab stock, UAS-PleRNAi Bloomington 25796 *y[1] v[1]; P{y[+t7.7] v[+t1.8]=TRiP.JF01813}attP2,* UAS-Ple is Bloomington 37539 *w[*]; P{w[+mC]=UAS-ple.T}331f2*, O-fucosyltransferase1 Bloomington 9376 *P{UAS-O-fut1.O}11.1*, UAS-Notch.Intracellular.Domain on third chromosome was a gift from Artavanis-Tsakonas lab[167]. The ER stress marker UAS-Xbp1-EGFP.HG Bloomington 60731 *w[*]; P{w[+mC]=UAS-Xbp1.EGFP.HG}3,* UAS-HSC70-3 Bloomington 5843 *w[126]; P{w[+mC]=UAS-Hsc70-3.WT}B.* Catsup point mutations were cloned into vector pUASt-attb with forward primer ctctgaatagggaattgggATGGCCAAACAAGTGGCTGA and

reverse primer ccgcagatctgttaacgtcaCGTAGAATCGAGACCGAGGAGAG. The vector was injected to attp2 flies *y1 w67c23; P{CaryP}attP2* by BestGene Inc.

Design of UAS-RNAi-resistant Catsup point mutations

When generating UAS-Catsup-point-mutations, we designed the construct so it cannot be targeted by the CatsupRNAi sequences by substituting redundant codons for the same amino acids within the region targeted by the RNAi. The RNAi resistant sequence is below with nucleic acid substitutions in lower case:

ACAcGGcCAttcCCAtGAcATGtcCATcGGctTGTGGGTgCTgGGcGGcATtATcGCgTTtCT
gagcGTcGAaAAgtTGGTgCGtATcCTgAAaGGaGGcCAcGGcGGcCAtGGaCAttcCCAcGG
cGCcCCcAAaCCcAAgCCcGTcCCcGCcAAaAAgAAaagCagcGAtAAgGAgGAttcCGGcG
AcGGcGAtAAgCCcGCcAAaCCcGCgAAaATtAAaagCAAaAAgCCcGAgGCcGAaCCcGA
gGGaGAgGTcGAaATcagCGGaTAtcTGAAccTGGCcGCcGAtTTcGCcCAtAAtTTtACgGA
cGGatTGGCgATtGGaGCgagCTAccTGGCcGGaAAttcCATcGGaATcGTcACgACcATtAC
cATctTGtTGCAtGAgGTcCCgCAcGAaATcGGcGAtTTcGCgATcCTgATcAAaagcGGaTG
cagCcGcCGcAAaGCcATGCTgtTGCAaCTgGTgACcGCcCTgGGcGCccTGGCcGGaACcG
CcCTgGCcCTgtTGGGcGCcGGcGGaGGcGAtGGcagcGCgCCcTGGGTgcTGCCgTTtACc
GCgGGaGGcTTcATcTAtATtGCcACcGTcAGcGTgtTGCCcGAatTGCTgGAaGAaagcACc
AAgtTGAAgCAaagctTGAAaGAgATtTTcGCctTGCTgACCGGCGTAGCCCTAATGATC
GTTATCGCCAAGTTCGAGGg.

Point mutations were designed by changing codons at the following site CatsupH183A (CAC to GCC), CatsupH187A (CAT to GCT), CatsupH315A (CAT to GCT), CatsupH344A (GCT to CAT).

Immunostaining and confocal imaging

Female flies were fattened with yeast for 2 days at 29°C. Egg chambers were dissected from ovaries of female flies in Schneider's medium with 10% FBS (pH=6.85-6.95) as described previously[168]. Freshly dissected egg chambers were fixed in 4% paraformaldehyde and then incubated overnight in 1xPBS with 0.4% triton and the following primary antibodies: mouse anti-PDI (1:200) (ADI-SPA-891-D Enzo Life Sciences, Inc.), chicken anti-GFP (1:200) (ab13970 Abcam plc.), Ple (anti-TH) antibody (a gift from the Craig Montell lab), mouse anti-Notch intracellular domain (1:100) C17.9C6 DSHB, rat Ecadherin antibody DCAD2 (1:50) DSHB, V5 Tag Monoclonal Antibody-Alexa Fluor 555 (2F11F7) Invitrogen, mouse anti-dEGFR (1:2000) E2906 Sigma Aldrich. O-fut1 antibody was used to confirm O-fut1 overexpression, and was a gift from Kenneth D. Irvine lab [169]. Secondary antibodies were incubated for 2 hours, together with Hoechst stain for nuclei, and phalloidin stain for F-actin. Mouse anti-PDI and mouse anti-V5-555 co-staining was done by first staining with PDI primary and secondary, followed by a thorough washout, and application of anti-V5-555 overnight. Immunostained samples were mounted in VECTASHIELD mounting medium from Vector Laboratories. Zeiss LSM780 and LSM800 confocal microscopes were used to acquire images. Images were processed using FIJI, rotated and cropped for presentation.

Sequence alignment

Catsup and ZIP7 amino acid sequences were acquired from NCBI in a FASTA format. The files were input into T-coffee http://tcoffee.crg.cat/apps/tcoffee/do:regular to generate multiple sequence alignment. The output was fed into Boxshade

http://www.ch.embnet.org/software/BOX_form.html to generate the sequence alignment with black and grey shades to show the conserved sequence region.

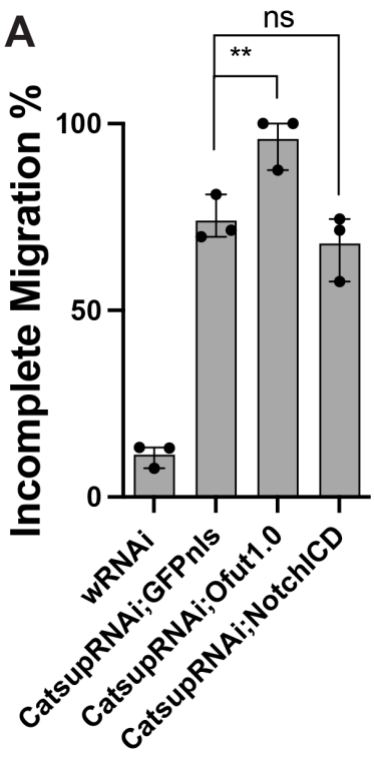

Supplemental Fig 3.1. Ofut1.0 and Notch intracellular domain do not fully rescue CatsupRNAi

(A) The quantification of incomplete migration rates in C306Gal4 driving wRNAi (control), CatsupRNAi;GFPnls caused over 80% incomplete migration, which is not significantly rescued by Ofut1.0 nor by Notch intracellular domain over expression.

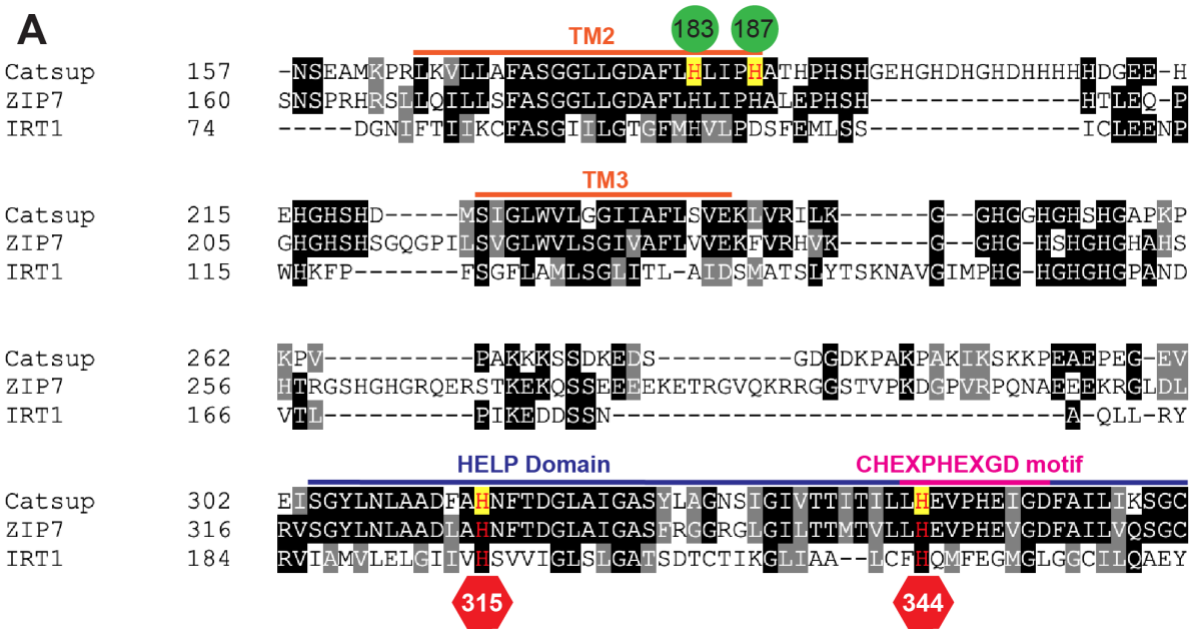

Supplemental Fig 3.2. Sequence alignment of Catsup, ZIP7, and the arabidopsis protein IRT1.

(A) Identical amino acids are shaded in black, similar amino acids in gray. Amino acid substitutions generated in this study are highlighted in yellow with red text. Green circles show the mutations that rescue CatsupRNAi caused migration defects, and red hexagons are the mutations that do not.

4. A new Tropomyosin1 isoform supports Drosophila border cell migration

Four types of filamentous networks make up the cytoskeleton of a eukaryotic cell: F-actin, microtubules, intermediate filaments, and septins, all of which contribute to cell migration behaviours in different ways [170–173]. Cytoplasmic intermediate filament proteins were

unknown in Drosophila until an atypical tropomyosin was reported to polymerize into filaments that are intermediate in diameter between F-actin microfilaments and microtubules [174]. Whereas canonical tropomyosins form end-to-end coiled-coils that wind around and stabilize actin filaments, Cho et al. found that atypical isoforms of fly Tropomyosin 1 (Tm1-I and -C) possess a central coiled-coil domain shared with canonical Tm1 that is flanked with intrinsically disordered N- and C-terminal domains. This domain architecture resembles intermediate filament protein subunits rather than classical tropomyosins. RNAi targeting of an exon present in Tm1-I/C but lacking in canonical Tm1 isoforms results in incomplete border cell migration and female infertility (Fig13. A, B).

4.1. Tm1-I/C is dispensable for border cell migration

To study the mechanism of Tm1-I/C function in border cell migration, we used CRISPR-Cas9 to knock out Tm1-I/C by adding two stop codons after the putative start codon (Fig. 13B). We confirmed the gene editing by DNA sequencing (see methods). Interestingly, the knocked out flies (Tm1-I/C-KO) were fertile, indicating that border cells migrated normally. Instead, these flies exhibited a grandchildless phenotype, consistent with findings by two other groups [175–177]: Tm1-I/C homozygous mutant females fail to form germ plasm during oogenesis, so their progeny are viable but sterile.

4.2. Tm1-X is sufficient to rescue border cell migration

If Tm1-I/C is not required for border cell migration, why does Tm1-I/C-RNAi inhibit migration? One possibility would be that the RNAi causes an off-target effect. However, we found that expression of UAS-Tm1-I/C/X-RNAi in border cells and posterior follicle cells using the c306Gal4 driver, effectively knocked down an N-terminally tagged version of Tm1-I/C [177] (Fig. 13C-D). The Tm1 locus is extensively alternatively spliced, producing at least 18 distinct isoforms (Fig.13A). We suspected that the RNAi might target an additional, unidentified isoform that is essential for border cell migration. The RNAi sequence targets an exon predicted to be present in multiple isoforms including Tm1-I/C/H/E, however Tm1-H and Tm1-E are not detectable in Drosophila ovaries [174]. The same exon, however, has additional downstream ATGs in frame with Tm1-I/C, which could be translated into a shorter polypeptide. We named this putative isoform Tm1-X (Fig. 13B). We made transgenic flies that express Tm1-X under UAS regulatory sequences to test whether Tm1-X would be sufficient to rescue the border cell migration defect caused by the RNAi. To visualize the protein, we included an mCherry fused to the Tm1-X N terminus. One copy of Tm1-X partially rescued border cell migration(Fig. 13E, G), and two copies of UAS-Tm1-X rescued nearly completely (Fig.13F, G). Combining UAS-Tm1-I/C and UAS-Tm1-X together was only 10% more effective than a single copy of UAS-Tm1-X (Fig. 13G). We conclude that Tm1-X expression is sufficient to support border cell migration.

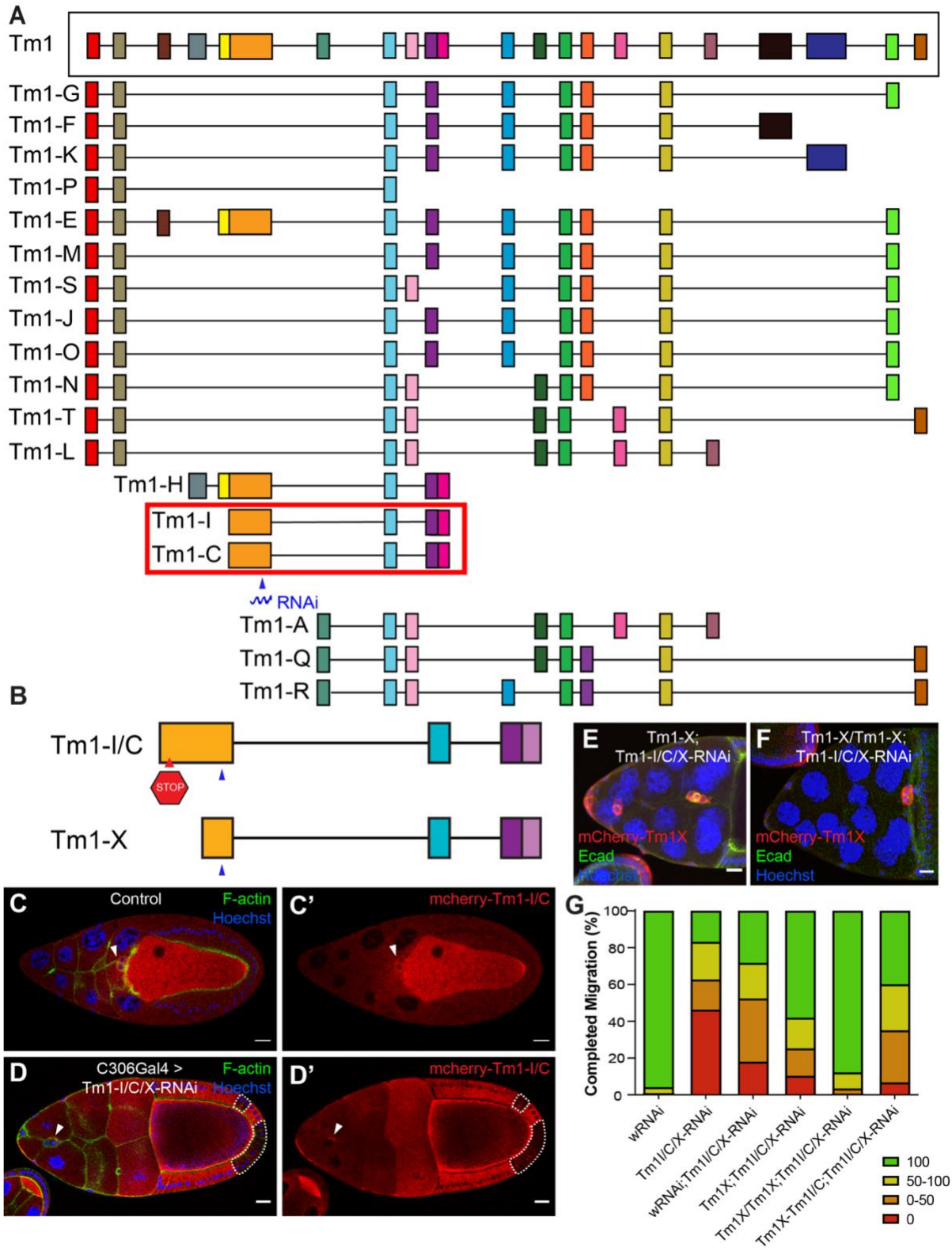

Fig. 13. A new Tropomyosin1 isoform, Tm1-X supports border cell migration

(A) Schematic representation of the 18 known Tropomyosin1 predicted transcripts, adapted from www.flybase.org. Exons are color coded. (B) Schematic representation of the Tm1-I/C transcript (upper panel). Red arrowhead indicates the stop codon insertion sites for generation of the Tm1-I/C-KO. The position of the Tm1-I/C-RNAi sequence is indicated in blue. The predicted Tm1-X isoform is fully contained within the Tm1-I/C (lower panel). (C) mCherry-tagged Tm1-I/C (red) is expressed in every cell in the egg chamber, (D) c306Gal4-driven RNAi knocks down the Tm1-I/C in border cells (white arrowhead) and posterior epithelial cells (dotted lines). Phalloidin stains F-actin in green and Hoechst stains DNA in blue. (E-F) Phenotypes of c304Gal4 driving one (E) or two copies (F) of UAS-mCherry-Tm1X with UAS-Tm1I/C/XRNAi in border cells. mCherry-Tm1X in red, E-cadherin in green, and Hoechst in blue. (G) Quantification of completed migration at stage 10 for c306Gal4 driving the indicated UAS constructs. The distance migrated as a percentage of the total path is color-coded so that 0%, 1-50%, 51-99% and 100% is represented in red, orange, yellow and green respectively. Scale bar: 20 um.

4.3. Tm1-X is a cytoplasmic, non-canonical Tropomyosin

Tm1-A and Tm1-L are canonical tropomyosins in Drosophila, which colocalize with F-actin at the cell cortex, whereas the non-canonical Tm1-I/C isoforms, which form intermediate filament-like structures in vitro, are diffuse throughout the cytoplasm [174]. When using antibodies that recognize all Tm1 isoforms (anti-Pan-Tm1), cytoplasmic staining is detected (Fig. 14A, A'). Tm1-I/C-KO flies retain cytoplasmically localized Tm1 (Fig. 14B, B'). The remaining cytoplasmic signal could be due to Tm1-X, consistent with the work of Gaspar et

al [177]. They also made a Tm1-I/C mutant (named $Tm1^{eg9}$), which lacks perinuclear staining in the nurse cells; however, the mutant egg chambers still have cytoplasmic Tm1. Additionally, a protein of the size predicted for Tm1-X (29.4 kD) was detected in a western blot by Veeranan-Karmegam et al. when they used an anti Tm1-I/C antibody to probe ovary lysates from the Tm1-I/C null mutant [176].

We carried out quantitative polymerase chain reaction (q-PCR) to determine if we could detect Tm1-X mRNA in wild-type and TM1-I/C mutant ovaries. Since Tm1-X is completely contained within Tm1-I/C, it is not possible to uniquely amplify TM1-X sequences from wild type. However it is possible to amplify sequences unique to Tm1-I/C (Fig. 14C). As expected, we were able to detect mRNA from wild type ovaries using primers that bind either to Tm1-I/C or to Tm1I/C and X transcripts. Furthermore, a low level of product was detected using primers targeting the Tm1-X region from mRNA isolated from the Tm1-I/C-KO flies whereas no product was amplified using Tm1-I/C-specific primers on the TM1-I/C mutant mRNA (Fig. 14C). These results are consistent with the interpretation that Tm1-X is expressed in both wild type and Tm1-I/C mutants. However, we note two anomalies that we cannot currently explain. First, the Tm1I/C/X primers should amplify mRNA from all three transcripts and thus should yield quantitatively more product than the Tm1-I/C primers. Yet we detected fewer rather than more transcripts. Secondly, the level of transcripts amplified by the Tm1-I/C/X primers from the Tm1-I/C mutants is ten-fold reduced compared to wild type. This is not consistent with the level of residual antibody staining or the level of the 26kD protein Veeranan-Karmegam et al. detected by Western blot or the level of expression of Tm1-X required to rescue the RNAi phenotype. Therefore we conclude that the Tm1-X

primers may not have been working efficiently in this experiment. Further experiments will be required to clarify this point.

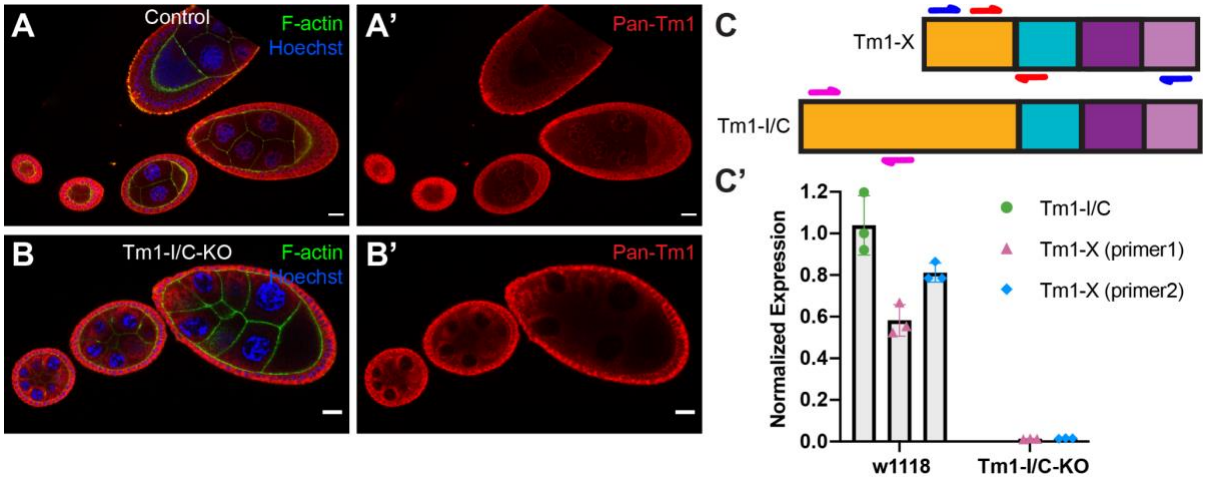

Fig. 14. Tropomyosin1-X is localized in the cytoplasm

(A-A') w1118 control and (B-B') Tm1-I/C-KO egg chambers are stained with Pan-Tm1 (red), F-actin in green and hoechst in blue. (A', B') Single channel view of the Pan-Tm1 staining. (C) Designed primers are indicated in red (Tm1-X primer set 1), blue (Tm1-X Primer set 2) and magenta (Tm1-I/C). (C') q-PCR detects expression of Tm1-I/C (green circle) and Tm1-X (pink triangle for primer set 1 and blue diamond for primer set 2) in w1118 and Tm1-I/C-KO flies. The expression is normalized to tubulin expression level in each sample and each data point is further normalized to the mean of w1118 Tm1-I/C. Egg chamber scale bar: 20 um.

Tm1-I/C isoforms assemble into intermediate filament-like structures in vitro. Compared to Tm1-I/C, Tm1-X has a shorter N-terminal, intrinsically disordered, head domain but the same coiled-coil and C-terminal disordered tail domains. To test whether Tm1-X forms filaments, we collaborated with Vasily Sysoev in Masato Kato's lab at the University of

Texas Southwestern Medical Center. They expressed and purified the full length Tm1-X, Tm1-X lacking the N-terminal disordered domain (headless), and Tm1-X lacking the C-terminal tail domain (tailless). As a positive control, Tm1-I/C formed filaments following an overnight incubation in vitro (Fig. 15A). Tm1-X formed aggregates and occasional long fibrils (Fig. 15B), but developed into filaments that resemble Tm1-I/C after 3 days of incubation (Fig. 15B'). Headless Tm1-X was able to form filaments (Fig. 15C, C') while Tailless Tm1-X did not (Fig. 15D) We conclude that Tm1-X may form different structures in vivo than Tm1-I/C, which could in principle explain its distinctive ability to support border cell migration. One possibility is that Tm1-I/C produces longer and more stable filaments whereas Tm1-X produces a more dynamic filament network that is required for cells to be able to change shape and move through the confined spaces within the egg chamber.

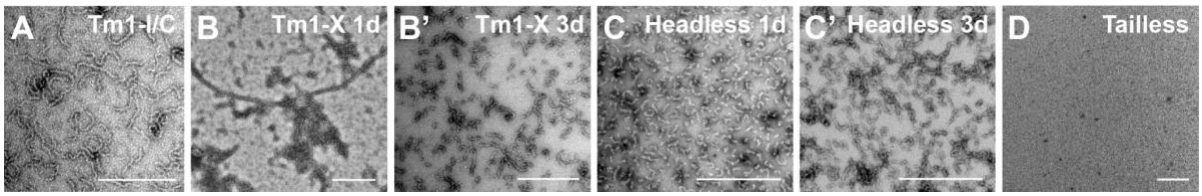

Fig. 15. Tropomyosin1-X forms filaments *in vitro*

(A) Purified Tm1-I/C protein (residues 2-441) forms intermediate filaments. (B) The overnight sample of Tm1-X (residues 184-441, in Tm1-I/C numeration) aggregates and forms long fibrils. (B') After three day incubation at room temperature that same Tm1-X sample contained filaments that resembled Tm1-I/C filaments. (C-C') Headless Tm1 protein (residues 204-441) forms filaments always. (D) Tailless protein (residues 2-372) cannot form any filaments. Egg chamber scale bar, 20um. Filaments scale bar, 500 nm.

4.4. Methods and materials

Fly Genetics and antibodies

Mcherry-Tm1-I/Tm3,ser #D (Fig. 13C, D) is generously given by Anne Ephrussi's lab. Tm1-I/C/X-RNAi is from the VDRC stock center: V34119. Overexpression of Tm1-I/C was done by the transgenic line UAS-EGFP-Tm1-I/C that was published by our lab [174]. Pan-Tm1 antibody was generated by Cho et al. as well.

Tm1-I/C CRISPR knock out

Two stop codons were inserted after the start codon of Tm1-I/C. The insertion is designed by protocols on (https://flycrispr.org/scarless-gene-editing/). 1kb left homology arm and 1kb right homology arm are cloned into the pHD-ScarlessDsRed vector. gRNAs were designed to target GGGAACTAGACTGGTATTGCTGG. The constructs with designed gRNAs are injected into Cas9 expressing flies and edited progenies are screened by DsRed expression. Unexpectedly, the edition did not take place in the designed way, but still served the same purpose. We sequenced the effectively edited progeny and confirmed that two stop codons (underlined) were inserted: ATG GAG CAC GAT GAC TCC AGC ACC AGT GGC ACT TGA GGC TAA.

Transgenic fly UAST-mCherry-Tm1-X generation

Tm1-X was designed to be RNAi resistant and synthesized by Integrated DNA Technologies (https://www.idtdna.com). The Tm1-X RNAi resistant sequence is fused with mCherry

sequence at the N-terminus and together cloned into a pUAST vector. The construct is injected into the stock attp40 fly embryos by the Bestgene company.

q-PCR for Tm1-X isoform

Total RNA was extracted from the w1118 and Tm1-I/C-KO fly lysates by Qiagen RNeasy kit. RNA was treated by Turbo DNA Free kit to digest reminiscent DNA. DNA-free RNA extract was used to synthesize cDNA. q-PCR was run at BioRad Thermal Cycler using the BioRad CFX Manager3.1 application. Tubulin was used as a positive target, and the expression is normalized to the average of tubulin expression level. Two primer sets were used to detect Tm1-X expression in Tm1-I/C-KO flies. Primer forward 1: CATCTTCAGTTCGGACACCA; reverse 1: CAGAGCGCTCCAAGTCTTCT. Primer forward 2: AAGGGACGTTGTGCGGATTA; reverse 2: CAGAGCGCTCCAAGTCTTCT.

Tm1 protein filaments formation

Tm1-I/C, Tm1-X, Headless Tm1-X and Tailless Tm1-X were expressed in bacteria and purified under denaturing conditions. The purified proteins were diluted to 100 uM and dialyzed against 50 mM MES-Na, pH 6.25, 170 mM NaCl, 10 mM beta-mercaptoethanol. Samples were incubated at room temperature for overnight or 3 days.

5. Perspectives and future directions

I have presented three studies that shed new light on the mechanisms that regulate collective cell migration in vivo both within migrating cells and in the external microenvironment. Each

study answered one or more questions, but also revealed directions for future study. Here, I present and discuss some of these exciting research avenues.

5.1. How does nuclear stiffness contribute to migration through a confined, cell-rich environment?

Reconstructing entire egg chambers in three dimensions provided a comprehensive view of the microenvironment that border cells encounter (Chapter 2). Of all the features that could in principle affect border cell path selection, the configuration of nurse cells turned out to be the most consequential. Junctures of three or more nurse cells are concentrated in the center of the egg chamber where they create a more favorable environment for protrusion compared to the interfaces of two nurse cells due to availability of tiny spaces even though they are much smaller than the cells that move into them. This is because border cells extend slender protrusions that are closer in size to the spaces they enter. Protrusion between two nurse cells requires breaking nurse cell-nurse cell adhesions whereas junctures of three or more cells leave tiny open spaces, reducing the energy barrier for protrusion, even though the crevices are much smaller than the border cell cluster or even a single cell or even a single nucleus. By measuring multiple features of the microenvironment, our work revealed that chemoattractants promote posterior migration whereas tissue topography favors the central path; E-cadherin-mediated adhesion provides traction in addition to its earlier reported role in amplifying the difference in chemoattractant signaling between the front and back of the cluster [93].

The work also offers an explanation for an earlier, unexplained phenomenon. The small GTPase Rac functions downstream of chemoattractant signaling [86,107], and Wang et al.

showed that photoactivation of an optogenetic form of Rac (PA-Rac) within a single border cell caused local protrusion and was sufficient to shift the direction of migration for the entire cluster [99]. Intriguingly, PA-Rac readily steered the cluster forward and backward along the medial migration path but it was not possible to steer the cells into side paths. At the time it was unclear what feature of the microenvironment was causing cells to favor the central path. Our results indicate that the central path is where multiple-nurse-cell junctures are concentrated, creating a path of least resistance.

The fact that the limited space between nurse cells is not even the size of a single cell nucleus is intriguing, since the nucleus is typically the largest and stiffest organelle, which impedes cell movement through a confined space in vitro [96]. Studies investigating single cancer cells or immune cells migrating between plastic pillars within microdevices or through dense ECM have concluded that nuclear stiffness impedes cell migration. A-type lamins form an intermediate filament meshwork underneath the nuclear envelope, and are major contributors to nuclear stiffness and structural integrity. A-type Lamin levels thereby impede cell migration while actomyosin-derived forces push and pull on nuclei to squeeze them through small spaces. In contrast, work in more deformable hydrogels has found that Lamin A/C can promote migration in some circumstances. In vivo, when single and collectively migrating cancer cells metastasize from solid tumors, they move through extracellular matrix (ECM), invade basement membranes, and squeeze between other cells during intravasation and extravasation. The microenvironment of the migration is often compact and confined. How the nucleus responds to the environment and whether it impedes or promotes cell migration generally, and border cell migration in particular, is still unknown. Thus, an important future

direction will be to investigate how Drosophila border cell nuclear structure and mechanics promote or impede their movement and how this relates to tumor metastasis.

To investigate the role of nuclear mechanics in border cell migration, we could knock down genes encoding key nuclear envelope proteins to change nuclear rigidity in the border cells and measure the effects on migration. Preliminary data show that type B lamin contributes to border cell migration. B type lamins polymerize into a separate intermediate filament network from A type lamins. In addition to providing structural support, lamin networks are involved in organization of the nuclear envelope, regulation of gene expression, and nuclear positioning. It would be interesting to figure out which of the roles Lamin B is playing in assisting cell migration. Emerging work shows a connection between mechanics and gene expression changes, it would be exciting to learn whether in addition to transcriptional changes, nuclear mechanics also affect cell migration.

5.2. From border cell migration to a gene therapy for Retinitis Pigmentosa?

Through genomic screening, we found that the multi-functional protein Catsup plays an important role in border cell migration. We propose that Catsup provides a local source of Zn^{2+} to RING finger ubiquitin ligases that are required to degrade misfolded proteins by ERAD. Thus, the Zn^{2+} transporter Catsup promotes ERAD, mitigates ER stress and, supports border cell migration and epithelial cell survival (see Chapters 1 and 3).

Strikingly, Catsup overexpression was sufficient to eliminate the accumulation of misfolded $Rh1^{G69D}$ protein, probably by enhancing ERAD, which then resolved the ER stress and rescued

border cell migration. ERAD depends on the ubiquitin E3 ligases that have RING finger domains, which must bind to Zn^{2+} ions to function properly. In Drosophila, the ligases are SORDD1/2 and are located on the ER membrane. To confirm that it is the enhanced ERAD that promotes misfolded protein degradation and thus resolved ER stress, we could investigate whether overexpression of SORDD1/2 rescues misfolded protein accumulation and the border cell migration defects caused by CatsupRNAi or expression of $Rh1^{G69D}$.

Catsup is one of many ZIP family Zn^{2+} transporters that transport Zinc ions from outside the cell or within organelles into the cytosol. To distinguish whether it is the global cytosolic Zn^{2+} concentration or the local Zn^{2+} in the immediate vicinity of the RING finger E3 ligases that matters for ERAD and ER homeostasis, we could overexpress each of the ZIP transporters and test for rescue of $Rh1^{G69D}$ protein accumulation or CatsupRNAi.

Our results indicate that some proteins are more prone to misfolding than others. For example, Notch and EGFR accumulate in the ER whereas neither E-cadherin nor N-cadherin accumulates in Catsup RNAi-expressing cells, despite the fact that they are all single pass transmembrane proteins (see Chapter 3). To ascertain which proteins are prone to misfolding and which are not, we could stain Catsup RNAi-expressing cells with antibodies against numerous different proteins that are normally present in the ER lumen as well as multi-pass transmembrane proteins.

It has long been known that Notch protein accumulates abnormally in the ER of Catsup mutant cells in Drosophila wing imaginal discs and when ZIP7 is inhibited in human cancer cells. In addition, Notch signaling is inhibited. Prior studies attempted to explain both findings by concluding that Notch trafficking to the plasma membrane was impaired.

However, surface labeling of Notch protein in living cells found a normal amount of Notch at the surface and no change in the rate of endocytosis, leaving a puzzle as to why Notch signaling was impaired. Our studies suggest an explanation for this conundrum. We propose that the defect in Notch signaling is a secondary consequence of the ER stress response that is activated in Catsup mutant cells as a result of the ERAD defect. Consistent with this model, Notch signaling is also perturbed by $Rh1^{G69D}$ expression, which causes ER stress. A further prediction of our model is that Catsup overexpression will rescue that defect.

A number of human diseases are linked to abnormal protein accumulation and ER stress. For example, the most common cause of Retinitis Pigmentosa are dominant mutations in human rhodopsin which lead to its accumulation in the ER. Over many years this eventually causes photoreceptor cell death and thus results in blindness. A cure or, better yet, a technique to prevent cell death and blindness, is an obvious goal. The ability of Catsup overexpression to restore protein homeostasis and biological functions such as border cell migration suggests a strategy. In preliminary experiments, my colleague Morgan Mutch has found that Catsup overexpression also rescues cell death caused by expression of $Rh1^{G69D}$ in Drosophila photoreceptor cells. Future experiments will test whether overexpression of the human homolog ZIP7 rescues photoreceptor defects due to mutant Rh1 in retinal organoid cultures derived from patient iPS cells.

Of potentially even greater impact, there are many neuronal degenerative diseases that are caused by over accumulation of misfolded cytoplasmic proteins, such as Tau protein, HTT, b-amyloid, a-synuclein, and others. It would be interesting to know whether Catsup and/or ZIP7 overexpression can rescue defects caused by misfolded cytosolic proteins, which are known to indirectly impair ERAD and cause ER stress. We could first test this hypothesis in

Drosophila models of neurodegenerative disease before moving to more complex mammalian models. ER stress and its regulators are evolutionarily ancient and the mechanisms are likely conserved.

ZIP7 is upregulated in many cancer types to promote cell survival and migration, and Catsup mutant also leads to epithelial cell death in drosophila. In our proposed model, Catsup is likely enhancing the function of E3 ubiquitin ligases by supplying local Zn^{2+}. E3 ligases are known to tag P53 and keep its level low when not needed. Whether CatsupRNAi or ZIP7 inhibition caused cell death is P53 dependent or not is still not known, and can be tested in Drosophila epithelial cells and in human cancer cell lines. Furthermore, anastasis is the process by which cells recover from the brink of apoptotic cell death following severe but transient stress. Whether Catsup/ZIP7 overexpression or inhibition affects anastasis remains to be determined.

5.3. Intermediate filament proteins in Drosophila?

As presented in Chapter 4, we identified a new isoform of Tropomyosin-1: Tm1-X, which is a shorter version of Tm1-I/C, which is essential for border cell migration. Similar to Tm1-I/C, Tm1-X is also cytoplasmically distributed and can form filaments in vitro. However, Tm1-X has a shorter N-terminal disordered domain and distinct filament-forming properties in vitro. It would be interesting to determine if the altered filament forming properties are critical for the function of Tm1-X in border cell migration.

Whether Tm1-X forms intermediate filaments structure similar to Tm1-I/C in vivo is not known. Compared to canonical tropomyosins Tm1-A/L that are colocalized with and stabilize F-actin, intermediate filaments should be localized in cytoplasm. There is no specific antibody that could detect Tm1-X isoform, however, Pan-Tm1 antibody shows a cytoplasm signal in the Tm1-I/C-KO egg chamber in ours and others research. The still existing cytoplasmic Tm1 could be due to Tm1-X. This could further be confirmed by Tm1-X-KO flies that were made by CRISPR-Cas9 gene editing, if Tm1-X-KO cells lose the cytoplasmic Tm1. Intermediate filaments functionally bind with microtubules and stabilize them. To test whether Tm1-X forms intermediate filaments in vivo, we could stain for microtubules and together with Pan-Tm1, then check whether filamentous structures can be visualized.

Using qPCR to detect the Tm1-X transcript has generated inconclusive data that could be due to primer quality or other technical issues, which are resolvable. In the meanwhile, we also conducted Rapid Amplification of cDNA Ends (RACE) to the w1118 control flies in an attempt to detect the presence of specific Tm1 transcripts. Only the Tm1-I/C transcripts ends were amplified and an expected shorter 5' RACE (corresponding to Tm1-X) was not detected. This result suggests two possibilities. First, in wild type controls, instead of an alternative spliced mRNA transcript, Tm1-X protein could be alternatively translated from the existing Tm1-I/C isoform. Second, Tm1-X transcript might not exist in wild type, only when Tm1-I/C is knocked out, Tm1-X might be transcribed to complement the loss of the Tm1-I/C. However, the fact that Tm1-I/C was not able to rescue migration defects as well as Tm1-X and that two copies of Tm1-X are needed to rescue the defect indicate that Tm1-X

exists at an abundant level naturally. It would be informative to test whether Tm1-X cDNA ends can be detected in the Tm1-I/C-KO flies either way.

While the work presented in this thesis advances our understanding of cell migration, there are many intriguing questions remaining. In science, every answer leads to at least one new question, and these three projects are no exception.

Bibliography

1. Van Haastert, P.J.M., and Devreotes, P.N. (2004). Chemotaxis: signalling the way forward. Nat. Rev. Mol. Cell Biol. *5*, 626–634.
2. Lauffenburger, D.A., and Horwitz, A.F. (1996). Cell migration: a physically integrated molecular process. Cell *84*, 359–369.
3. Miskolci, V., Klemm, L.C., and Huttenlocher, A. (2020). Cell Migration Guided by Cell-Cell Contacts in Innate Immunity. Trends Cell Biol.
5. Grimaldi, C., and Raz, E. (2020). Germ cell migration-Evolutionary issues and current understanding. Semin. Cell Dev. Biol. *100*, 152–159.
6. Martinez-Garay, I. (2020). Molecular mechanisms of cadherin function during cortical migration. Front. Cell Dev. Biol. *8*, 588152.
7. Friedl, P., and Gilmour, D. (2009). Collective cell migration in morphogenesis, regeneration and cancer. Nat. Rev. Mol. Cell Biol. *10*, 445–457.
8. Unable to find information for 1209190.
9. SenGupta, S., Parent, C.A., and Bear, J.E. (2021). The principles of directed cell migration. Nat. Rev. Mol. Cell Biol. *22*, 529–547.
10. Mishra, A.K., Campanale, J.P., Mondo, J.A., and Montell, D.J. (2019). Cell interactions in collective cell migration. Development *146*.
11. Barriga, E.H., Franze, K., Charras, G., and Mayor, R. (2018). Tissue stiffening coordinates morphogenesis by triggering collective cell migration in vivo. Nature *554*, 523–527.
12. Dai, W., Guo, X., Cao, Y., Mondo, J.A., Campanale, J.P., Montell, B.J., Burrous, H.,

Streichan, S., Gov, N., Rappel, W.-J., *et al.* (2020). Tissue topography steers migrating Drosophila border cells. Science *370*, 987–990.

13. Richardson, B.E., and Lehmann, R. (2010). Mechanisms guiding primordial germ cell migration: strategies from different organisms. Nat. Rev. Mol. Cell Biol. *11*, 37–49.

14. Rahimi-Balaei, M., Bergen, H., Kong, J., and Marzban, H. (2018). Neuronal migration during development of the cerebellum. Front. Cell. Neurosci. *12*, 484.

15. Anton, E.S., Kreidberg, J.A., and Rakic, P. (1999). Distinct functions of alpha3 and alpha(v) integrin receptors in neuronal migration and laminar organization of the cerebral cortex. Neuron *22*, 277–289.

16. Elias, L.A.B., Wang, D.D., and Kriegstein, A.R. (2007). Gap junction adhesion is necessary for radial migration in the neocortex. Nature *448*, 901–907.

17. Horn, Z., Behesti, H., and Hatten, M.E. (2018). N-cadherin provides a cis and trans ligand for astrotactin that functions in glial-guided neuronal migration. Proc Natl Acad Sci USA *115*, 10556–10563.

18. Gil-Sanz, C., Franco, S.J., Martinez-Garay, I., Espinosa, A., Harkins-Perry, S., and Müller, U. (2013). Cajal-Retzius cells instruct neuronal migration by coincidence signaling between secreted and contact-dependent guidance cues. Neuron *79*, 461–477.

19. Prockop, S.E., Palencia, S., Ryan, C.M., Gordon, K., Gray, D., and Petrie, H.T. (2002). Stromal cells provide the matrix for migration of early lymphoid progenitors through the thymic cortex. J. Immunol. *169*, 4354–4361.

20. Harman, B.C., Jenkinson, E.J., and Anderson, G. (2003). Microenvironmental regulation of Notch signalling in T cell development. Seminars in immunology *15*, 91–97.

21. McCaughtry, T.M., Wilken, M.S., and Hogquist, K.A. (2007). Thymic emigration revisited. J. Exp. Med. *204*, 2513–2520.

22. Gallegos, A.M., and Bevan, M.J. (2004). Central tolerance to tissue-specific antigens mediated by direct and indirect antigen presentation. J. Exp. Med. *200*, 1039–1049.

23. Le Borgne, M., Ladi, E., Dzhagalov, I., Herzmark, P., Liao, Y.F., Chakraborty, A.K., and Robey, E.A. (2009). The impact of negative selection on thymocyte migration in the medulla. Nat. Immunol. *10*, 823–830.

24. Bajoghli, B., Kuri, P., Inoue, D., Aghaallaei, N., Hanelt, M., Thumberger, T., Rauzi, M., Wittbrodt, J., and Leptin, M. (2015). Noninvasive in toto imaging of the thymus reveals heterogeneous migratory behavior of developing T cells. J. Immunol. *195*, 2177–2186.

25. Filippi, M.-D. (2019). Neutrophil transendothelial migration: updates and new

perspectives. Blood *133*, 2149–2158.

26. Kroon, J., Daniel, A.E., Hoogenboezem, M., and van Buul, J.D. (2014). Real-time imaging of endothelial cell-cell junctions during neutrophil transmigration under physiological flow. J. Vis. Exp., e51766.

27. Muller, W.A. (2016). Transendothelial migration: unifying principles from the endothelial perspective. Immunol. Rev. *273*, 61–75.

28. Proebstl, D., Voisin, M.-B., Woodfin, A., Whiteford, J., D'Acquisto, F., Jones, G.E., Rowe, D., and Nourshargh, S. (2012). Pericytes support neutrophil subendothelial cell crawling and breaching of venular walls in vivo. J. Exp. Med. *209*, 1219–1234.

29. Kurz, A.R.M., Pruenster, M., Rohwedder, I., Ramadass, M., Schäfer, K., Harrison, U., Gouveia, G., Nussbaum, C., Immler, R., Wiessner, J.R., *et al.* (2016). MST1-dependent vesicle trafficking regulates neutrophil transmigration through the vascular basement membrane. The Journal of Clinical Investigation.

30. Liesveld, J.L., Sharma, N., and Aljitawi, O.S. (2020). Stem cell homing: From physiology to therapeutics. Stem Cells *38*, 1241–1253.

31. Unable to find information for 676249.

32. Li, D., Xue, W., Li, M., Dong, M., Wang, J., Wang, X., Li, X., Chen, K., Zhang, W., Wu, S., *et al.* (2018). VCAM-1+ macrophages guide the homing of HSPCs to a vascular niche. Nature *564*, 119–124.

33. Kitano, M., Yamazaki, C., Takumi, A., Ikeno, T., Hemmi, H., Takahashi, N., Shimizu, K., Fraser, S.E., Hoshino, K., Kaisho, T., *et al.* (2016). Imaging of the cross-presenting dendritic cell subsets in the skin-draining lymph node. Proc Natl Acad Sci USA *113*, 1044–1049.

34. Uderhardt, S., Martins, A.J., Tsang, J.S., Lämmermann, T., and Germain, R.N. (2019). Resident Macrophages Cloak Tissue Microlesions to Prevent Neutrophil-Driven Inflammatory Damage. Cell *177*, 541-555.e17.

35. Otten, M.A., Bakema, J.E., Tuk, C.W., Glennie, M.J., Tutt, A.L., Beelen, R.H.J., van de Winkel, J.G.J., and van Egmond, M. (2012). Enhanced FcαRI-mediated neutrophil migration towards tumour colonies in the presence of endothelial cells. Eur. J. Immunol. *42*, 1815–1821.

36. Poplimont, H., Georgantzoglou, A., Boulch, M., Walker, H.A., Coombs, C., Papaleonidopoulou, F., and Sarris, M. (2020). Neutrophil swarming in damaged tissue is orchestrated by connexins and cooperative calcium alarm signals. Curr. Biol. *30*, 2761-2776.e7.

37. Scarpa, E., Szabó, A., Bibonne, A., Theveneau, E., Parsons, M., and Mayor, R. (2015). Cadherin Switch during EMT in Neural Crest Cells Leads to Contact Inhibition of

Locomotion via Repolarization of Forces. Dev. Cell *34*, 421–434.

38. Binnewies, M., Roberts, E.W., Kersten, K., Chan, V., Fearon, D.F., Merad, M., Coussens, L.M., Gabrilovich, D.I., Ostrand-Rosenberg, S., Hedrick, C.C., *et al.* (2018). Understanding the tumor immune microenvironment (TIME) for effective therapy. Nat. Med. *24*, 541–550.

39. Song, E., Mao, T., Dong, H., Boisserand, L.S.B., Antila, S., Bosenberg, M., Alitalo, K., Thomas, J.-L., and Iwasaki, A. (2020). VEGF-C-driven lymphatic drainage enables immunosurveillance of brain tumours. Nature *577*, 689–694.

40. Beatty, G.L., Winograd, R., Evans, R.A., Long, K.B., Luque, S.L., Lee, J.W., Clendenin, C., Gladney, W.L., Knoblock, D.M., Guirnalda, P.D., *et al.* (2015). Exclusion of T cells from pancreatic carcinomas in mice is regulated by ly6c(low) F4/80(+) extratumoral macrophages. Gastroenterology *149*, 201–210.

41. Xu, N., Palmer, D.C., Robeson, A.C., Shou, P., Bommiasamy, H., Laurie, S.J., Willis, C., Dotti, G., Vincent, B.G., Restifo, N.P., *et al.* (2021). STING agonist promotes CAR T cell trafficking and persistence in breast cancer. J. Exp. Med. *218*.

42. Schumacher, D., Strilic, B., Sivaraj, K.K., Wettschureck, N., and Offermanns, S. (2013). Platelet-derived nucleotides promote tumor-cell transendothelial migration and metastasis via P2Y2 receptor. Cancer Cell *24*, 130–137.

43. Strilic, B., and Offermanns, S. (2017). Intravascular survival and extravasation of tumor cells. Cancer Cell *32*, 282–293.

44. Leong, H.S., Robertson, A.E., Stoletov, K., Leith, S.J., Chin, C.A., Chien, A.E., Hague, M.N., Ablack, A., Carmine-Simmen, K., McPherson, V.A., *et al.* (2014). Invadopodia are required for cancer cell extravasation and are a therapeutic target for metastasis. Cell Rep. *8*, 1558–1570.

45. Tichet, M., Prod'Homme, V., Fenouille, N., Ambrosetti, D., Mallavialle, A., Cerezo, M., Ohanna, M., Audebert, S., Rocchi, S., Giacchero, D., *et al.* (2015). Tumour-derived SPARC drives vascular permeability and extravasation through endothelial VCAM1 signalling to promote metastasis. Nat. Commun. *6*, 6993.

46. Strilic, B., Yang, L., Albarrán-Juárez, J., Wachsmuth, L., Han, K., Müller, U.C., Pasparakis, M., and Offermanns, S. (2016). Tumour-cell-induced endothelial cell necroptosis via death receptor 6 promotes metastasis. Nature *536*, 215–218.

47. Labelle, M., Begum, S., and Hynes, R.O. (2011). Direct signaling between platelets and cancer cells induces an epithelial-mesenchymal-like transition and promotes metastasis. Cancer Cell *20*, 576–590.

48. Labelle, M., Begum, S., and Hynes, R.O. (2014). Platelets guide the formation of early metastatic niches. Proc Natl Acad Sci USA *111*, E3053-61.

49. Zeng, Q., Michael, I.P., Zhang, P., Saghafinia, S., Knott, G., Jiao, W., McCabe, B.D., Galván, J.A., Robinson, H.P.C., Zlobec, I., *et al.* (2019). Synaptic proximity enables NMDAR signalling to promote brain metastasis. Nature *573*, 526–531.

50. Chen, Q., Boire, A., Jin, X., Valiente, M., Er, E.E., Lopez-Soto, A., Jacob, L., Patwa, R., Shah, H., Xu, K., *et al.* (2016). Carcinoma-astrocyte gap junctions promote brain metastasis by cGAMP transfer. Nature *533*, 493–498.

51. Stoletov, K., Strnadel, J., Zardouzian, E., Momiyama, M., Park, F.D., Kelber, J.A., Pizzo, D.P., Hoffman, R., VandenBerg, S.R., and Klemke, R.L. (2013). Role of connexins in metastatic breast cancer and melanoma brain colonization. J. Cell Sci. *126*, 904–913.

52. Oliveira, R., Christov, C., Guillamo, J.S., de Boüard, S., Palfi, S., Venance, L., Tardy, M., and Peschanski, M. (2005). Contribution of gap junctional communication between tumor cells and astroglia to the invasion of the brain parenchyma by human glioblastomas. BMC Cell Biol. *6*, 7.

53. Sin, W.C., Aftab, Q., Bechberger, J.F., Leung, J.H., Chen, H., and Naus, C.C. (2016). Astrocytes promote glioma invasion via the gap junction protein connexin43. Oncogene *35*, 1504–1516.

54. Civita, P., M Leite, D., and Pilkington, G.J. (2019). Pre-Clinical Drug Testing in 2D and 3D Human In Vitro Models of Glioblastoma Incorporating Non-Neoplastic Astrocytes: Tunneling Nano Tubules and Mitochondrial Transfer Modulates Cell Behavior and Therapeutic Respons. Int. J. Mol. Sci. *20*.

55. Leite, D.M., Zvar Baskovic, B., Civita, P., Neto, C., Gumbleton, M., and Pilkington, G.J. (2020). A human co-culture cell model incorporating microglia supports glioblastoma growth and migration, and confers resistance to cytotoxics. FASEB J. *34*, 1710–1727.

56. Burgoyne, A.M., Palomo, J.M., Phillips-Mason, P.J., Burden-Gulley, S.M., Major, D.L., Zaremba, A., Robinson, S., Sloan, A.E., Vogelbaum, M.A., Miller, R.H., *et al.* (2009). PTPmu suppresses glioma cell migration and dispersal. Neuro Oncol. *11*, 767–778.

57. Appolloni, I., Barilari, M., Caviglia, S., Gambini, E., Reisoli, E., and Malatesta, P. (2015). A cadherin switch underlies malignancy in high-grade gliomas. Oncogene *34*, 1991–2002.

58. Walck-Shannon, E., and Hardin, J. (2014). Cell intercalation from top to bottom. Nat. Rev. Mol. Cell Biol. *15*, 34–48.

59. Stubbs, J.L., Davidson, L., Keller, R., and Kintner, C. (2006). Radial intercalation of ciliated cells during Xenopus skin development. Development *133*, 2507–2515.

60. Kim, K., Lake, B.B., Haremaki, T., Weinstein, D.C., and Sokol, S.Y. (2012). Rab11 regulates planar polarity and migratory behavior of multiciliated cells in Xenopus embryonic epidermis. Dev. Dyn. *241*, 1385–1395.

61. Werner, M.E., Mitchell, J.W., Putzbach, W., Bacon, E., Kim, S.K., and Mitchell, B.J. (2014). Radial intercalation is regulated by the Par complex and the microtubule-stabilizing protein CLAMP/Spef1. J. Cell Biol. *206*, 367–376.

62. Sirour, C., Hidalgo, M., Bello, V., Buisson, N., Darribère, T., and Moreau, N. (2011). Dystroglycan is involved in skin morphogenesis downstream of the Notch signaling pathway. Mol. Biol. Cell *22*, 2957–2969.

63. Sedzinski, J., Hannezo, E., Tu, F., Biro, M., and Wallingford, J.B. (2016). Emergence of an apical epithelial cell surface in vivo. Dev. Cell *36*, 24–35.

64. Sedzinski, J., Hannezo, E., Tu, F., Biro, M., and Wallingford, J.B. (2017). RhoA regulates actin network dynamics during apical surface emergence in multiciliated epithelial cells. J. Cell Sci. *130*, 420–428.

65. Bharathan, N.K., and Dickinson, A.J.G. (2019). Desmoplakin is required for epidermal integrity and morphogenesis in the Xenopus laevis embryo. Dev. Biol. *450*, 115–131.

66. Ewald, A.J., Brenot, A., Duong, M., Chan, B.S., and Werb, Z. (2008). Collective epithelial migration and cell rearrangements drive mammary branching morphogenesis. Dev. Cell *14*, 570–581.

67. Neumann, N.M., Perrone, M.C., Veldhuis, J.H., Huebner, R.J., Zhan, H., Devreotes, P.N., Brodland, G.W., and Ewald, A.J. (2018). Coordination of receptor tyrosine kinase signaling and interfacial tension dynamics drives radial intercalation and tube elongation. Dev. Cell *45*, 67-82.e6.

68. Cutz, E., Pan, J., Yeger, H., Domnik, N.J., and Fisher, J.T. (2013). Recent advances and contraversies on the role of pulmonary neuroepithelial bodies as airway sensors. Semin. Cell Dev. Biol. *24*, 40–50.

69. Guha, A., Vasconcelos, M., Cai, Y., Yoneda, M., Hinds, A., Qian, J., Li, G., Dickel, L., Johnson, J.E., Kimura, S., *et al.* (2012). Neuroepithelial body microenvironment is a niche for a distinct subset of Clara-like precursors in the developing airways. Proc Natl Acad Sci USA *109*, 12592–12597.

70. Kuo, C.S., and Krasnow, M.A. (2015). Formation of a neurosensory organ by epithelial cell slithering. Cell *163*, 394–405.

71. Barton, L.J., LeBlanc, M.G., and Lehmann, R. (2016). Finding their way: themes in germ cell migration. Curr. Opin. Cell Biol. *42*, 128–137.

72. DeGennaro, M., Hurd, T.R., Siekhaus, D.E., Biteau, B., Jasper, H., and Lehmann, R.

(2011). Peroxiredoxin stabilization of DE-cadherin promotes primordial germ cell adhesion. Dev. Cell *20*, 233–243.

73. Seifert, J.R.K., and Lehmann, R. (2012). Drosophila primordial germ cell migration requires epithelial remodeling of the endoderm. Development *139*, 2101–2106.

74. Renault, A.D., Sigal, Y.J., Morris, A.J., and Lehmann, R. (2004). Soma-germ line competition for lipid phosphate uptake regulates germ cell migration and survival. Science *305*, 1963–1966.

75. Ricardo, S., and Lehmann, R. (2009). An ABC transporter controls export of a Drosophila germ cell attractant. Science *323*, 943–946.

76. Kardash, E., Reichman-Fried, M., Maître, J.-L., Boldajipour, B., Papusheva, E., Messerschmidt, E.-M., Heisenberg, C.-P., and Raz, E. (2010). A role for Rho GTPases and cell-cell adhesion in single-cell motility in vivo. Nat. Cell Biol. *12*, 47–53; sup pp 1.

77. Grimaldi, C., Schumacher, I., Boquet-Pujadas, A., Tarbashevich, K., Vos, B.E., Bandemer, J., Schick, J., Aalto, A., Olivo-Marin, J.-C., Betz, T., *et al.* (2020). E-cadherin focuses protrusion formation at the front of migrating cells by impeding actin flow. Nat. Commun. *11*, 5397.

78. Gross-Thebing, S., Truszkowski, L., Tenbrinck, D., Sánchez-Iranzo, H., Camelo, C., Westerich, K.J., Singh, A., Maier, P., Prengel, J., Lange, P., *et al.* (2020). Using migrating cells as probes to illuminate features in live embryonic tissues. Sci. Adv. *6*.

79. Paksa, A., Bandemer, J., Hoeckendorf, B., Razin, N., Tarbashevich, K., Minina, S., Meyen, D., Biundo, A., Leidel, S.A., Peyrieras, N., *et al.* (2016). Repulsive cues combined with physical barriers and cell-cell adhesion determine progenitor cell positioning during organogenesis. Nat. Commun. *7*, 11288.

80. Montell, D.J., Yoon, W.H., and Starz-Gaiano, M. (2012). Group choreography: mechanisms orchestrating the collective movement of border cells. Nat. Rev. Mol. Cell Biol. *13*, 631–645.

81. Unable to find information for 319237.

82. Mishra, A.K., Mondo, J.A., Campanale, J.P., and Montell, D.J. (2019). Coordination of protrusion dynamics within and between collectively migrating border cells by myosin II. Mol. Biol. Cell *30*, 2490–2502.

83. Miao, G., Godt, D., and Montell, D.J. (2020). Integration of Migratory Cells into a New Site In Vivo Requires Channel-Independent Functions of Innexins on Microtubules. Dev. Cell *54*, 501-515.e9.

84. Cai, D., and Montell, D.J. (2014). Diverse and dynamic sources and sinks in gradient formation and directed migration. Curr. Opin. Cell Biol. *30*, 91–98.

85. Artemenko, Y., Lampert, T.J., and Devreotes, P.N. (2014). Moving towards a paradigm: common mechanisms of chemotactic signaling in Dictyostelium and mammalian leukocytes. Cell. Mol. Life Sci. *71*, 3711–3747.

86. Swaney, K.F., Huang, C.-H., and Devreotes, P.N. (2010). Eukaryotic chemotaxis: a network of signaling pathways controls motility, directional sensing, and polarity. Annu. Rev. Biophys. *39*, 265–289.

87. Unable to find information for 1172894.

88. Duchek, P., and Rørth, P. (2001). Guidance of cell migration by EGF receptor signaling during Drosophila oogenesis. Science *291*, 131–133.

89. Duchek, P., Somogyi, K., Jékely, G., Beccari, S., and Rørth, P. (2001). Guidance of cell migration by the Drosophila PDGF/VEGF receptor. Cell *107*, 17–26.

90. McDonald, J.A., Pinheiro, E.M., and Montell, D.J. (2003). PVF1, a PDGF/VEGF homolog, is sufficient to guide border cells and interacts genetically with Taiman. Development *130*, 3469–3478.

91. McDonald, J.A., Pinheiro, E.M., Kadlec, L., Schupbach, T., and Montell, D.J. (2006). Multiple EGFR ligands participate in guiding migrating border cells. Dev. Biol. *296*, 94–103.

92. Bussmann, J., and Raz, E. (2015). Chemokine-guided cell migration and motility in zebrafish development. EMBO J. *34*, 1309–1318.

93. Mayor, R., and Theveneau, E. (2013). The neural crest. Development *140*, 2247–2251.

94. Ng, M.R., Besser, A., Danuser, G., and Brugge, J.S. (2012). Substrate stiffness regulates cadherin-dependent collective migration through myosin-II contractility. J. Cell Biol. *199*, 545–563.

95. Aranjuez, G., Burtscher, A., Sawant, K., Majumder, P., and McDonald, J.A. (2016). Dynamic myosin activation promotes collective morphology and migration by locally balancing oppositional forces from surrounding tissue. Mol. Biol. Cell *27*, 1898–1910.

96. Cai, D., Chen, S.-C., Prasad, M., He, L., Wang, X., Choesmel-Cadamuro, V., Sawyer, J.K., Danuser, G., and Montell, D.J. (2014). Mechanical feedback through E-cadherin promotes direction sensing during collective cell migration. Cell *157*, 1146–1159.

97. Alsous, J.I., Villoutreix, P., Stoop, N., Shvartsman, S.Y., and Dunkel, J. (2018). Entropic effects in cell lineage tree packings. Nat. Phys. *14*, 1016–1021.

98. Zanotelli, M.R., Rahman-Zaman, A., VanderBurgh, J.A., Taufalele, P.V., Jain, A., Erickson, D., Bordeleau, F., and Reinhart-King, C.A. (2019). Energetic costs regulated by cell mechanics and confinement are predictive of migration path during decision-making. Nat. Commun. *10*, 4185.

99. Renkawitz, J., Kopf, A., Stopp, J., de Vries, I., Driscoll, M.K., Merrin, J., Hauschild, R., Welf, E.S., Danuser, G., Fiolka, R., *et al.* (2019). Nuclear positioning facilitates amoeboid migration along the path of least resistance. Nature *568*, 546–550.

100. Matias, N.R., Mathieu, J., and Huynh, J.-R. (2015). Abscission is regulated by the ESCRT-III protein shrub in Drosophila germline stem cells. PLoS Genet. *11*, e1004653.

101. Lilly, M.A., and Spradling, A.C. (1996). The Drosophila endocycle is controlled by Cyclin E and lacks a checkpoint ensuring S-phase completion. Genes Dev. *10*, 2514–2526.

102. Wang, X., He, L., Wu, Y.I., Hahn, K.M., and Montell, D.J. (2010). Light-mediated activation reveals a key role for Rac in collective guidance of cell movement in vivo. Nat. Cell Biol. *12*, 591–597.

103. Murphy, A.M., and Montell, D.J. (1996). Cell type-specific roles for Cdc42, Rac, and RhoL in Drosophila oogenesis. J. Cell Biol. *133*, 617–630.

104. Friedl, P., and Mayor, R. (2017). Tuning Collective Cell Migration by Cell-Cell Junction Regulation. Cold Spring Harb. Perspect. Biol. *9*.

105. Friedl, P., Locker, J., Sahai, E., and Segall, J.E. (2012). Classifying collective cancer cell invasion. Nat. Cell Biol. *14*, 777–783.

106. Silver, D.L., and Montell, D.J. (2001). Paracrine signaling through the JAK/STAT pathway activates invasive behavior of ovarian epithelial cells in Drosophila. Cell *107*, 831–841.

107. Bai, J., and Montell, D. (2002). Eyes absent, a key repressor of polar cell fate during Drosophila oogenesis. Development *129*, 5377–5388.

108. Jang, A.C.-C., Chang, Y.-C., Bai, J., and Montell, D. (2009). Border-cell migration requires integration of spatial and temporal signals by the BTB protein Abrupt. Nat. Cell Biol. *11*, 569–579.

109. Bai, J., Uehara, Y., and Montell, D.J. (2000). Regulation of invasive cell behavior by taiman, a Drosophila protein related to AIB1, a steroid receptor coactivator amplified in breast cancer. Cell *103*, 1047–1058.

110. Dai, W., Guo, X., Cao, Y.S., Mondo, J.A., Campanale, J.P., Montell, B.J., Burrous, H., Streichan, S., Gov, N., Rappel, W.-J., *et al.* (2020). Tissue topography steers migrating Drosophila border cells. BioRxiv.

111. Kim, J.H., Cho, A., Yin, H., Schafer, D.A., Mouneimne, G., Simpson, K.J., Nguyen, K.-V., Brugge, J.S., and Montell, D.J. (2011). Psidin, a conserved protein that regulates protrusion dynamics and cell migration. Genes Dev. *25*, 730–741.

112. Lee, T., Feig, L., and Montell, D.J. (1996). Two distinct roles for Ras in a

developmentally regulated cell migration. Development *122*, 409–418.

113. McDonald, J.A., Khodyakova, A., Aranjuez, G., Dudley, C., and Montell, D.J. (2008). PAR-1 kinase regulates epithelial detachment and directional protrusion of migrating border cells. Curr. Biol. *18*, 1659–1667.

114. Fulga, T.A., and Rørth, P. (2002). Invasive cell migration is initiated by guided growth of long cellular extensions. Nat. Cell Biol. *4*, 715–719.

115. Ramel, D., Wang, X., Laflamme, C., Montell, D.J., and Emery, G. (2013). Rab11 regulates cell-cell communication during collective cell movements. Nat. Cell Biol. *15*, 317–324.

116. Assaker, G., Ramel, D., Wculek, S.K., González-Gaitán, M., and Emery, G. (2010). Spatial restriction of receptor tyrosine kinase activity through a polarized endocytic cycle controls border cell migration. Proc Natl Acad Sci USA *107*, 22558–22563.

117. Colombié, N., Choesmel-Cadamuro, V., Series, J., Emery, G., Wang, X., and Ramel, D. (2017). Non-autonomous role of Cdc42 in cell-cell communication during collective migration. Dev. Biol. *423*, 12–18.

118. Chen, Y., Kotian, N., Aranjuez, G., Chen, L., Messer, C.L., Burtscher, A., Sawant, K., Ramel, D., Wang, X., and McDonald, J.A. (2020). Protein phosphatase 1 activity controls a balance between collective and single cell modes of migration. eLife *9*.

119. Laflamme, C., Assaker, G., Ramel, D., Dorn, J.F., She, D., Maddox, P.S., and Emery, G. (2012). Evi5 promotes collective cell migration through its Rab-GAP activity. J. Cell Biol. *198*, 57–67.

120. Ogienko, A.A., Yarinich, L.A., Fedorova, E.V., Dorogova, N.V., Bayborodin, S.I., Baricheva, E.M., and Pindyurin, A.V. (2020). GAGA regulates border cell migration in drosophila. Int. J. Mol. Sci. *21*.

121. Berez, A., Peercy, B.E., and Starz-Gaiano, M. (2020). Development and analysis of a quantitative mathematical model of bistability in the cross repression system between APT and SLBO within the JAK/STAT signaling pathway. Front. Physiol. *11*, 803.

122. Wang, X., Wang, H., Liu, L., Li, S., Emery, G., and Chen, J. (2020). Temporal Coordination of Collective Migration and Lumen Formation by Antagonism between Two Nuclear Receptors. iScience *23*, 101335.

123. Wang, H., Guo, X., Wang, X., Wang, X., and Chen, J. (2020). Supracellular Actomyosin Mediates Cell-Cell Communication and Shapes Collective Migratory Morphology. iScience *23*, 101204.

124. Fox, E.F., Lamb, M.C., Mellentine, S.Q., and Tootle, T.L. (2020). Prostaglandins regulate invasive, collective border cell migration. Mol. Biol. Cell *31*, 1584–1594.

125. Plutoni, C., Keil, S., Zeledon, C., Delsin, L.E.A., Decelle, B., Roux, P.P., Carréno, S.,

and Emery, G. (2019). Misshapen coordinates protrusion restriction and actomyosin contractility during collective cell migration. Nat. Commun. *10*, 3940.

126. Zeledon, C., Sun, X., Plutoni, C., and Emery, G. (2019). The ArfGAP Drongo Promotes Actomyosin Contractility during Collective Cell Migration by Releasing Myosin Phosphatase from the Trailing Edge. Cell Rep. *28*, 3238-3248.e3.

127. Lamb, M.C., Anliker, K.K., and Tootle, T.L. (2020). Fascin regulates protrusions and delamination to mediate invasive, collective cell migration in vivo. Dev. Dyn. *249*, 961–982.

128. Ghiglione, C., Jouandin, P., Cérézo, D., and Noselli, S. (2018). The Drosophila insulin pathway controls Profilin expression and dynamic actin-rich protrusions during collective cell migration. Development *145*.

129. Sharma, A., Halder, S., Felix, M., Nisaa, K., Deshpande, G., and Prasad, M. (2018). Insulin signaling modulates border cell movement in Drosophila oogenesis. Development *145*.

130. Liu, Y., and Montell, D.J. (1999). Identification of mutations that cause cell migration defects in mosaic clones. Development *126*, 1869–1878.

131. Wang, X., Bo, J., Bridges, T., Dugan, K.D., Pan, T., Chodosh, L.A., and Montell, D.J. (2006). Analysis of cell migration using whole-genome expression profiling of migratory cells in the Drosophila ovary. Dev. Cell *10*, 483–495.

132. Stathakis, D.G., Burton, D.Y., McIvor, W.E., Krishnakumar, S., Wright, T.R., and O'Donnell, J.M. (1999). The catecholamines up (Catsup) protein of Drosophila melanogaster functions as a negative regulator of tyrosine hydroxylase activity. Genetics *153*, 361–382.

133. Hsouna, A., Lawal, H.O., Izevbaye, I., Hsu, T., and O'Donnell, J.M. (2007). Drosophila dopamine synthesis pathway genes regulate tracheal morphogenesis. Dev. Biol. *308*, 30–43.

134. Groth, C., Sasamura, T., Khanna, M.R., Whitley, M., and Fortini, M.E. (2013). Protein trafficking abnormalities in Drosophila tissues with impaired activity of the ZIP7 zinc transporter Catsup. Development *140*, 3018–3027.

135. Kambe, T. (2011). Zinc Transport: Regulation. In Encyclopedia of inorganic and bioinorganic chemistry, R. A. Scott, ed. (Chichester, UK: John Wiley & Sons, Ltd), pp. 1–9.

136. Taylor, K.M., Morgan, H.E., Johnson, A., and Nicholson, R.I. (2004). Structure-function analysis of HKE4, a member of the new LIV-1 subfamily of zinc transporters. Biochem. J. *377*, 131–139.

137. Kambe, T., Tsuji, T., Hashimoto, A., and Itsumura, N. (2015). The physiological,

biochemical, and molecular roles of zinc transporters in zinc homeostasis and metabolism. Physiol. Rev. *95*, 749–784.

138. Nguyen, T.S.L., Kohno, K., and Kimata, Y. (2013). Zinc depletion activates the endoplasmic reticulum-stress sensor Ire1 via pleiotropic mechanisms. Biosci. Biotechnol. Biochem. *77*, 1337–1339.

139. Tan, S., Han, R., Li, P., Yang, G., Li, S., Zhang, P., Wang, W.-B., Zhao, W.-Z., and Yin, L.-P. (2015). Over-expression of the MxIRT1 gene increases iron and zinc content in rice seeds. Transgenic Res. *24*, 109–122.

140. Zhang, P., Tan, S., Berry, J.O., Li, P., Ren, N., Li, S., Yang, G., Wang, W.-B., Qi, X.-T., and Yin, L.-P. (2014). An uncleaved signal peptide directs the Malus xiaojinensis iron transporter protein Mx IRT1 into the ER for the PM secretory pathway. Int. J. Mol. Sci. *15*, 20413–20433.

141. Adulcikas, J., Norouzi, S., Bretag, L., Sohal, S.S., and Myers, S. (2018). The zinc transporter SLC39A7 (ZIP7) harbours a highly-conserved histidine-rich N-terminal region that potentially contributes to zinc homeostasis in the endoplasmic reticulum. Comput. Biol. Med. *100*, 196–202.

142. Tuncay, E., Bitirim, V.C., Durak, A., Carrat, G.R.J., Taylor, K.M., Rutter, G.A., and Turan, B. (2017). Hyperglycemia-Induced Changes in ZIP7 and ZnT7 Expression Cause Zn2+ Release From the Sarco(endo)plasmic Reticulum and Mediate ER Stress in the Heart. Diabetes *66*, 1346–1358.

143. Fauster, A., Rebsamen, M., Willmann, K.L., César-Razquin, A., Girardi, E., Bigenzahn, J.W., Schischlik, F., Scorzoni, S., Bruckner, M., Konecka, J., *et al.* (2019). Systematic genetic mapping of necroptosis identifies SLC39A7 as modulator of death receptor trafficking. Cell Death Differ. *26*, 1138–1155.

144. Sarov, M., Barz, C., Jambor, H., Hein, M.Y., Schmied, C., Suchold, D., Stender, B., Janosch, S., K J, V.V., Krishnan, R.T., *et al.* (2016). A genome-wide resource for the analysis of protein localisation in Drosophila. eLife *5*, e12068.

145. Borensztejn, A., Boissoneau, E., Fernandez, G., Agnès, F., and Pret, A.-M. (2013). JAK/STAT autocontrol of ligand-producing cell number through apoptosis. Development *140*, 195–204.

146. Haas, P., and Gilmour, D. (2006). Chemokine signaling mediates self-organizing tissue migration in the zebrafish lateral line. Dev. Cell *10*, 673–680.

147. Geisbrecht, E.R., and Montell, D.J. (2004). A role for Drosophila IAP1-mediated caspase inhibition in Rac-dependent cell migration. Cell *118*, 111–125.

148. Wang, Z., Ferdousy, F., Lawal, H., Huang, Z., Daigle, J.G., Izevbaye, I., Doherty, O., Thomas, J., Stathakis, D.G., and O'Donnell, J.M. (2011). Catecholamines up

integrates dopamine synthesis and synaptic trafficking. J. Neurochem. *119*, 1294–1305.

149. Navarro, J.A., Heßner, S., Yenisetti, S.C., Bayersdorfer, F., Zhang, L., Voigt, A., Schneuwly, S., and Botella, J.A. (2014). Analysis of dopaminergic neuronal dysfunction in genetic and toxin-induced models of Parkinson's disease in Drosophila. J. Neurochem. *131*, 369–382.

150. Terriente-Felix, A., Li, J., Collins, S., Mulligan, A., Reekie, I., Bernard, F., Krejci, A., and Bray, S. (2013). Notch cooperates with Lozenge/Runx to lock haemocytes into a differentiation programme. Development *140*, 926–937.

151. Wang, X., Adam, J.C., and Montell, D. (2007). Spatially localized Kuzbanian required for specific activation of Notch during border cell migration. Dev. Biol. *301*, 532–540.

152. Okajima, T., Xu, A., Lei, L., and Irvine, K.D. (2005). Chaperone activity of protein O-fucosyltransferase 1 promotes notch receptor folding. Science *307*, 1599–1603.

153. Sone, M., Zeng, X., Larese, J., and Ryoo, H.D. (2013). A modified UPR stress sensing system reveals a novel tissue distribution of IRE1/XBP1 activity during normal Drosophila development. Cell Stress Chaperones *18*, 307–319.

154. Karagöz, G.E., Aragón, T., and Acosta-Alvear, D. (2019). Recent advances in signal integration mechanisms in the unfolded protein response. [version 1; peer review: 2 approved]. F1000Res. *8*.

155. Chow, C.Y., Avila, F.W., Clark, A.G., and Wolfner, M.F. (2015). Induction of excessive endoplasmic reticulum stress in the Drosophila male accessory gland results in infertility. PLoS ONE *10*, e0119386.

156. Karagöz, G.E., Acosta-Alvear, D., and Walter, P. (2019). The Unfolded Protein Response: Detecting and Responding to Fluctuations in the Protein-Folding Capacity of the Endoplasmic Reticulum. Cold Spring Harb. Perspect. Biol. *11*.

157. Nolin, E., Gans, S., Llamas, L., Bandyopadhyay, S., Brittain, S.M., Bernasconi-Elias, P., Carter, K.P., Loureiro, J.J., Thomas, J.R., Schirle, M., *et al.* (2019). Discovery of a ZIP7 inhibitor from a Notch pathway screen. Nat. Chem. Biol. *15*, 179–188.

158. Taylor, K.M., Hiscox, S., Nicholson, R.I., Hogstrand, C., and Kille, P. (2012). Protein kinase CK2 triggers cytosolic zinc signaling pathways by phosphorylation of zinc channel ZIP7. Sci. Signal. *5*, ra11.

159. Rogers, E.E., Eide, D.J., and Guerinot, M.L. (2000). Altered selectivity in an Arabidopsis metal transporter. Proc Natl Acad Sci USA *97*, 12356–12360.

160. Christianson, J.C., Olzmann, J.A., Shaler, T.A., Sowa, M.E., Bennett, E.J., Richter, C.M., Tyler, R.E., Greenblatt, E.J., Harper, J.W., and Kopito, R.R. (2011). Defining human ERAD networks through an integrative mapping strategy. Nat. Cell Biol. *14*,

93–105.

161. Ohashi, W., Kimura, S., Iwanaga, T., Furusawa, Y., Irié, T., Izumi, H., Watanabe, T., Hijikata, A., Hara, T., Ohara, O., *et al.* (2016). Zinc Transporter SLC39A7/ZIP7 Promotes Intestinal Epithelial Self-Renewal by Resolving ER Stress. PLoS Genet. *12*, e1006349.

162. Xu, J., Zhao, H., and Wang, T. (2020). Suppression of retinal degeneration by two novel ERAD ubiquitin E3 ligases SORDD1/2 in Drosophila. PLoS Genet. *16*, e1009172.

163. Ferguson, K.M. (2008). Structure-based view of epidermal growth factor receptor regulation. Annu. Rev. Biophys. *37*, 353–373.

164. Unable to find information for 11289069.

165. Unable to find information for 5712751.

166. Shacham, T., Sharma, N., and Lederkremer, G.Z. (2019). Protein misfolding and ER stress in huntington's disease. Front. Mol. Biosci. *6*, 20.

167. Go, M.J., Eastman, D.S., and Artavanis-Tsakonas, S. (1998). Cell proliferation control by Notch signaling in Drosophila development. Development *125*, 2031–2040.

168. Dai, W., and Montell, D.J. (2016). Live imaging of border cell migration in drosophila. Methods Mol. Biol. *1407*, 153–168.

169. Okajima, T., Xu, A., and Irvine, K.D. (2003). Modulation of notch-ligand binding by protein O-fucosyltransferase 1 and fringe. J. Biol. Chem. *278*, 42340–42345.

170. Schaks, M., Giannone, G., and Rottner, K. (2019). Actin dynamics in cell migration. Essays Biochem. *63*, 483–495.

171. Garcin, C., and Straube, A. (2019). Microtubules in cell migration. Essays Biochem. *63*, 509–520.

172. Leduc, C., and Etienne-Manneville, S. (2015). Intermediate filaments in cell migration and invasion: the unusual suspects. Curr. Opin. Cell Biol. *32*, 102–112.

173. Short, B. (2014). Septins provide a link to epithelial migration. J. Cell Biol. *207*, 162.2-162.

174. Cho, A., Kato, M., Whitwam, T., Kim, J.H., and Montell, D.J. (2016). An Atypical Tropomyosin in Drosophila with Intermediate Filament-like Properties. Cell Rep. *16*, 928–938.

175. Gaspar, I., Sysoev, V., Komissarov, A., and Ephrussi, A. (2016). An RNA-binding tropomyosin recruits kinesin-1 dynamically to*oskar* mRNPs. BioRxiv.

176. Veeranan-Karmegam, R., Boggupalli, D.P., Liu, G., and Gonsalvez, G.B. (2016). A

new isoform of Drosophila non-muscle Tropomyosin 1 interacts with Kinesin-1 and functions in oskar mRNA localization. J. Cell Sci. *129*, 4252–4264.

177. Gáspár, I., Sysoev, V., Komissarov, A., and Ephrussi, A. (2017). An RNA-binding atypical tropomyosin recruits kinesin-1 dynamically to oskar mRNPs. EMBO J. *36*, 319–333.